THE UNIVERSITY OF QUEENSLAND

AUSTRALIA

Enabling Multi-Photon Experiments with Solid-State Emitters: A Farewell to Downconversion

Juan C. Loredo

M.Phys.

Abstract

Advances in photonics will lead to breakthroughs in technology with a similar impact to that resulted from the development of electronics. At the quantum level, photons exhibit some unique features, such as non-classical correlations and bosonic bunching. The manipulation of these quanta of light foresee the construction of quantum devices capable of outperforming their classical counterparts in the purposes for which they are built. Despite a significant progress in developing quantum technologies, several unsolved issues certainly remain: Efficient quantification of quantum correlations in a system, and manipulation of multiple photons at once, are two of such hurdles to be overcome. In this thesis, we tackle these two issues and present experimental progress towards their solution. We first explore quantum entanglement between two single-photons and its effect on phases appearing on the system's wavefunction. The observed phases revealed an intimate connection between entanglement—a purely quantum phenomena—and geometric and topological structures of abstract manifolds: A special case of geometric phases was found to increase monotonically with the amount of entanglement in the system, thus serving as an alternative measure of quantum correlations. We then employed a system of three single-photons, and two concatenated entangling gates, as the basis of a quantum simulation protocol: A three-particle quantum simulator, mimicking the entangling evolution of two particles, is used to experimentally demonstrate that the overhead in measuring concurrence—a measure of two-particle entanglement—can be significantly reduced down to measuring only two observables. At this point, increasing the number of photons being handled proved extremely difficult; the low efficiency of photon sources based on parametric downconversion—the gold-standard and only source at-the-time used for multi-photon experiments—imposed a hard limit on countrates and hence the number of photons to be manipulated. We thus then focused on overcoming this obstacle: We studied a solid-state emitter and its performance as a multi-photon source. We employed a quantum dot-cavity system to show that streams of tens of indistinguishable single-photons are produced, whose temporal-to-spatial demultiplexing serves as a novel kind of multi-photon source. A three-photon source was then built and employed in the first demonstration of multi-photon interference from a solid-state source: We implemented a BosonSampling device with a source that is between one and two orders-of-magnitude more efficient than its downconversion counterpart. The main limiting factors for scaling to higher photon numbers were identified to be not intrinsic to the solid-state emitter, but determined by low detector efficiencies and the probabilistic nature of the demultiplexing scheme. Future improvements on these limitations are expected to allow the generation of sources with a higher number of single-photons, a task that has to date remained otherwise impossible.

Declaration by author

This thesis is composed of my original work, and contains no material previously published or written by another person except where due reference has been made in the text. I have clearly stated the contribution by others to jointly-authored works that I have included in my thesis.

I have clearly stated the contribution of others to my thesis as a whole, including statistical assistance, survey design, data analysis, significant technical procedures, professional editorial advice, and any other original research work used or reported in my thesis. The content of my thesis is the result of work I have carried out since the commencement of my research higher degree candidature and does not include a substantial part of work that has been submitted to qualify for the award of any other degree or diploma in any university or other tertiary institution. I have clearly stated which parts of my thesis, if any, have been submitted to qualify for another award.

I acknowledge that an electronic copy of my thesis must be lodged with the University Library and, subject to the policy and procedures of The University of Queensland, the thesis be made available for research and study in accordance with the Copyright Act 1968 unless a period of embargo has been approved by the Dean of the Graduate School.

I acknowledge that copyright of all material contained in my thesis resides with the copyright holder(s) of that material. Where appropriate I have obtained copyright permission from the copyright holder to reproduce material in this thesis.

Publications during candidature

Peer-reviewed publications

1. *Observation of entanglement-dependent two-particle holonomic phase,*
   J. C. Loredo, M. A. Broome, D. H. Smith, A. G. White
   Physical Review Letters **112**, 143603 (2014). (e-print: *arXiv:1306.3370*)

2. *Polarimetric measurements of single-photon geometric phases,*
   O. Ortíz, Y. Yugra, A. Rosario, J. C. Sihuincha, J. C. Loredo, M. V. Andrés, F. De Zela
   Physical Review A **89**, 012124 (2014). (e-print: *arXiv:1510.03802*)

3. *Measuring entanglement in a photonic embedding quantum simulator,*
   J. C. Loredo, M. P. Almeida, R. Di Candia, J. S. Pedernales, J. Casanova, E. Solano, A. G. White
   Physical Review Letters **116**, 070503 (2016). (e-print: *arXiv:1506.05108*)

4. *Near-optimal single-photon sources in the solid state,*
   N. Somaschi, V. Giesz, L. De Santis, J. C. Loredo, M. P. Almeida, G. Hornecker, S. L. Portalupi,
   T. Grange, C. Anton, J. Demory, C. Gomez, I. Sagnes, N. D. Lanzillotti-Kimura, A. Lemaitre,
   A. Auffeves, A. G. White, L. Lanco, P. Senellart
   Nature Photonics **Advance Online Publication** (2016). (e-print: *arXiv:1510.06499*)

5. *Scalable performance in solid-state single-photon sources,*
   J. C. Loredo, N. A. Zakaria, N. Somaschi, N., C. Anton, L. De Santis, V. Giesz, T. Grange,
   M. A. Broome, O. Gazzano, G. Coppola, I. Sagnes, A. Lemaitre, A. Auffeves, P. Senellart,
   M. P. Almeida, A. G. White
   Optica **3**, 433-440 (2016). (e-print: *arXiv:1601.00654*)

Publications included in this thesis

Observation of entanglement-dependent two-particle holonomic phase,

J. C. Loredo, M. A. Broome, D. H. Smith, A. G. White

Physical Review Letters **112**, 143603 (2014).

Incorporated as Chapter 2.

Contributor	Statement of contribution	% Contribution
J. C. Loredo (Candidate)	Initial development of concept	100%
	Design and construction of experiment	80%
	Preliminary and final data acquisition	100%
	Data analysis and interpretation	70%
	Theoretical results	100%
	Complete first draft of manuscript	80%
	Final draft of manuscript	80%
	Referee replies and final manuscript revision	70%
M. A. Broome	Design and construction of experiment	10%
	Data analysis and interpretation	20%
	Complete first draft of manuscript	10%
	Final draft of manuscript	10%
	Referee replies and final manuscript revision	20%
D. H. Smith	Design and construction of experiment	10%
A. G. White	Data analysis and interpretation	10%
	Complete first draft of manuscript	10%
	Final draft of manuscript	10%
	Referee replies and final manuscript revision	10%

Measuring entanglement in a photonic embedding quantum simulator,

J. C. Loredo, M. P. Almeida, R. Di Candia, J. S. Pedernales, J. Casanova, E. Solano, A. G. White

Physical Review Letters **116**, 070503 (2016).

Incorporated as Chapter 3.

Contributor	Statement of contribution	% Contribution
J. C. Loredo (Candidate)	Initial development of concept	30%
	Design and construction of experiment	80%
	Preliminary and final data acquisition	100%
	Data analysis and interpretation	70%
	Complete first draft of manuscript	60%
	Final draft of manuscript	60%
	Referee replies and final manuscript revision	40%
M. P. Almeida	Design and construction of experiment	20%
	Data analysis and interpretation	10%
	Referee replies and final manuscript revision	10%
R. Di Candia	Theoretical model	25%
	Referee replies and final manuscript revision	10%
J. S. Pedernales	Theoretical model	25%
	Complete first draft of manuscript	10%
	Final draft of manuscript	10%
	Referee replies and final manuscript revision	10%
J. Casanova	Initial development of concept	30%
	Theoretical model	25%
	Complete first draft of manuscript	10%
	Final draft of manuscript	10%
	Referee replies and final manuscript revision	10%
E. Solano	Initial development of concept	40%
	Data analysis and interpretation	10%
	Theoretical model	25%
	Complete first draft of manuscript	10%
	Final draft of manuscript	10%
	Referee replies and final manuscript revision	10%
A. G. White	Data analysis and interpretation	10%
	Complete first draft of manuscript	10%
	Final draft of manuscript	10%
	Referee replies and final manuscript revision	10%

Contributor	Statement of contribution	% Contribution
J. C. Loredo (Candidate)	Initial development of concept	20%
	Design and construction of experiment	40%
	Preliminary and final data acquisition	50%
	Data analysis and interpretation	70%
	Complete first draft of manuscript	70%
	Final draft of manuscript	70%
	Referee replies and final manuscript revision	50%
N. A. Zakaria	Design and construction of experiment	15%
	Preliminary and final data acquisition	15%
N. Somaschi	Design and construction of experiment	5%
	Preliminary and final data acquisition	5%
C. Anton	Design and construction of experiment	5%
	Preliminary and final data acquisition	5%
L. De Santis	Design and construction of experiment	5%
	Preliminary and final data acquisition	5%
V. Giesz	Design and construction of experiment	5%
	Preliminary and final data acquisition	5%
T. Grange	Theoretical model	70%
M. A. Broome	Design and construction of experiment	5%
	Preliminary and final data acquisition	5%
O. Gazzano	Design and construction of experiment	5%
	Preliminary and final data acquisition	5%
G. Coppola	Design and construction of experiment	5%
	Preliminary and final data acquisition	5%
I. Sagnes	Etching of micropillar cavities	100%
A. Lemaitre	Growth of quantum dots	100%
A. Auffeves	Theoretical model	30%
P. Senellart	Initial development of concept	25%
	Data analysis and interpretation	10%
	Complete first draft of manuscript	15%
	Final draft of manuscript	15%
	Referee replies and final manuscript revision	30%

Contributor	Statement of contribution	% Contribution
M. P. Almeida	Initial development of concept	25%
	Design and construction of experiment	10%
	Data analysis and interpretation	10%
	Referee replies and final manuscript revision	10%
A. G. White	Initial development of concept	30%
	Data analysis and interpretation	10%
	Complete first draft of manuscript	15%
	Final draft of manuscript	15%
	Referee replies and final manuscript revision	10%

Contributions by others to the thesis

No contributions by others except as co-authors as outlined in the "Publications included in this thesis" section.

Statement of parts of the thesis submitted to qualify for the award of another degree

None.

Acknowledgements

I will miss thanking many individuals in this one page, certainly. Even a few pages do not seem enough to extensively and individually express my gratitude to all those who were part of this four-year journey. I shall however mention only a few that cross my mind at this very moment.

Unquestionably, my gratitude goes first to my parents: Your diligent, selfless, and tireless work made my days simple and easy, so I could dedicate my time to enjoy the things that I enjoy, eventually leading to this minute so I could thank you for it all.

I want to thank my advisor, Andrew White, an inspiring person of unending laughter: Thank you for having me, for your ethical teachings, for correcting my endless typos in English, and for supporting me during these four years of exciting research days. We shall keep in touch!

To Margot Chavez: As hard as I try I can not thank you enough for your patience, company, and caring since long before any of this started. Thank you Gota! I am back now and we shall enjoy the beach, especially when it rains.

Many other names deserve—without a doubt—individual mentioning and thanking. But did I mention one more I would risk to miss many instead. You all know who you are, and you would believe me when I say that I am deeply thankful for meeting you and sharing those moments that led to this point. To you all: Thank you!

Keywords

Australian and New Zealand Standard Research Classifications (ANZSRC)

ANZSRC code: 020604 Quantum Optics, 40%

ANZSRC code: 020603 Quantum Information, Computation and Communication 40%

ANZSRC code: 020503 Nonlinear Optics and Spectroscopy, 20%

Fields of Research (FoR) Classification

FoR code: 0206 Quantum Physics, 80%
FoR code: 0205 Optical Physics, 20%

Contents

List of Figures

For my parents.

Overview

Photon sources based on spontaneous parametric downconversion have been to date the workhorse for most optical quantum information processing protocols [1]. These sources proved being very useful in proof-of-principle experiments, serving in the demonstration of several seminal works—such as quantum teleportation [2], entangling quantum logic gates [3], bipartite- [4] and multi-partite entanglement [5, 6], and loophole-free Bell tests [7, 8], to name only a few. However, it is well recognised that the two-decades old technology presents serious difficulties regarding scalability: Experiments so far consisted mostly of two-photon protocols, and only one eight-photon realisation has been reported [6]. The inherent low efficiency of the downconversion process makes it extremely difficult to experimentally study quantum phenomena with higher numbers of single-photons.

The content of this thesis represents my efforts—in collaboration with my co-authors—on developing new approaches for reducing two current limitations in quantum information and quantum photonics. Two main results can then be outlined from this work: The first result is with regards to reducing the difficulty in quantifying entanglement in quantum systems; and the second result deals with the implementation of a new kind of multi-photon source based on a semiconductor quantum dot embedded in a micropillar cavity, where the issue of scalability has been addressed and a source with promising scalable potential was obtained.

Parts of this thesis

This work is primarily a thesis by publication. Three chapters (Chapters 2, 3, and 4) are published peer reviewed papers, and one chapter (Chapter 5) is a manuscript submitted and currently under review. All of which I am the lead author, having dealt with a substantial load in each project. The thesis is made of two parts, Parts I and II, whose content is organised as follows.

Part I: Photons: A Reduced Measurement Overhead for Entanglement

Chapter 1 presents the concept of a source of single-photons. I discuss the theoretical concept of an ideal single-photon source, and what experimentalists refer to as one. We provide a general overview of the current state-of-the-art of photon sources, considering the advantages and disadvantages that different systems have to offer. The chapter ends with a brief description of the experimental properties of two kinds of sources used in this thesis, one is based on

parametric downconversion, and the other one employs a sample with semiconductor quantum dots developed by our collaborators in the group of Prof. Pascale Senellart in Paris.

In Chapter 2 we study phases appearing in the evolving state of two single-photons entangled in their polarisation. These phases appear as a shift in the interferometric modulation of a two-photon coincidence measurement; as such they differ to previously studied one-particle phases and belong a 6-dimensional parameter space describing the joint-state of two-photons. Specific bi-local evolutions are chosen to enforce that the dynamical component of the gained phase vanishes and only its geometrical (or topological) nature is observed. Theoretically, we found that one special kind of geometric phases vanishes for all separable—unentangled—states and monotonically increases with the amount of entanglement—quantified, e.g., by the tangle (concurrence squared)—between the particles. In this sense, it serves as an alternative method to quantify entanglement in a system of two particles without the necessity of full tomographic reconstruction techniques [9].

Chapter 3 describes the experimental demonstration of a quantum simulation protocol [10] introduced by our collaborators in the group of Prof. Enrique Solano in Bilbao. In this *Embedding Quantum Simulator*, the addition of one ancillary qubit allows for the efficient measurement of entanglement monotones: Measuring only either two or six observables—depending on the dimension of the system's Hilbert space—is sufficient to extract the "strength" of multipartite quantum correlations. We built a three-qubit quantum simulator that mimics the evolution of two qubits undergoing an entangling dynamics, for which we used a source of three photons (plus a fourth trigger photon) and two control-sign gates implemented with linear-optics. The simulated concurrence of the evolving system was obtained by measuring only two observables, instead of the fifteen that full state tomography requires.

Part II: Multi-Photon Experiments with Solid-State Emitters

Given the difficulty in continuing increasing the number of single-photons being manipulated from a downconversion source, we turned our efforts into exploring a novel technology that presented great potential as a single-photon source. This is based on solid-state emitters—quantum dots coupled to micropillar cavity structures—with much higher efficiency than downconversion processes, thus with potential to overcome previous limitations and ultimately replacing the older technology.

In Chapter 4, we first focused on implementing an efficient setup for collecting the emitted light from the quantum dot-micropillar system. As a result, a source brightness at the output of a single-mode fibre of 14% was obtained: About one in seven laser pulses results in a high-quality single-photon that can be directly used. We then showed that this source emits streams of tens of single-photons that remain highly indistinguishable. Each of these consecutive photons are produced by independent laser pulses, which contrasts favourably to downconversion sources, where photons generated from independent pump-events exhibit a strongly decreased indistinguishability.

Chapter 5 presents the concluding experiment of this thesis. The source developed in Chap-

ter 4 is temporal-to-spatial demultiplexed into a source that can be run as multiple partially-indistinguishable single-photons. Operated as a 3-photon source, it is used in a BosonSampling protocol, where the developed source is between one and two orders-of-magnitude more efficient than previous equivalent downconversion sources.

References

[1] Pan, J.-W. *et al.* Multiphoton entanglement and interferometry. *Rev. Mod. Phys.* **84**, 777–838 (2012).

[2] Bouwmeester, D. *et al.* Experimental quantum teleportation. *Nature* **390**, 575–579 (1997).

[3] O'Brien, J. L., Pryde, G. J., White, A. G., Ralph, T. C. & Branning, D. Demonstration of an all-optical quantum controlled-not gate. *Nature* **426**, 264–267 (2003).

[4] Kwiat, P. G. *et al.* New high-intensity source of polarization-entangled photon pairs. *Phys. Rev. Lett.* **75**, 4337–4341 (1995).

[5] Bouwmeester, D., Pan, J.-W., Daniell, M., Weinfurter, H. & Zeilinger, A. Observation of three-photon greenberger-horne-zeilinger entanglement. *Phys. Rev. Lett.* **82**, 1345–1349 (1999).

[6] Yao, X.-C. *et al.* Observation of eight-photon entanglement. *Nat Photon* **6**, 225–228 (2012).

[7] Giustina, M. *et al.* Significant-loophole-free test of bell's theorem with entangled photons. *Phys. Rev. Lett.* **115**, 250401 (2015).

[8] Shalm, L. K. *et al.* Strong loophole-free test of local realism*. *Phys. Rev. Lett.* **115**, 250402 (2015).

[9] James, D. F. V., Kwiat, P. G., Munro, W. J. & White, A. G. Measurement of qubits. *Phys. Rev. A* **64**, 052312 (2001).

[10] Di Candia, R. *et al.* Embedding quantum simulators for quantum computation of entanglement. *Phys. Rev. Lett.* **111**, 240502 (2013).

Part I

Photons: A Reduced Measurement Overhead for Entanglement

CHAPTER 1

Sources of single-photons

I NTERACTION with light is amongst the earliest ways by which we begin learning what is around us. Before we even realise what light is, its importance became clear as it represents a window through which we explore our world. But what is light? From "rays from fire" according to the Greeks twenty-five centuries ago, through wave and corpuscular theories put forward by Hook and Newton, light is to date understood as radiation of the electromagnetic field. Its quanta is the *photon*: An elementary "indivisible" particle (not made of other sub-particles), carrier of the electromagnetic force.

Several processes are known by which photons are produced: Charges subject to acceleration lose energy by radiating a continuous photon flux; the annihilation of an electron and its antiparticle the positron results in the creation of two photons; and the decay of an atomic excited state produces a single photon with a well defined energy. Thermal radiation—due to thermal motion of charges—is an example of the former case, and can be explained in terms of classical physics. The latter two cases, on the other hand, are examples of quantum phenomena at high and low energies, respectively. In this work we focus on sources that emit—in principle— only one photon at the time: A single-photon source.

1.1 The wish-list

An *ideal* single-photon source satisfies the following wish-list [1]:

1. The source is deterministic, or "on-demand": Photon emission can occur at any time, as defined by a user.

2. 100% source efficiency: Every attempt does result in the emission of a photon.

3. 0% multiple-photon emission: Only a single-photon Fock state is emitted.

4. 100% photon indistinguishability: All emitted photons are indistinguishable from one another.

Also, arguably with less immediate importance than the other characteristics, another desirable feature of an ideal single-photon source is that it can be operated at an arbitrarily fast repetition rate, limited only by photon lifetimes.

The above mentioned idealised characteristics are, obviously, only possible in a theoretical concept. In practice, the literature considers a device as a single-photon source to that satisfying (at least partially) characteristic (3) of the wish-list. Experimental implementations to date have met, to some extent, one or more of such features simultaneously, being different physical systems better suited than others at different characteristics. Therefore, depending on the particular application the experimenter has in mind, an "approximate" single-photon source from one or another system can suffice.

Below we briefly describe the different kinds of single-photon sources with respect to the mentioned wish-list. For characteristics (3) and (4), we provide experimental results obtained during this PhD candidature with two kinds of sources, with bulk non-linear crystals and with solid-state emitters, located at UQ's Quantum Technology Laboratory (QTLab).

1.1.1 On-demand single-photon sources

For on-demand photon generation, some physical systems naturally[1] lead to the emission of a single photon with an inherently high probability: Atomic and atom-like systems in which the relaxation of an excited state of a single electron in the emitter results in the creation of one[2] photon. Examples of sources of the former kind are atoms with two-level [2] and multi-level energy structures [3, 4, 5], and trapped ions [6, 7, 8]; while atomic-like systems include single-molecules [9, 10, 11, 12], and solid-state emitters such as color centers in diamonds [13, 14, 15] and quantum dots (QDs) [16, 17, 18, 19].

On the other hand, non-linear crystals—media where the dielectric polarisation is non-linearly modulated by electric fields—can also produce pairs of photons by parametric fluorescence. This process, called Spontaneous Parametric Downconversion (SPDC), generates photon pairs in two modes[3] [20, 21], where the detection of a downconverted photon in one mode *heralds* [22] the presence of a single-photon[4] in the other mode. Although this generates a heralded single-photon source, the downconversion process is probabilistic and inefficient, producing single photons at random instances. Therefore SPDC does not constitute an on-demand source and is inherently non-deterministic. There are however ongoing efforts to overcome this inherently low-efficiency by using active spatial- and temporal-multiplexing methods [23, 24, 25].

The "on-demand", or "deterministic", term in these sources refers to an intrinsic high efficiency (virtually up to a unity probability) of photon emission into a free (arbitrary) propagation mode, without considering, e.g., whether such mode has a high or low degree of directionality

---

[1]In this context "naturally" means without explicit implementation of demultiplexing schemes. Thus it refers to processes with intrinsic high efficiency.

[2]Subject to experimental conditions that lead to measuring non-perfect single-photon statistics. For example, pump pulses with a temporal duration of similar scale than relaxation times leading to emission of more than one photon per excitation cycle, recapture processes due to non-resonant excitation schemes, or slow detectors not able to resolve time-bins with vanishing photon statistics.

[3]The output of downconversion is an infinite weighted sum of two-mode n-Fock states: A two-mode squeezed vacuum state.

[4]A heralded SPDC source can produce single-photon statistics if operated at low pump powers. However, at higher powers contribution from higher-order photon Fock states become appreciable and introduce noise to the obtained statistics.

or if its transversal mode is suitable for efficient collection and interconnect with further optical circuits. An on-demand source can thus exhibit poor collection efficiency and still remain as an inefficient way of producing single photons for practical purposes.

1.1.2 Efficient and bright sources

Efficiency

For a source to be efficient one typically requires that the emitted photon also exhibits a well-defined spatial mode with a high degree of directionality, and preferably with a transverse mode as close as possible to the TEM_{00} single-mode. This can be done by coupling the emitter to a photonic structure [26] that imprints its mode onto the emitted light. Achieving this is technologically more challenging for atomic sources than for single-molecule and solid-state emitters.

Single-molecules can be located within an "optical antenna" that alters its molecular dipole, efficiently converting the 4π solid-angle emission into a well defined mode with a high degree of directionality [27, 28, 29, 30]. However, they present a complex transverse mode that is not straightforwardly convertible into a more versatile mode, such as that of a single-mode fibre. Solid-state quantum dots, on the other hand, can be coupled to cavity structures enhancing the emission into a (cavity) mode that resembles a better approximation to a TEM_{00} mode and thus can be efficiently collected by a single-mode fibre for further use [31, 32, 33, 34, 35, 36, 37]; or enhancing emission into modes within an integrated circuit where the exterior coupling can be circumvented by performing state preparation, processing, and detection within the same integrated chip [38, 39, 40]. Emitter-cavity mode coupling has to date been realised via either a probabilistic or a deterministic approach: The first consists of fabricating a large number of devices and eventually finding some that exhibit the desired coupling [31, 32]; whereas the latter method[5] consists on the deterministic fabrication of a structure around the emitter, where coupling is achieved in every—thus the term deterministic—device fabricated [33, 34, 35, 36, 37].

Brightness

A successful emitter-structure coupling results in large probabilities of collecting the emitted light. This leads to the definition of *source brightness*: The probability per laser pump pulse[6] of collecting[7] a single-photon at the first lens of the experimental setup. The experimenter extracts this measure by carefully determining the optical loses from the first lens all the way down to the efficiency of the employed detectors, and then correcting the detected count-rates to find the photon rates before the first lens. Under this definition, large brightnesses have been demonstrated, in some cases reaching near unity values.

---

[5]This deterministic fabrication method was first introduced in the literature by our collaborators in Paris, who provide the quantum dot samples we used in the experiments of the second part of this thesis.

[6]A source brightness can also be considered for CW pumped sources. However, the quantum dot based experiments performed in this thesis employed a pulsed scheme, thus we refer here only to this case.

[7]This refers to those photons that are captured and refracted within the numeric aperture of the collecting lens.

The definition of brightness at the first lens has been useful to characterise and compare various sources from the same or different systems, irrespective of the setup efficiency. However, one criticism is that it lacks of practical meaning. Every experiment—before the realisation of this thesis—would report systematically incredibly large brightness however accompanied with low detected rates, resulting in a gap of several orders-of-magnitude between the reported brightness and actual detected rates. This lead to the necessity of obtaining large photon fluxes at a point in an experimental setup that can be easily interconnected with further experiments, such as at the output of a single-mode fibre. One can then define an *absolute brightness*[8] as the probability per laser pump pulse of generating a high-purity, spectrally isolated, single-photon at the output of a single-mode fibre[9]. As part of the results obtained in this thesis, the first high absolute brightness demonstrated in any physical system was obtained, reaching a record value of 14%, as explained in detail in Chapter 4.

1.1.3 Single-photon purity

Photon sources can produce a variety of states: A light-bulb is a source of thermal light[10]; the output of a laser is in good approximation a coherent state; and an excited state of an electron in an atom decays producing one photon. A relevant quantity in the characterisation of these different kinds of sources is the second-order autocorrelation function $g^{(2)}(\tau)$ [41]:

$$g^{(2)}(\tau) = \frac{\langle \hat{a}^{\dagger}(t)\hat{a}^{\dagger}(t+\tau)\hat{a}(t+\tau)\hat{a}(t) \rangle}{\langle \hat{a}^{\dagger}(t)\hat{a}(t) \rangle^2}, \tag{1.1}$$

where $\hat{a}$ and $\hat{a}^{\dagger}$ are respectively the annihilation and creation operator. Equation (1.1), when evaluated at zero delay $\tau=0$, can be written as:

$$g^{(2)}(0) = 1 + \frac{(\Delta n)^2 - \overline{n}}{\overline{n}^2}, \tag{1.2}$$

with $(\Delta n)^2 = \langle \hat{n}^2 \rangle - \langle \hat{n} \rangle^2$ the field variance, $\hat{n} = \hat{a}^{\dagger}\hat{a}$ the number operator, and $\overline{n} = \langle \hat{n} \rangle$ the average photon number. The explicit form in Eq. (1.2) is particularly useful, as it is simply given in terms of the mean photon number and variance, quantities characterising the field. The thermal, coherent, and Fock states are exemplified below.

Thermal state

A thermal state can be written as:

$$\hat{\rho}^{\text{th}} = \sum_{m=0}^{\infty} \frac{\overline{n}^m}{(\overline{n}+1)^{m+1}} |m\rangle\langle m|, \tag{1.3}$$

---

[8]This term has been suggested and introduced to the literature (other groups already started using it) as a result of the work done in this PhD candidature.

[9]The inclusion of "high-purity", and "spectrally isolated" features are here used to maintain consistency with the definition considered in Chapter 4.

[10]Any object produces thermal light as a result of the thermal motion of charges within the object.

where $|m\rangle$ is m-th excited Fock state. The variance of this state is:

$$(\Delta n)^2 = \overline{n}\,(\overline{n}+1)\,, \tag{1.4}$$

thus, in virtue of Eq. (1.2), it follows:

$$g^{(2)}_{\text{thermal}}(0) = 2. \tag{1.5}$$

Coherent state

The coherent state takes the form:

$$|\alpha\rangle = e^{-\frac{|\alpha|^2}{2}} \sum_{n=0}^{\infty} \frac{\alpha^n}{\sqrt{n!}}|n\rangle, \tag{1.6}$$

with $\alpha \in \mathbb{C}$ an amplitude parameter such that $\overline{n}=|\alpha|^2$. The variance of this state is smaller than for the thermal state, and equals the mean photon number:

$$(\Delta n)^2 = \overline{n}. \tag{1.7}$$

This results in:

$$g^{(2)}_{\text{coherent}}(0) = 1. \tag{1.8}$$

Fock state

A Fock state $|n\rangle$, $n \in \mathbb{N}$, has an exact photon occupation number—consequently an undefined phase—resulting in a vanishing variance for any $|n\rangle$:

$$(\Delta n)^2 = 0, \ \forall n. \tag{1.9}$$

Therefore one obtains the second-order autocorrelation function at zero delay:

$$g^{(2)}_{\text{Fock}}(0) = 1 - \frac{1}{n}. \tag{1.10}$$

Note that two regimes are identified based on the autocorrelation function: A classical regime, with $g^{(2)}(0)>1$, where light is said to be "bunched" (photons tend to form groups distributed in time); and the non-classical regime with "antibunched" photons (photons are more evenly separated in time), with $0 \leq g^{(2)}(0)<1$, and where the maximally antibunched state of light is the single-photon Fock state $|n\rangle=|1\rangle$, in which case the the autocorrelation function takes its minimum value $g^{(2)}(0)=0$. The coherent state, with $g^{(2)}(0)=1$, represents a boundary between the two scenarios.

A comparison between these distributions at the single-photon level occurs for small $\overline{n}$. Figure 1.1 shows the cases discussed above for $\overline{n}=5$, $\overline{n}=2$, and $\overline{n}=1$. Note that the characteristic (3) of the wish-list—that is, 0% multiple-photon terms—is only satisfied for the single-photon
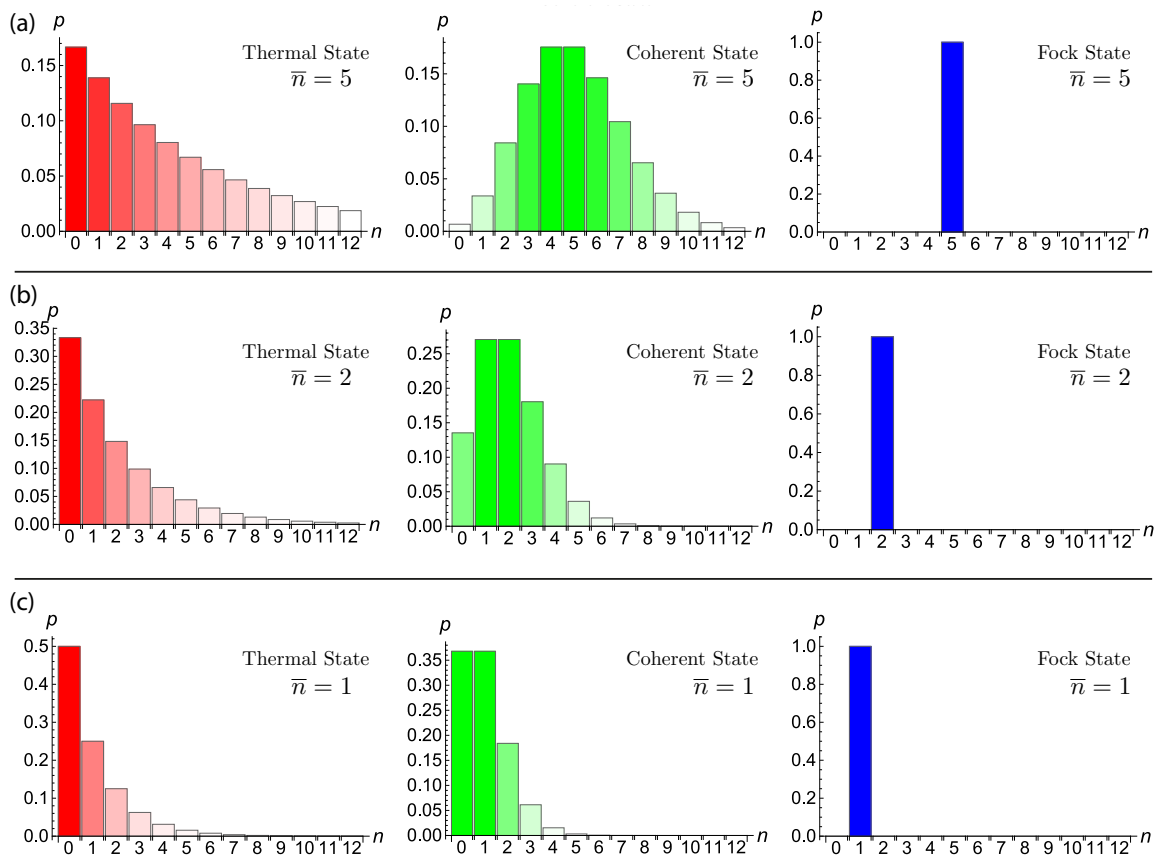
Figure 1.1: Photon number probability distribution. Thermal, coherent, and Fock states for (a) $\overline{n}$=5, (b) $\overline{n}$=2, and (c) $\overline{n}$=1.

Fock state. Nonetheless, the literature is quite forgiving on what it considers as a single-photon source: A non-classical source of light whose photon number statistics exhibits more antibunching than the two-photon Fock state $|n\rangle=|2\rangle$—that is, a source with $g^{(2)}(0)<0.5$. Note that purity here then refers to what extent the output of the photon source approximates to a single-photon Fock state, thus the ideal pure single-photon source holds for $g^{(2)}(0)=0$, or alternatively a single-photon purity[11] of $1-g^{(2)}(0)=1$.

1.1.4 Photon indistinguishability

The indistinguishability of bosonic particles, such as the photon, leads to unique quantum phenomena without classical akin. It has enabled a broad range of applications, from quantum teleportation [42, 43], to linear-optics quantum computing [44, 45]. First observed by Hong, Ou, and Mandel [46]—thereby called the Hong-Ou-Mandel (HOM) effect—in the bunching[12] of two photons at the output of a balanced 2×2 beamsplitter when both photons are indistinguish-

---

[11]It is convenient to refer to $1-g^{(2)}(0)$ as the single-photon purity because its value is 0% at the classical boundary, and 100% for the ideal case.

[12]Photons leave always at the same output of the beamsplitter. The cases where photons leave in different outputs are suppressed due to two-photon quantum interference (HOM effect).

able[13]. Phenomenom observed to date in a variety of physical systems, including atoms [47], ions [48], color centers [49], single molecules [50], superconducting circuits [51], parametric downconversion [46, 52], and quantum dots [53].

This effect is a consequence of the symmetric bosonic nature[14]. If the state describing all degrees of freedom of two photons is symmetric before the beamsplitter, then after the path degree-of-freedom introduced by the beamsplitter the output state contains only bunched events as to remain symmetric. Conversely, if the state before the beamsplitter is antisymmetric[15] in one degree-of-freedom, e.g., with an odd-mode Hermite-Gaussian transverse profile, or an entangled state in the antisymmetric Bell state $|\Psi^-\rangle$, then the spatial degree-of-freedom at the output is antibunched [54]—that is, in the antisymmetric spatial-mode configuration—as to enforce an overall output symmetric state for the bosonic particles.

In idealised conditions, this effect is seen as the complete suppression of coincidence counts at the output of a balanced beamsplitter. However, in a more general case, when a linear-device characterised by the transfer matrix $\mathcal{L}$ is used, photons with a degree of indistinguishability quantified by $\mathcal{I}$ are detected at its output with a coincidence probability [55]:

$$c = \frac{(1+\mathcal{I})}{2} \left|\mathrm{per}(\mathcal{L})\right|^2 + \frac{(1-\mathcal{I})}{2} \left|\det(\mathcal{L})\right|^2 , \tag{1.11}$$

with $\mathrm{per}(\mathcal{L})$ the permanent of $\mathcal{L}$, and $\det(\mathcal{L})$ the determinant.

Below we present two kinds of photon sources located at the QTLAB, one based on quantum dots, and the other based on spontaneous parametric downconversion, and present measurements of their single-photon purities and photon indistinguishability.

1.2 Quantum dot based photon source

A quantum dot is a semiconductor nanocrystal of a given band gap surrounded by another host semiconductor of a larger band gap. The host semiconductor provides a potential barrier such that electrons and holes[16] within the inner semiconductor are confined to nanometer-size scales[17] in all three spatial dimensions, resulting in the quantisation of electronic levels and thus the possibility of emitting discrete quanta of light. See Refs. [26, 56] for detailed discussions of the use of quantum dots as single-photon sources.

By either optically or electrically pumping this solid-state emitter, excitons (bound states of an electron and a hole) are created in the quantum dot, whose relaxation results in the creation of a photon. Other states, such as biexcitons (bound states between two excitons) and trions

---

[13]The photons need to be indistinguishable in every degree-of-freedom, including spectra, polarisation, and time of arrival at the interface of the beamsplitter.

[14]The state describing a bosonic system remains unchanged after any pair-wise exchange of bosons.

[15]An antisymmetric state picks up a π phase factor upon exchange of bosons.

[16]A hole is the absence of an electron. It is considered as if it was a (positively charged) quasi-particle that interacts with the electrons within the quantum dot as to simplify mathematical calculations of the motion of electrons in the material.

[17]The size of a quantum dot determines the energy of the emitted photons. The larger the quantum dot is, the lower the energy of its emitted light.

(composed of two electrons and one hole, or two holes and one electron) are also very appealing for the emission of entangled photons [57, 58, 59] or preparing spin qubits [60, 61, 62, 63], respectively.

The radiative decay of one exciton should lead to the emission of only one photon with the same properties every time (indistinguishable). However, experimental pumping conditions are essential in the resulting statistics of the emitted light. Three regimes based on the energy of the pump are identified:

1. *Above-band excitation.* The quantum dot is excited above the band gap of the host semi-conductor. Some of the excitons created on the host material are captured by the wetting layer—the first layer made of the inner semiconductor where the quantum dots are formed—to then decay non-radiatively[18] via a phonon assisted process into the inner energy levels of the quantum dot. At this stage a final radiative decay results in the emission of a photon. This pumping scheme is experimentally attractive because the large energy difference between that of the quantum dot and the pump allows to straightforwardly isolate emission modes from laser light, e.g., by using a dichroic filter or a monochromator. However, recombination of electron-hole pairs in the semiconductor occurs at timescales not much shorter than the radiative recombination of the quantum dot, then more than one photon per excitation pulse can be generated due to recombination of carriers within the same relaxation process. Only moderate single-photon purities are thus obtained in this excitation regime, with typical $g^{(2)}(0)$ values in the $0.10-0.50$ range. Two photon interference visibilities, accounting for both non-ideal purity and decreased indistinguishability, are rather low with this scheme, often also in the $10-50\%$ range.

2. *Quasi-resonant excitation.* The energy of the pump corresponds to one of the higher excited states of the quantum dot, e.g., in its p-shell. The state rapidly decays into the first excited state of the quantum dot where radiative recombination leads to the emission of a photon. In this scheme, interaction occurs directly between the pump light and the quantum dot, and more pump power is needed due to the small cross section of the emitter. An improved single-photon purity is observed, with $g^{(2)}(0)$ often under 0.05, and in some conditions reaching values below 0.01. A time jitter remains in the preparation of the exciton, as it results from a decay of higher excited states, which in combination with pure dephasing—caused by random charges near the quantum dot that randomly shift the transition energy of the quantum dot—result in non-ideal indistinguishabilities, with typical values reaching the 70% mark.

3. *Resonant excitation.* The laser pump energy is matched to the quantum dot first excited state. This represents the optimal regime to operate the source at: A coherently controlled quantum dot, as evidenced by the observation of Rabi oscillations, is deterministically prepared in the exciton state at a π-pulse preparation[19]. Both single-photon purities and

---

[18]A non-radiative process is that where the decay in energy level does not involve light emission. Conversely, a radiative decay leads to the emission of a photon.

[19]First maximum of the Rabi oscillation.

indistinguishability can reach near-optimal values under this excitation scheme. However, this regime is experimentally more challenging because the straightforward colour-filtering is no longer possible, and other techniques—e.g., orthogonal polarisation of excitation and collection modes—must be used to suppress the pump laser light.
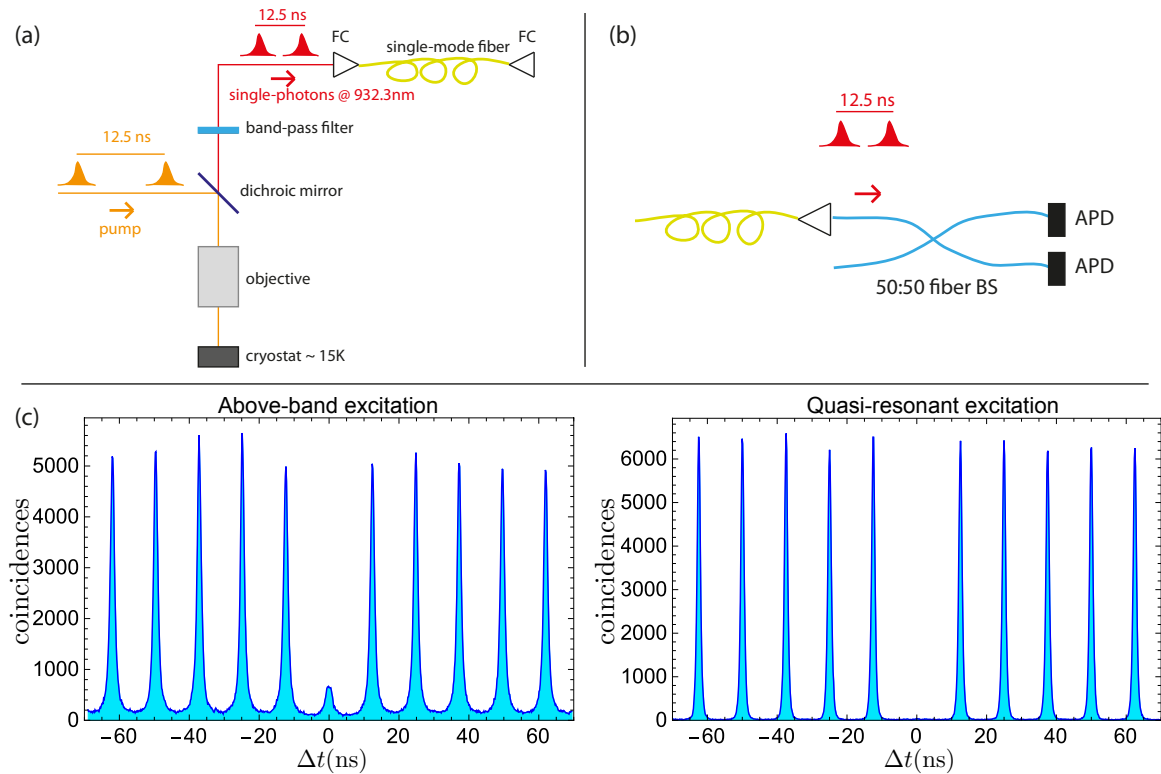
Figure 1.2: Purity of a single-photon from a quantum dot. (a) Depiction of the quantum dot based single-photon source. (b) Coincidence detection at the output of a HBT setup measures the second-order autocorrelation function. (c) Single-photon purities of the same quantum dot with excitation occurring above band (left), resulting in $g^{(2)}(0)=0.165\pm0.001$, or on the p-shell (right), exhibiting a near-ideal purity with $g^{(2)}(0)=0.006 \pm 0.001$. These values are obtained by integrating the detected counts, without any background correction, within a 2 ns window around zero delay divided by the average of the 10 adjacent peaks.

Our experimental apparatus at the QTLAB, to date, allows us to excite the quantum dot in the former two regimes. Figure 1.2(a) shows the schematics of the setup. A sample—fabricated by our collaborators in the group of Prof. Pascale Senellart in Paris, first studied in Ref. [33]—consisting of quantum dots deterministically coupled to micropillar cavities is located inside a closed-cycle cryostat at a temperature of T=15 K, corresponding to the emitter-cavity resonance[20]. Laser pulses at 80 MHz repetition rate, wavelength λ_{pump} below 922 nm[21], excite the quantum dot either on its p-shell[22] (λ_{pump}=909.3 nm), or above-band (λ_{pump}=820.0 nm).

---

[20]The sample contains multiple devices, each of them will have a different resonance temperature, mostly within the $10-20$ K range.

[21]This is the cut-off wavelength of the dichroic filter.

[22]This is one of multiple wavelengths with which the quantum dot can get excited. The measurements in Chapters 4, and 5 used a different p-shell state at λ=905.3 nm.

A microscope objective with N.A.=0.3 is used in confocal configuration to focus the pump light to a diameter size of $\sim 3\ \mu m$, close to the diameter of the micropillar cavity, and simultaneously collects the emitted photons. A dichroic mirror separates the emission mode from the pump, and a band-pass filter with a FWHM=0.85 nm is used to further suppress any scattered laser light. The emitted single-photons, with λ=932.3 nm, are then collected in a single-mode fibre. In Figure 1.2(b), a standard Hanbury-Brown and Twiss setup measures the second-order autocorrelation function of the emitted fluorescence. Experimental results of a $g^{(2)}(\Delta t)$ measurement are shown in Fig. 1.2(c) at low pump powers under above-band (left), and quasi-resonant (right) excitation.
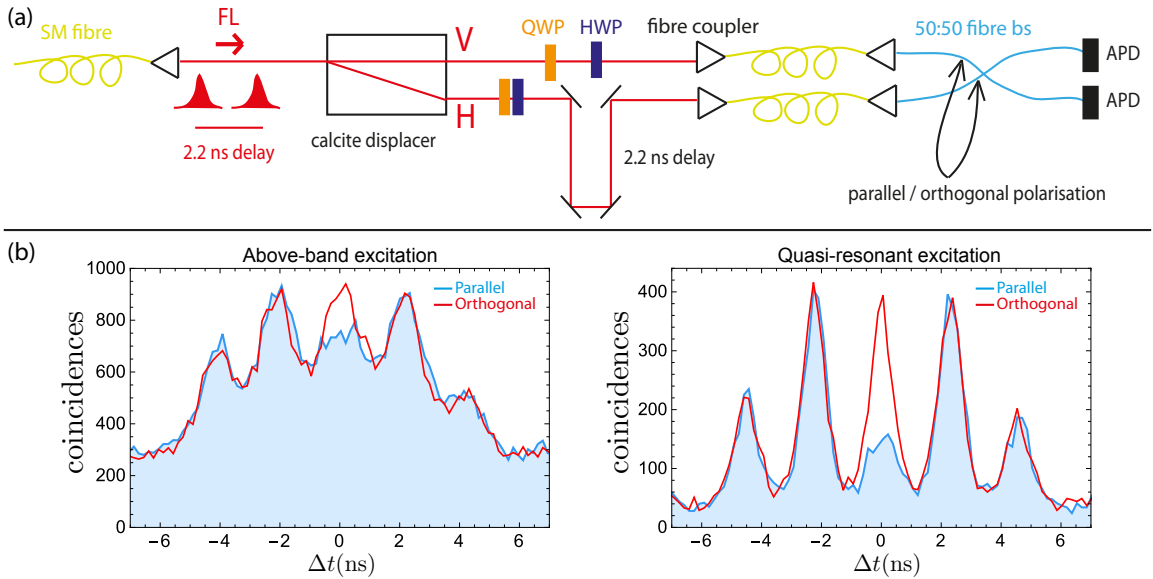
Figure 1.3: Two-photon interference from a quantum dot. (a) Schematics of the experimental setup. Two consecutive photons traverse an unbalanced Mach-Zehnder interferometer (between the calcite displacer and 50:50 fibre beamsplitter), and their polarisation are set, by means of quarter- (QWP) and half-wave plates (HWP), to either parallel (exhibiting photon bunching), or orthogonal configuration (corresponding to completely distinguishable particles). (b) HOM measurement results. The suppression of the peak around zero delay is a signature of two-photon quantum interference. A clear improvement is observed under quasi-resonant excitation with $\mathcal{I}\sim70\%$, as compared to above-band pump where $\mathcal{I}\sim10\%$ is observed.

In order to measure the indistinguishability between consecutively emitted photons, we use the setup depicted in Fig. 1.3(a). Two consecutive photons separated by 2.2 ns are probabilistically split in a calcite displacer; an optical path delay of the same length is introduced in one spatial mode; and both photons, in different temporal bins, probabilistically meet in a 50:50 beamsplitter. A suppression of coincidence counts around zero delay results from a finite degree of indistinguishability. Figures 1.3(b) shows HOM measurements under above-band (left) and quasi-resonant (right) excitation for both orthogonally-polarised photons (red)—thus completely distinguishable—and parallel-polarised photons (blue) exhibiting photon bunching.

16

1.3   SPDC source

In Spontaneous Parametric Downconversion, a non-linear crystal is pumped by laser light and occasionally one pump photon of higher energy is converted into two photons of lower energies, such that energy and momentum are conserved. In our case at the QTLAB, a *beta*-barium borate (BBO) crystal is pumped by a frequency-doubled mode-locked femtosecond Ti:Sapphire laser operating at a 76 MHz repetition rate. The state at the output of this process is a two-mode squeezed state, and it can be written as [45]:

$$|\Psi_{SPDC}\rangle = \sqrt{1 - |\lambda|^2} \sum_{n=0}^{\infty} \lambda^n |n, n\rangle, \tag{1.12}$$

where λ is the squeezing parameter ($|\lambda|^2$ is proportional to the laser pump power), and $|n, n\rangle$ is the two-mode n-photon Fock state. Thus, the probability of creating n photon pairs is simply given by $p(n) = (1 - |\lambda|^2)|\lambda|^{2n}$.

Here, it is useful to notice that $p(n+1)/p(n) = |\lambda|^2$. That is, the ratio between the probability of creating $n+1$ photon pairs to that of n pairs is determined by—and increases monotonically with—$|\lambda|$. Therefore, although mostly consisting of vacuum, if one wishes to operate $|\Psi_{SPDC}\rangle$ as a heralded single-photon source $|1, 1\rangle$—where the detection of one photon flags the presence of its *twin* photon—then the source must be run at low pump powers to achieve $|\lambda| \ll 1$, so that the probability of creating $|2, 2\rangle$ states (or other higher-order terms) in Eq. (1.12) remains negligible compared to the only non-zero order state of interest $|1, 1\rangle$. These higher-order terms are responsible of degrading the visibility of two-photon interference experiments and thus decreasing the performance of quantum information protocols [64].
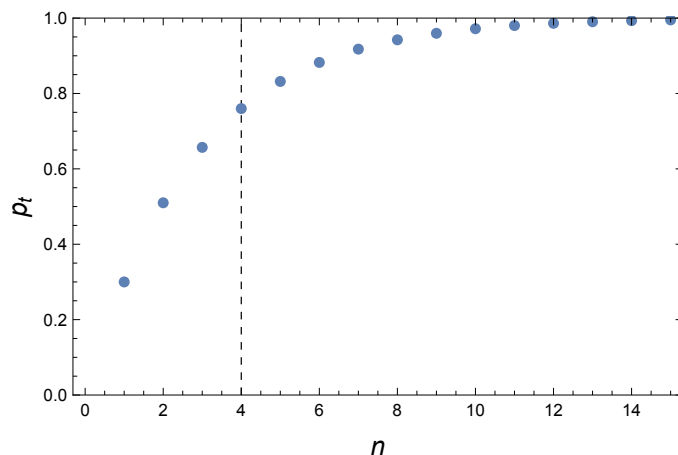
Figure 1.4: Probability of detecting $|n\rangle$ with a non number-resolving detector after setup losses characterised by a transmittance $t=0.3$. The dashed vertical line indicates a region (left), with $n<4$, containing the "stronger" terms contributing to $|\Psi_{SPDC}\rangle$.

However, keeping $|\lambda|$ too small importantly reduces the available count rates in an experiment. We must therefore optimise a trade-off for how large $|\lambda|$ can be as to provide decent

event rates while simultaneously being small enough to minimise the impact of higher-order terms. It turns out that these terms are more likely to be detected after setup loses. This can be seen from considering a simple model for optical losses: losses in one spatial mode are assumed to be the result of tracing out the reflecting port of a beam-splitter with transmittance t. It can be shown that, with an "on-off" detector, the term $|n\rangle$ is measured with a probability $p_t(n){=}1 - (1 - t)^n$, see Fig. (1.4). Limited detector efficiency can also be modeled as optical loss followed by detection with unity efficiency.

It is clear from the above that a pump-dependent analysis must be carried out to quantify the impact of higher-order terms on the performance of SPDC sources. First, we parameterise $|\lambda|$ in relation to the employed pump powers. This should be done at the lowest powers available, where detected rates of singles and coincidences reveal the corresponding value for $|\lambda|^2$. Then, $|\lambda|^2$ is simply proportional to the pump power. Furthermore, to compare its brightness against solid-state sources, here we use the average photon number per mode $\mu{=}\langle\hat{n}\otimes\hat{I}\rangle{=}\langle\hat{I}\otimes\hat{n}\rangle{=}|\lambda|^2/(1 - |\lambda|^2)$ as the brightness for SPDC sources. This is a reasonable brightness parameter as it represents, in the limit $|\lambda| \ll 1$, the probability per laser-pulse for one downconverted event to reach the first setup lens, and it also accounts for small contributions from higher-order events intrinsic to this source.
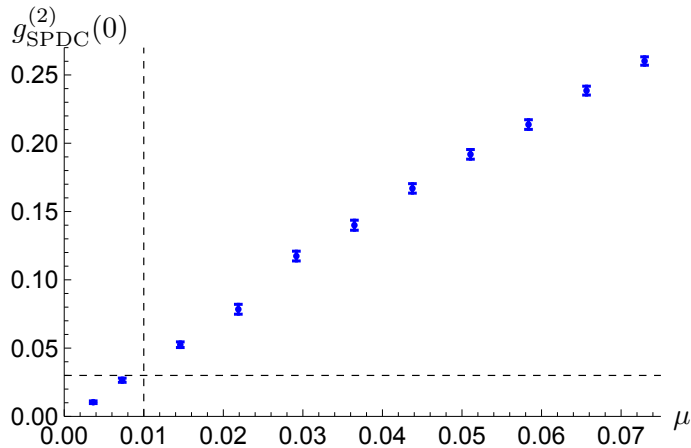
Figure 1.5: Heralded second-order autocorrelation function in our SPDC source. A high-purity single-photon source ($g_{\mathrm{SPDC}}^{(2)}(0){<}0.03$) is obtained for a brightness $\mu{<}0.01$.

The second-order autocorrelation function in a SPDC source is measured for one downconverted mode conditioned on the detection of its partner: A (heralding) detector is located on one arm (mode), and a standard Hanbury-Brown and Twiss (HBT) setup[23] is placed on the other arm with two detectors at its output. By measuring single counts, double, and triple coincidences, the *heralded* $g_{\mathrm{SPDC}}^{(2)}(0)$ is obtained via [65]:

$$g_{\mathrm{SPDC}}^{(2)}(0) = \frac{c_{\mathrm{h},1,2}c_{\mathrm{h}}}{c_{\mathrm{h},1}c_{\mathrm{h},2}}, \tag{1.13}$$

where c_{h} is the singles count rate on the heralding arm, $c_{\mathrm{h},1}$ ($c_{\mathrm{h},2}$) is the coincidence count

---

[23]This consists of one balanced 2×2 beamsplitter and one detector at the each output.

rate between the heralding detector and the first (second) detector at the output of the HBT setup, and $c_{\mathrm{h},1,2}$ is the triple coincidence count rate between the heralding, first, and second detector. Figure 1.5 shows our measured $g_{\mathrm{SPDC}}^{(2)}(0)$ as a function of the SPDC brightness μ. The SPDC single-photon purity is degraded with increasing brightness, and high purity levels $(g_{\mathrm{SPDC}}^{(2)}(0){<}0.03)$ are found only for low values of brightness $(\mu{<}0.01)$.
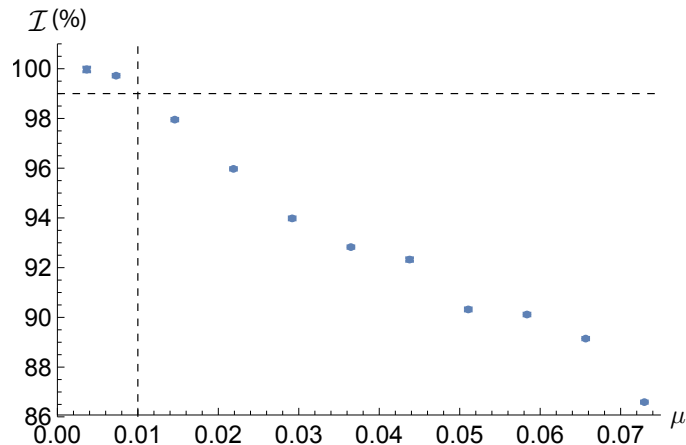
Figure 1.6: Photon indistinguishability in our SPDC source. Indistinguishability monotonically decreases with brightness. Dashed lines indicate that highly indistinguishable photons $(\mathcal{I}{>}99\%)$ are obtained only for a brightness $\mu{<}0.01$.

Spontaneous parametric downconversion provides photons with high degrees of indistinguishabilities. Figure 1.6 shows the indistinguishability between photons of the same downconverted pair for various values of brightness. Previous works have identified the higher-order terms to be the main cause of performance degradation [64], thus this observed decreased indistinguishability[24] with increasing brightness is primarily due to the higher-order terms and do not originate from a "true" increase of photon distinguishability.

---

[24]Strictly speaking, it is the two-photon interference visibility the one that is decreased, but "indistinguishability" is still used for consistency with the rest of the work.

References

[1] Eisaman, M. D., Fan, J., Migdall, A. & Polyakov, S. V. Invited review article: Single-photon sources and detectors. *Review of Scientific Instruments* **82** (2011).

[2] Darquié, B. *et al.* Controlled single-photon emission from a single trapped two-level atom. *Science* **309**, 454–456 (2005).

[3] Kuhn, A., Hennrich, M., Bondo, T. & Rempe, G. Controlled generation of single photons from a strongly coupled atom-cavity system. *Applied Physics B* **69**, 373–377 (1999).

[4] Hennrich, M., Legero, T., Kuhn, A. & Rempe, G. Vacuum-stimulated raman scattering based on adiabatic passage in a high-finesse optical cavity. *Phys. Rev. Lett.* **85**, 4872–4875 (2000).

[5] Kuhn, A., Hennrich, M. & Rempe, G. Deterministic single-photon source for distributed quantum networking. *Phys. Rev. Lett.* **89**, 067901 (2002).

[6] Moehring, D. L. *et al.* Quantum networking with photons and trapped atoms (invited). *J. Opt. Soc. Am. B* **24**, 300–315 (2007).

[7] Almendros, M. *et al.* Bandwidth-tunable single-photon source in an ion-trap quantum network. *Phys. Rev. Lett.* **103**, 213601 (2009).

[8] Barros, H. G. *et al.* Deterministic single-photon source from a single ion. *New Journal of Physics* **11**, 103004 (2009).

[9] De Martini, F., Di Giuseppe, G. & Marrocco, M. Single-mode generation of quantum photon states by excited single molecules in a microcavity trap. *Phys. Rev. Lett.* **76**, 900–903 (1996).

[10] Brunel, C., Lounis, B., Tamarat, P. & Orrit, M. Triggered source of single photons based on controlled single molecule fluorescence. *Phys. Rev. Lett.* **83**, 2722–2725 (1999).

[11] Lounis, B. & Moerner, W. E. Single photons on demand from a single molecule at room temperature. *Nature* **407**, 491–493 (2000).

[12] Wrigge, G., Gerhardt, I., Hwang, J., Zumofen, G. & Sandoghdar, V. Efficient coupling of photons to a single molecule and the observation of its resonance fluorescence. *Nat Phys* **4**, 60–66 (2008).

[13] Brouri, R., Beveratos, A., Poizat, J.-P. & Grangier, P. Photon antibunching in the fluorescence of individual color centers in diamond. *Opt. Lett.* **25**, 1294–1296 (2000).

[14] Kurtsiefer, C., Mayer, S., Zarda, P. & Weinfurter, H. Stable solid-state source of single photons. *Phys. Rev. Lett.* **85**, 290–293 (2000).

[15] Riedel, D. *et al.* Low-loss broadband antenna for efficient photon collection from a coherent spin in diamond. *Phys. Rev. Applied* **2**, 064011 (2014).

[16] Kim, J., Benson, O., Kan, H. & Yamamoto, Y. A single-photon turnstile device. *Nature* **397**, 500–503 (1999).

[17] Michler, P. *et al.* Quantum correlation among photons from a single quantum dot at room temperature. *Nature* **406**, 968–970 (2000).

[18] Santori, C., Pelton, M., Solomon, G., Dale, Y. & Yamamoto, Y. Triggered single photons from a quantum dot. *Phys. Rev. Lett.* **86**, 1502–1505 (2001).

[19] Press, D. *et al.* Photon antibunching from a single quantum-dot-microcavity system in the strong coupling regime. *Phys. Rev. Lett.* **98**, 117402 (2007).

[20] Kwiat, P. G., Waks, E., White, A. G., Appelbaum, I. & Eberhard, P. H. Ultrabright source of polarization-entangled photons. *Phys. Rev. A* **60**, R773–R776 (1999).

[21] Tanida, M., Okamoto, R. & Takeuchi, S. Highly indistinguishable heralded single-photon sources using parametric down conversion. *Opt. Express* **20**, 15275–15285 (2012).

[22] Hong, C. K. & Mandel, L. Experimental realization of a localized one-photon state. *Phys. Rev. Lett.* **56**, 58–60 (1986).

[23] Kaneda, F. *et al.* Time-multiplexed heralded single-photon source. *Optica* **2**, 1010–1013 (2015).

[24] Mendoza, G. J. *et al.* Active temporal and spatial multiplexing of photons. *Optica* **3**, 127–132 (2016).

[25] Xiong, C. *et al.* Active temporal multiplexing of indistinguishable heralded single photons. *Nat Commun* **7**, 10853 (2016).

[26] Lodahl, P., Mahmoodian, S. & Stobbe, S. Interfacing single photons and single quantum dots with photonic nanostructures. *Rev. Mod. Phys.* **87**, 347–400 (2015).

[27] G., L. *et al.* A planar dielectric antenna for directional single-photon emission and near-unity collection efficiency. *Nat Photon* **5**, 166–169 (2011).

[28] Chen, X.-W., Götzinger, S. & Sandoghdar, V. 99% efficiency in collecting photons from a single emitter. *Opt. Lett.* **36**, 3545–3547 (2011).

[29] Chen, X.-W., Agio, M. & Sandoghdar, V. Metallodielectric hybrid antennas for ultrastrong enhancement of spontaneous emission. *Phys. Rev. Lett.* **108**, 233001 (2012).

[30] Chu, X.-L. *et al.* Experimental realization of an optical antenna designed for collecting 99% of photons from a quantum emitter. *Optica* **1**, 203–208 (2014).

[31] Unsleber, S. *et al.* Deterministic generation of bright single resonance fluorescence photons from a purcell-enhanced quantum dot-micropillar system. *Opt. Express* **23**, 32977–32985 (2015).

[32] Ding, X. *et al.* On-demand single photons with high extraction efficiency and near-unity indistinguishability from a resonantly driven quantum dot in a micropillar. *Phys. Rev. Lett.* **116**, 020401 (2016).

[33] Gazzano, O. *et al.* Bright solid-state sources of indistinguishable single photons. *Nat Commun* **4**, 1425 (2013).

[34] Nowak, A. K. *et al.* Deterministic and electrically tunable bright single-photon source. *Nat Commun* **5** (2014).

[35] Gschrey, M. *et al.* Highly indistinguishable photons from deterministic quantum-dot microlenses utilizing three-dimensional in situ electron-beam lithography. *Nat Commun* **6** (2015).

[36] Somaschi, N. *et al.* Near-optimal single-photon sources in the solid state. *Nat Photon* **advance online publication**, – (2016).

[37] Unsleber, S. *et al.* Highly indistinguishable on-demand resonance fluorescence photons from a deterministic quantum dot micropillar device with 75% extraction efficiency. *arXiv:1512.07453* (2015).

[38] Arcari, M. *et al.* Near-unity coupling efficiency of a quantum emitter to a photonic crystal waveguide. *Phys. Rev. Lett.* **113**, 093603 (2014).

[39] Söllner, I. *et al.* Deterministic photon–emitter coupling in chiral photonic circuits. *Nat Nano* **10**, 775–778 (2015).

[40] Reithmaier, G. *et al.* On-chip generation, routing, and detection of resonance fluorescence. *Nano Letters* **15**, 5208–5213 (2015). PMID: 26102603, `http://dx.doi.org/10.1021/acs.nanolett.5b01444`.

[41] Scully, M. O. & Zubairy, M. S. Quantum optics. *Cambridge: Cambridge University Press* (1997).

[42] Bouwmeester, D. *et al.* Experimental quantum teleportation. *Nature* **390**, 575–579 (1997).

[43] Wang, X.-L. *et al.* Quantum teleportation of multiple degrees of freedom of a single photon. *Nature* **518**, 516–519 (2015).

[44] Knill, E., Laflamme, R. & Milburn, G. J. A scheme for efficient quantum computation with linear optics. *Nature* **409**, 46–52 (2001).

[45] Kok, P. *et al.* Linear optical quantum computing with photonic qubits. *Rev. Mod. Phys.* **79**, 135–174 (2007).

[46] Hong, C. K., Ou, Z. Y. & Mandel, L. Measurement of subpicosecond time intervals between two photons by interference. *Phys. Rev. Lett.* **59**, 2044–2046 (1987).

[47] Legero, T., Wilk, T., Hennrich, M., Rempe, G. & Kuhn, A. Quantum beat of two single photons. *Phys. Rev. Lett.* **93**, 070503 (2004).

[48] Duan, L.-M. & Monroe, C. *Colloquium* : Quantum networks with trapped ions. *Rev. Mod. Phys.* **82**, 1209–1224 (2010).

[49] Bernien, H. *et al.* Two-photon quantum interference from separate nitrogen vacancy centers in diamond. *Phys. Rev. Lett.* **108**, 043604 (2012).

[50] Kiraz, A. *et al.* Indistinguishable photons from a single molecule. *Phys. Rev. Lett.* **94**, 223602 (2005).

[51] Lang, C. *et al.* Correlations, indistinguishability and entanglement in hong-ou-mandel experiments at microwave frequencies. *Nat Phys* **9**, 345–348 (2013).

[52] Pittman, T., Jacobs, B. & Franson, J. Heralding single photons from pulsed parametric down-conversion. *Optics Communications* **246**, 545 – 550 (2005).

[53] Santori, C., Fattal, D., Vuckovic, J., Solomon, G. S. & Yamamoto, Y. Indistinguishable photons from a single-photon device. *Nature* **419**, 594–597 (2002).

[54] Walborn, S. P., de Oliveira, A. N., Pádua, S. & Monken, C. H. Multimode hong-ou-mandel interference. *Phys. Rev. Lett.* **90**, 143601 (2003).

[55] Tillmann, M. *et al.* Generalized multiphoton quantum interference. *Phys. Rev. X* **5**, 041015 (2015).

[56] Buckley, S., Rivoire, K. & Vuçkoviá, J. Engineered quantum dot single-photon sources. *Reports on Progress in Physics* **75**, 126503 (2012).

[57] Akopian, N. *et al.* Entangled photon pairs from semiconductor quantum dots. *Phys. Rev. Lett.* **96**, 130501 (2006).

[58] Muller, A., Fang, W., Lawall, J. & Solomon, G. S. Creating polarization-entangled photon pairs from a semiconductor quantum dot using the optical stark effect. *Phys. Rev. Lett.* **103**, 217402 (2009).

[59] Dousse, A. *et al.* Ultrabright source of entangled photon pairs. *Nature* **466**, 217–220 (2010).

[60] Imamoglu, A. *et al.* Quantum information processing using quantum dot spins and cavity qed. *Phys. Rev. Lett.* **83**, 4204–4207 (1999).

[61] Atatüre, M. *et al.* Quantum-dot spin-state preparation with near-unity fidelity. *Science* **312**, 551–553 (2006).

[62] Nick Vamivakas, A., Zhao, Y., Lu, C.-Y. & Atature, M. Spin-resolved quantum-dot resonance fluorescence. *Nat Phys* **5**, 198–202 (2009).

[63] Hansom, J. *et al.* Environment-assisted quantum control of a solid-state spin via coherent dark states. *Nat Phys* **10**, 725–730 (2014).

[64] Weinhold, T. J. *et al.* Understanding photonic quantum-logic gates: The road to fault tolerance. *arXiv:0808.0794* (2008).

[65] Grangier, P., Roger, G. & Aspect, A. Experimental evidence for a photon anticorrelation effect on a beam splitter: A new light on single-photon interferences. *Europhys. Lett.* **1**, 173–179 (1986).

CHAPTER 2

Observation of entanglement-dependent two-particle holonomic phase

J. C. Loredo, M. A. Broome, D. H. Smith, A. G White

Centre for Engineered Quantum Systems, Centre for Quantum Computer and Communication Technology, and School of Mathematics and Physics, University of Queensland, Brisbane, QLD 4072, Australia

Holonomic phases, geometric and topological, have long been an intriguing aspect of physics. They are ubiquitous, ranging from observations in particle physics to applications in fault tolerant quantum computing. However, their exploration in particles sharing genuine quantum correlations lack in observations. Here we experimentally demonstrate the holonomic phase of two entangled-photons evolving locally, which nevertheless gives rise to an entanglement-dependent phase. We observe its transition from geometric to topological as the entanglement between the particles is tuned from zero to maximal, and find this phase to behave more resilient to evolution changes with increasing entanglement. Furthermore, we theoretically show that holonomic phases can directly quantify the amount of quantum correlations between the two particles. Our results open up a new avenue for observations of holonomic phenomena in multi-particle entangled quantum systems.

2.1   Introduction

$\mathbf{I}$N differential geometry, holonomy accounts for the difference between a parallel-transported vector along a geodesic—i.e. shortest path—and any other curve. It is a direct manifestation of the geometry *and* topology of a given curved space. A physical system evolving in its own multi-dimensional parameter space will exhibit holonomies as a result of these geometric and topological structures. Consequently, holonomies have physical manifestations, ranging from Thomas precession to the Aharonov-Bohm effect.

In quantum systems, the holonomy manifests as a phase imparted on the wavefunction [1]. When the quantum parameter space is *simply* connected, holonomies are continuous-valued with respect to continuous deformations of the trajectory. These are geometric phases [2] and they depend on the space's curvature. Conversely, when the parameter space is not simply-connected discrete-valued topological phases appear [3, 4]. We refer to both geometric and topological as holonomic phases.

Holonomies are of fundamental interest and have important applications, for example, in holonomic quantum computation [5, 6, 7, 8], where matrix-valued geometric phase transformations play the role of quantum logic gates. This scheme has received a great deal of attention due to its potential to overcome decoherence [9], and has recently been experimentally realized in different architectures [10, 11].

In the quantum regime, holonomic phases have been observed in particles encoding one qubit [12, 13, 14], as well as two particle systems encoding uncorrelated two-qubit states [15]. In addition, topological phases have been observed in classical systems emulating the behaviour of entanglement, for example, so-called non-separable states between the polarization and transverse modes of a laser [16], or pseudo-entanglement in NMR [17]. Lacking up to now, however, is the exploration of holonomic phases between genuinely entangled quantum particles.

Here we demonstrate both geometric and topological phases appearing in the joint wavefunction of two separate, and genuinely-entangled, particles whose correlations can be tuned from vanishing to maximal.

2.2   Two-particle holonomic phase

To better elucidate two-qubit holonomic phases, consider an arbitrary two-qubit pure state written in its Schmidt decomposition:

$$|\psi(0)\rangle = e^{-i\beta/2}\cos\frac{\alpha}{2}|n_a m_b\rangle + e^{i\beta/2}\sin\frac{\alpha}{2}|n_a^\perp m_b^\perp\rangle, \tag{2.1}$$

where $\alpha \in [0, \pi]$ and $\beta \in [0, 2\pi]$ parametrise the Schmidt sphere [18] of a correlation space, and $|n_a m_b\rangle$, $|n_a^\perp m_b^\perp\rangle$ are orthogonal product states defining the Schmidt basis, see Fig. 2.1a, b. While a treatment of the two-qubit space can be carried out formally [19], it is more intuitive to represent evolutions in it with the trajectories that the reduced density matrices, ρ_a and ρ_b, undertake on their corresponding local Bloch spheres together with the curve that α and β

project onto the Schmidt sphere.

For a non-maximally entangled state, $|\psi(0)\rangle$ has preferred directions, given by unit vectors $\hat{a}$ and $\hat{b}$, on each qubit's Bloch sphere. That is, the reduced density matrix of, say, system a is given by $\rho_a = \text{Tr}_b(|\psi\rangle\langle\psi|) = \frac{1}{2}(\mathbb{I} + \cos\alpha\,\hat{a}\cdot\vec{\sigma})$, where $\vec{\sigma} = (\sigma_x, \sigma_y, \sigma_z)$ denote the Pauli matrices. Accordingly, $|\psi(0)\rangle$ spans a six-dimensional parameter space.
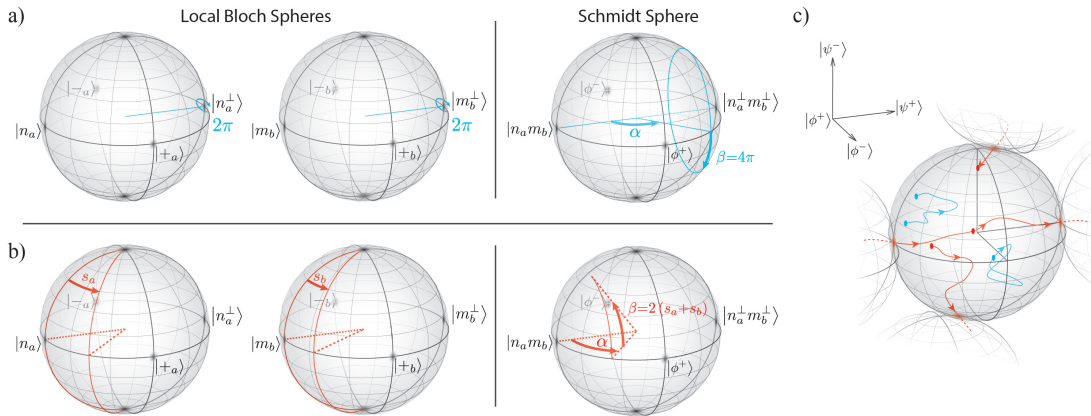
Figure 2.1: a) A cyclic Schmidt evolution with $\theta_S = 2\pi$. Left and middle spheres show trajectories traced out in the local Bloch spheres of each qubit defined in the Schmidt basis. Here, they evolve at a single point and therefore enclose no area, leading to no gain in holonomic phase. The right sphere represents the trajectory spanned by the evolution of α and β in the Schmidt sphere. In contrast to the local trajectories, a holonomic phase still arises as a result of the area enclosed by this trajectory. Equivalent Schmidt evolutions of non-entangled states induce a zero holonomic phase. b) In contrast, segmented evolutions defined by angles s_a and s_b induce holonomies appearing from both local and Schmidt spheres. The parameters s_a and s_b define the opening angles for the projected curves of ρ_a and ρ_b onto the local Bloch spheres. In the right sphere, a rotation angle $2(s_a + s_b) = \beta$ around $|n_a m_b\rangle$ also contributes to the holonomy. Equivalent evolutions of non-entangled states induce a non-zero holonomic phase. c) Depiction of the double-connected parameter space of maximally entangled states: SO(3) in $\mathbb{R}^3$ with a border at S_π^2. This border is a 2-sphere of radius π with identified antipodal points. Blue trajectories represent arbitrary evolutions for one homotopy-class along which no phase is gained. Red curves represent evolutions of the other homotopy-class after which a π phase appears on the wave-function.

From the state $|\psi(0)\rangle$, an entanglement-induced holonomic phase will appear as a result of the special "Schmidt evolution". We define a Schmidt evolution as a bi-local rotation of θ_S, of both qubits around their preferential directions $\hat{a}$ and $\hat{b}$, see Fig. 2.1a. The holonomic phase of this evolution is calculated—in the standard way—as a difference [20]

$$\Phi_h = \Phi_P - \Phi_{\text{dyn}}, \tag{2.2}$$

with $\Phi_P = \arg\langle\psi(0)|\psi(\tau)\rangle$ the Pancharatnam [21] and $\Phi_{\text{dyn}} = \text{Im}\int_0^\tau \langle\psi(t)|\dot{\psi}(t)\rangle dt$ the dynamical phase, and $|\psi(t)\rangle, t \in [0, \tau]$, denotes the evolving state.

While usually Φ_h is regarded as a geometric phase only [20], its value arises from both the geometry (curvature) *and* topology (connectedness) of the parameter space. It has therefore become more routine to identify parts of Φ_h as being of either geometric or topological origin [22]. For instance, maximally-entangled two-qubit pure states (MES) can only induce a phase of topological origin regardless of their evolution [3, 4, 22].

Canonically, the amount of entanglement in a two-qubit state can be measured by the tangle $\mathbb{T}$ (concurrence squared [23]). In a pure system as given in Eq. 2.1, it is determined by the relative populations of the Schmidt basis: $\mathbb{T} = \sin^2 \alpha$, and ranges from 0 for separable states up to 1 for maximally-entangled states. Consequently, a Schmidt evolution will give rise to, see Appendix, an entanglement-induced holonomic phase given by:

$$\Phi_h^{\text{ent}} = \arg\left(\cos\theta_{\text{S}} - i\sqrt{1-\mathbb{T}}\sin\theta_{\text{S}}\right) + \theta_{\text{S}}\sqrt{1-\mathbb{T}}. \tag{2.3}$$

Importantly, Φ_h^{ent} behaves monotonically with the amount of entanglement, measuring 0 for separable states and its maximum for MES (value depended on θ_{S}). For instance, for the evolution depicted in Fig. 2.1a, $\theta_{\text{S}}=2\pi$, and $\Phi_h^{\text{ent}} = -2\pi\left(1 - \sqrt{1-\mathbb{T}}\right)$. While there are extensive theoretical studies of holonomic phases in mixed, as well as pure, entangled systems [24, 25, 26], it remains an open question as to whether a holonomic phase quantifying entanglement can be found for mixed states.

Recalling that experimentally it is the total Pancharatnam phase that is observed [27], we can choose evolutions for which the dynamical component vanishes, ensuring the total phase gained is holonomic in nature only. We achieve this using the the bi-local segmented evolutions characterised by the opening angles s_a and s_b on qubits a and b respectively, see Fig. 2.1b. These trajectories are connected geodesics, meaning any dynamical phase is identically zero. However, not being Schmidt evolutions, the holonomic phase arises from trajectories in *both* local and Schmidt spheres, but importantly remains monotonic with entanglement:

$$\Phi_h = \mp \arctan\left(\sqrt{1-\mathbb{T}}\tan(2s)\right), \tag{2.4}$$

where the sign is $-$ ($+$) if the joint state is more populated in $|n_a m_b\rangle$ ($|n_a^{\perp} m_b^{\perp}\rangle$) of the Schmidt basis, see Appendix, and s defines the evolution undertaken by $|\psi(0)\rangle$. In Eq. (2.4), the opening angles $s_a = s_b = s$.

One important feature of the state in Eq. (2.1) is the change that occurs to the parameter space as a result of increasing tangle. As $\mathbb{T}\to1$, previously separated states in the two-qubit parameter space become less distinguishable, and eventually some become identical at $\mathbb{T}=1$. At this point the parameter space collapses from six to three dimensions represented by the double-connected SO(3) ball [3, 4], see Fig. 2.1c. Spaces of this kind—not simply connected—allow state trajectories that are topologically distinct, i.e. cannot be continuously transformed into one another.

Trajectories in the SO(3) ball are classified by two different homotopy-class families: those that cross the border S_{π}^2—a 2-sphere of radius π—an odd number of times and those crossing

it an even number of times (zero included). Physically, crossing S_π^2 l-times results in a $l\pi$ phase on the wavefunction. For instance, if $\alpha=\pi/2$ in the Schmidt evolution shown in Fig. 2.1a, then its trajectory in SO(3) crosses S_π^2 twice, picking up a 2π topological phase.

2.3   Experimental implementation

In order to observe the entanglement-dependent holonomic phase given by Eq. (2.4), we implement a method, depicted in Fig. 2.2, that works as follows: We generate a two-qubit state, $|\psi\rangle$, in the polarization of two single-photons whose tangle can be tuned from $\mathbb{T}=0\rightarrow1$ [28, 29]. Upon meeting at the first 50:50 beam-splitter BS1 of the interferometer depicted in Fig. 2.2a, the photons are subject to non-classical interference [30], after which they exit via the same spatial mode. Regardless of the specific form of $|\psi\rangle$, photon bunching can always be achieved by engineering other degrees of freedom if necessary [31]. Consequently, the joint state of the system, $|\psi\rangle$, remains in either of the two paths of the interferometer, whose optical path lengths are equal. The joint state then undergoes a polarization evolution, composed of two auxiliary evolutions $\breve{U}$ and U in separate paths of the interferometer.
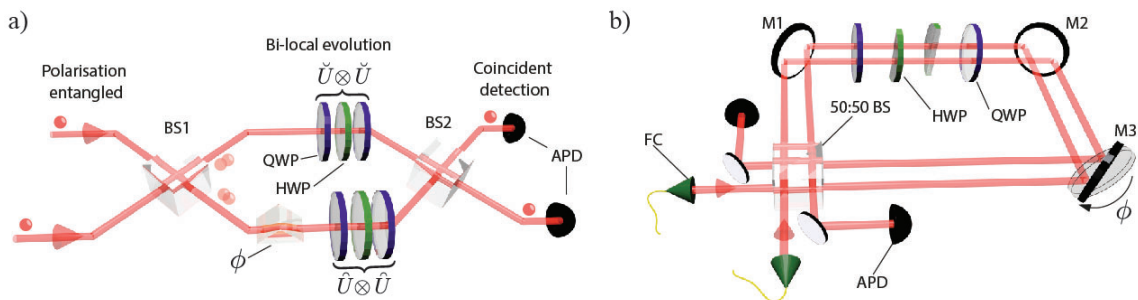
Figure 2.2: a) Depiction of the experimental method. Two indistinguishable photons, encoding a two-qubit entangled state $|\psi\rangle$ in their polarization, pass through an interferometer and are detected in coincidence with avalanche-photo-diodes (APD) at the output. Due to the Hong-Ou-Mandel effect at the first beam-splitter BS1, a coincidence signal c after the exit of the interferometer through BS2, cannot distinguish between different paths travelled in the interferometer. The resulting holonomic phase gained by the evolved state $|\psi'\rangle=U^\dagger\breve{U} \otimes U^\dagger\breve{U}|\psi\rangle$, as well as the phase ϕ, thus appear as a modulation in the coincidence given by $c \propto |e^{2i\phi}|\psi\rangle+|\psi'\rangle|^2$. b) Experimental implementation of the method. Single photons are injected via single-mode fibre couplers (FC) into a displaced-Sagnac interferometer configuration, composed of one 50:50 beam-splitter (BS) and three mirrors M1-3. Polarisation evolution is performed using two common-path quarter wave-plates QWP and two semi-circular half wave-plates HWP in separate optical paths. Mirror M3 is rotated via a micro-translation stage to control ϕ.

The information about which-path the photons followed is erased by a second 50:50 beam-splitter BS2, after which point the photons are detected. As such, the two-photon coincidence signal, c, will exhibit interference behaviour modulated by all relative phases between the two arms of the interferometer. That is, caused by a physical optical path-difference phase ϕ and

the Pancharatnam phase Φ_P arising from the polarization evolutions.

We prepared the initial polarization-entangled state $|\psi\rangle = \cos\frac{\alpha}{2}|HH\rangle + \sin\frac{\alpha}{2}|VV\rangle$, where α is a tuneable parameter defining the amount of entanglement $\mathbb{T} = \sin^2\alpha$, and $|H\rangle$ and $|V\rangle$ denote the horizontal and vertical polarizations. The state is injected into a displaced-Sagnac interferometer configuration, shown in Fig. 2.2b, where no active path locking is required. Using the notation $\sigma_1 = |H\rangle\langle H| - |V\rangle\langle V|$ and $\sigma_2 = |H\rangle\langle V| + |V\rangle\langle H|$, we choose an evolution

$$U \equiv U^\dagger \breve{U} = e^{i\frac{\pi}{4}\sigma_2} e^{-i\frac{\pi}{2}(\sigma_1 \sin s + \sigma_2 \cos s)} e^{i\frac{\pi}{4}\sigma_2}, \tag{2.5}$$

where s equals the opening angles of the corresponding geodesic trajectories in the local spaces, see Fig. 2.1b. Since the evolutions $\breve{U}$ and U are chosen to induce no dynamical phase, from Eq. 2.2 the Pancharatnam phase matches the holonomic phase. Thus by controlling the variable phase ϕ—introduced by slightly rotating the mirror M3 of the interferometer, see Fig. 2.2b—the two-photon coincidence will modulate as:

$$
\begin{aligned}
c &= \frac{1}{4}\left| e^{2i\phi}|\psi\rangle + (U^\dagger\breve{U} \otimes U^\dagger\breve{U})|\psi\rangle \right|^2 \\
&= \frac{1}{2}\left[1 + v\cos(2\phi - \Phi_h)\right],
\end{aligned}
\tag{2.6}
$$

where $v = |\langle\psi|\psi'\rangle|$ is the interference visibility and $\Phi_h = \arg\langle\psi|\psi'\rangle$ is the holnomic phase gained during the effective evolution $|\psi'\rangle = U\otimes U|\psi\rangle$. Consequently, we can determine Φ_h by measuring coincidence modulation as a function of ϕ, see Appendix.

The polarization evolution in Eq. 2.5 is implemented using quarter- Q and half-wave-plates H in the arrangement $U = Q(-\frac{\pi}{4})H(\frac{\pi}{4} - \frac{s}{2})Q(-\frac{\pi}{4})$, where the arguments inside parentheses indicate the angle of the wave-plate optic axis in the laboratory frame. This unitary evolution is built from auxiliaries in separate arms of the interferometer, given by $\breve{U} = Q(-\frac{\pi}{4})H(\frac{\pi}{4} - \frac{s}{4})Q(-\frac{\pi}{4})$ and $U = Q(\frac{\pi}{4})H(-\frac{\pi}{4} - \frac{s}{4})Q(\frac{\pi}{4})$. Physically, we perform these evolutions using two common-path quarter-wave-plates with angles fixed at $-\frac{\pi}{4}$ and two semi-circular half-wave-plates, one in each path, see Fig. 2.2b.

Figure 2.3a shows our predicted and measured results for Φ_h, as a function of entanglement represented by α, and the opening angle s of the trajectories. The solid and dashed black lines in Fig. 2.3b show theoretical predictions for the bipartite holonomic phase for a fitted value of tangle, $\mathbb{T} = 0.01 \pm 0.01$. In this case the holonomy is simply the sum of individual geometric phases $\Phi_h^{\text{sep}} = \mp(s+s)$.

Conversely, as the amount of entanglement increases to a maximum, i.e. as $\alpha \to \pi/2$, the holonomic phase becomes less affected by changes in the trajectory angle s. Instead, two attractors at $\Phi_h = 0$ and $\Phi_h = \pi$ appear, becoming its only possible values when $\mathbb{T} = 1$, shown by the solid-red curves in Fig. 2.3b. Thus, the tuning from $\alpha = 0 \to \alpha = \pi/2$ results in a geometric-to-topological transition of the holonomic phase. The solid and dashed blue curves in Fig. 2.3b show our measurements for the fitted value of tangle, $\mathbb{T} = 0.99 \pm 0.01$.

This reported tangle is the best-fitted value to our data using Eq. (2.4). To confirm the presence of a high amount of entanglement, we carried out a full quantum state tomography of
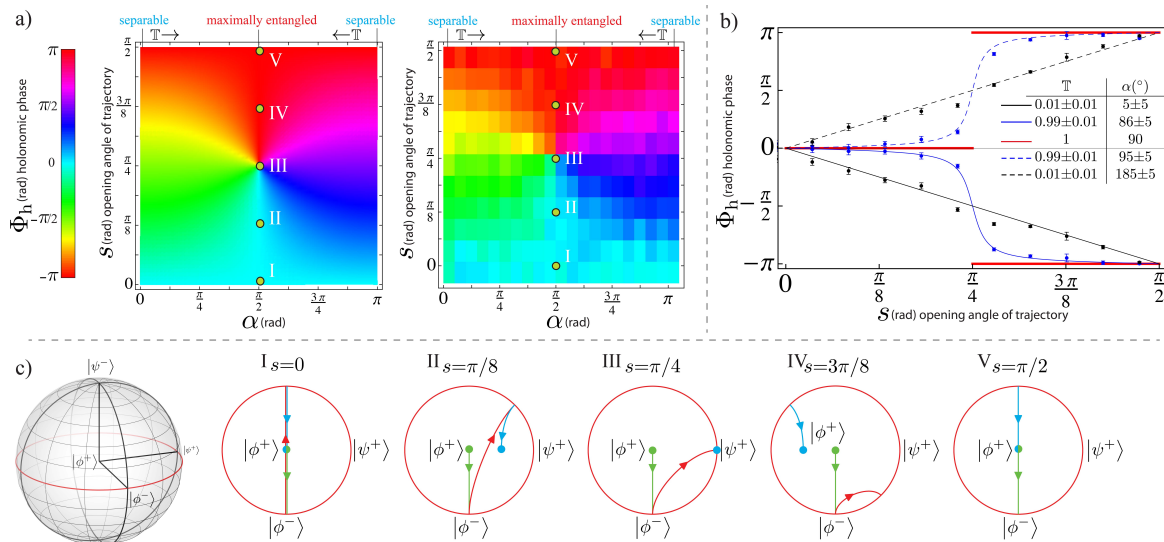
Figure 2.3: Experimental results. a) In a cyclic colour-scale, predicted (left) and measured (right) results for $\Phi_h = -\arctan\left(\cos(\alpha)\tan(2s)\right)$ (equivalent to Eq. (2.4)). Centres of the rectangular measured data blocks represent the corresponding (α, s) coordinates. b) The black data points and theoretical curves correspond to measurements of holonomic phases with an initial state $|HH\rangle$ (solid curve) and $|VV\rangle$ (dashed curve) for a fitted level of tangle, $\mathbb{T}=0.01\pm0.01$. Blue data points and theoretical curves show the extent to which we observe the topological behaviour of Φ_h for a highly entangled state. Here the data is fitted to a state tangle of $\mathbb{T}=0.99\pm0.01$, for the cases in which $|\psi(0)\rangle$ is more populated by $|HH\rangle$ ($\alpha=\pi/2-\epsilon$) shown by the solid curve, and $|VV\rangle$ ($\alpha=\pi/2+\epsilon$) given by the dashed curve, for $0<\epsilon\ll1$. The red curve corresponds to the theoretical ideal case of $\mathbb{T}=1$. Errors are calculated via Poissonian counting statistics. c) Depiction of cyclic (I,V) and non-cyclic (II,III,IV) evolutions of MES in a plane of the double-connected SO(3) ball. Green, red and blue coloured-curves denote the first, second and third part of each evolution, respectively. Evolution III for which $s=\pi/4$, marks the switch between two distinct homotopy-classes, those that cross the S_π^2 border zero times (I and II) and one time (IV and V).

the two-photon state, resulting in a tangle of $\mathbb{T}_{tomo}=0.959\pm0.001$, see Appendix.

As discussed previously, when $\mathbb{T}=1$, the corresponding evolutions follow trajectories in the double-connected SO(3) space, thus giving rise to two topologically distinct paths. Figure 2.3c shows the corresponding paths for five such evolutions, for which the trajectory with $s=\frac{\pi}{4}$ represents the switch between two the distinct homotopy-classes.

Experiments [16, 17] observing such topological phases have been realised with cyclic evolutions using classical states that are formally equivalent to a MES, corresponding to the top and bottom data points at $\alpha=\pi/2$ in Fig. 2.3a. In contrast, we additionally demonstrated topological behaviour for explicitly non-cyclic evolutions, see Fig. 2.3c, of genuinely entangled quantum systems.

2.4 Discussion

We experimentally demonstrated that the wavefunction of a pair of qubits picks up a phase factor of holonomic nature in both cyclic and non-cyclic evolutions. In contrast to conventional measurements of single-qubit holonomic phases [12, 13], the phase shift observed in our work is dependent on genuine quantum correlations. We find that the holonomic phase becomes more resilient to evolution changes with increasing entanglement, which indicates that quantum correlations can be utilised to enhance holonomic robustness and there may be advantages in using not only geometric but the full range of holonomic phases. Naturally, this leads to the question as to whether more general forms of quantum correlations—most notably discord [32]—could be the underlying reason for this enhancement.

Finally, we derived an entanglement-induced holonomic phase that can be used to quantify the amount of quantum correlations between a pair of pure-state qubits. This result provides a measurable quantity arising solely from entanglement and it is a step in gaining a broader understanding of the geometric interpretation of quantum correlations. We expect that this work will strongly motivate new proposals for more robust holonomic quantum computation and trigger observations of holonomies in multi-partite entangled states of qubits or higher-dimensional qudit systems.

2.5 Appendix

2.5.1 Calculation of holonomic phase of entanglement

Consider the arbitrary initial two-qubit pure state written in its Schmidt decomposition,

$$|\psi(0)\rangle = \cos\frac{\alpha}{2}e^{-i\beta/2}|n_a m_b\rangle + \sin\frac{\alpha}{2}e^{i\beta/2}|n_a^\perp m_b^\perp\rangle, \tag{2.7}$$

which is then subject to a rotation of both qubits around their preferential directions $\hat{a}$ and $\hat{b}$ in their corresponding local Bloch spheres. That is, a bi-local rotation $U^{\mathcal{S}}(\theta)=U_a^{\mathcal{S}(n)}(\theta)\otimes U_b^{\mathcal{S}(m)}(\theta)$ such that $U_j^{\mathcal{S}(k)}(\theta) = \exp\left(-i\theta\sigma_j^{(k)}/2\right)$, where θ is the angle of rotation, $\sigma_j^{(k)} = \eta|k_j\rangle\langle k_j| - \eta|k_j^\perp\rangle\langle k_j^\perp|$, and η is the sign of $\cos\alpha$. The holonomic phase of such evolution can be calculated from the formula

$$\Phi_{\mathrm{h}} = \arg\langle\psi(0)|\psi(\theta)\rangle - \mathrm{Im}\int_0^\theta \langle\psi(\theta')|\dot{\psi}(\theta')\rangle d\theta', \tag{2.8}$$

where $\Phi_{\mathrm{P}}=\arg\langle\psi(0)|\psi(\theta)\rangle$ and $\Phi_{\mathrm{dyn}}=\mathrm{Im}\int_0^\theta\langle\psi(\theta')|\dot{\psi}(\theta')\rangle d\theta'$ are the Pancharatnam and dynamical phases respectively. This gives,

$$
\begin{aligned}
\arg\langle\psi(0)|\psi(\theta)\rangle &= \arg\left(\cos\theta - i\eta\cos\alpha\sin\theta\right) \\
&= \arg\left(\cos\theta - i|\cos\alpha|\sin\theta\right),
\end{aligned} \tag{2.9}
$$

and

$$
\begin{aligned}
\mathrm{Im}\int_0^\theta\langle\psi(\theta')|\dot{\psi}(\theta')\rangle d\theta' &= \mathrm{Im}\int_0^\theta -i\eta\cos\alpha\, d\theta' \\
&= -|\cos\alpha|\theta.
\end{aligned} \tag{2.10}
$$

Using the expression for the tangle $\mathbb{T}=\sin^2\alpha$, we find the holonomic phase of entanglement to be

$$\Phi_{\mathrm{h}}^{\mathrm{ent}} = \arg\left(\cos\theta - i\sqrt{1-\mathbb{T}}\sin\theta\right) + \theta\sqrt{1-\mathbb{T}}, \tag{2.11}$$

which for $\theta=2\pi$ takes the form

$$\Phi_{\mathrm{h}}^{\mathrm{ent}} = -2\pi\left(1 - \sqrt{1-\mathbb{T}}\right). \tag{2.12}$$

2.5.2 Holonomic phase in evolutions with vanishing dynamical phase

In our experiment we prepare the initial polarization-entangled state $|\psi\rangle=\cos\frac{\alpha}{2}|HH\rangle+\sin\frac{\alpha}{2}|VV\rangle$, where $|H\rangle$ and $|V\rangle$ denote horizontal and vertical polarizations respectively. We choose bi-local evolutions $U\otimes U$, with

$$U = e^{i\frac{\pi}{4}\sigma_2}e^{-i\frac{\pi}{2}(\sigma_1\sin s+\sigma_2\cos s)}e^{i\frac{\pi}{4}\sigma_2}, \tag{2.13}$$

where $\sigma_1=|H\rangle\langle H| - |V\rangle\langle V|$, $\sigma_2=|H\rangle\langle V| + |V\rangle\langle H|$ and s equals the opening angles of the trajectories projected onto the Bloch spheres. For this particular evolution, one can demonstrate that the dynamical phase vanishes at every step of the evolution. Then the holonomic phase is calculated as

$$\begin{aligned}\Phi_{\mathrm{h}} &= \arg\left(\cos 2s - i\cos\alpha\sin 2s\right)\\ &= -\arctan\left(\cos\alpha\tan 2s\right).\end{aligned} \tag{2.14}$$

Using $\cos\alpha=\eta\sqrt{1-\mathbb{T}}=\pm\sqrt{1-\mathbb{T}}$, where the sign is $+$ $(-)$ if $|HH\rangle$ $(|VV\rangle)$ is more populated, we find that

$$\Phi_{\mathrm{h}} = \mp\arctan\left(\sqrt{1-\mathbb{T}}\tan(2s)\right). \tag{2.15}$$

For equally-populated states (maximally-entangled states) the sign is irrelevant and the holonomic phase $\Phi_{\mathrm{h}}=\arg(\cos 2s)$ is topological, being $\Phi_{\mathrm{h}}=0$ for $\cos 2s \geq 0$, and $\Phi_{\mathrm{h}}=\pi$ for $\cos 2s < 0$.

2.5.3 Measurement of the coincidence signal

Ideally, two parameters, s and α, define the probability of detecting a coincidence event in the experimental set-up described in the main text:

$$c=\frac{1}{2}\left[1 + v_{\mathrm{t}}\cos(2\phi - \Phi_{\mathrm{h}})\right], \tag{2.16}$$

with $v_{\mathrm{t}}=\sqrt{(\cos 2s)^2 + (\cos\alpha\sin 2s)^2}$, and $\Phi_{\mathrm{h}}=-\arctan\left(\cos\alpha\tan 2s\right)$. Then, if N pairs of single-photons enter the set-up, theoretically we would observe a coincidence signal

$$c_{\mathrm{t}} = \frac{N}{2}\left[1 + v_{\mathrm{t}}\cos(2\phi - \Phi_{\mathrm{h}})\right], \tag{2.17}$$

which predicts a reference, i.e. $s=0$, theoretical visibility:

$$v_{\mathrm{t}}^{\mathrm{r}}\equiv\left(c_{\mathrm{t}}^{\mathrm{r,max}} - c_{\mathrm{t}}^{\mathrm{r,min}}\right)/\left(c_{\mathrm{t}}^{\mathrm{r,max}} + c_{\mathrm{t}}^{\mathrm{r,min}}\right)=1,\ \forall\alpha, \tag{2.18}$$

where max (min) stands for maximum (minimum) value with respect to ϕ.

Experimentally, however, we observe the reference counts dropping to a minimum of non-zero N_0 events, which decreases the signal visibility. Imperfect 50:50 beamsplitter reflection:transmission ratio, and higher-order photon pairs—mainly present in pulsed-pumped down-conversion sources—can decrease visibilities in interference experiments. However, in our case the former is measured to be 46:54 at the source-wavelength (820nm) and the latter are negligible as ours is a cw-pumped down-conversion source. Accordingly, these issues have a minor contribution on the reduced visibility. On the other hand, if fully distinguishable photons (outside the Hong-Ou-Mandel dip) enter our set-up, one can show that the reference interference probability oscillates between 1 and 1/2, giving a visibility of 1/3, which is in agreement with our observations outside the dip, see Fig. 2.5a. Thus, the degree of photon-distinguishability
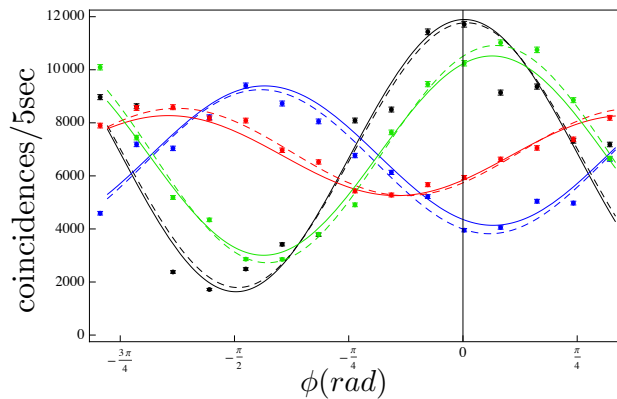
Figure 2.4: Counted coincidence events. The reference signal (solid black curve) was obtained from finding N^i and N_0^i by imposing $s^i=0$ and $\alpha^i=i\pi/20, i = 0, 1, ..., 20$ and averaging them to obtain $N=11911$ and $N_0=1616$, the phase origin, i.e. $\phi=0$, is set to be the average of their phases. Black points and dashed black curve represent the collected coincidence counts and best sinusoidal fit for $(s, \alpha)=(0, \frac{8}{20}\pi)$. Blue, red and green points and curves correspond to the predicted experimental coincidence signal (solid curves) c_e, see Eq. (2.19), and best sinusoidal fits (dashed curves) for $(s, \alpha)=(\frac{7}{10}\frac{\pi}{2}, \frac{8}{20}\pi)$, $(s, \alpha)=(\frac{6}{10}\frac{\pi}{2}, \frac{11}{20}\pi)$ and $(s, \alpha)=(\frac{3}{10}\frac{\pi}{2}, \frac{12}{20}\pi)$, respectively.

plays an important role and accounts for the reduced visibility, which in our experiment we believe arises from a temporal mode mismatch between the single photons.

The maximum and minimum number of experimental reference counts, $c_e^{r,\max}=N, c_e^{r,\min}=N_0$, give an experimental reference visibility $v_e^r = (N - N_0) / (N + N_0)$. Then, the correction for the experimental coincidence signal is given by

$$c_e = \frac{(N - N_0)}{2} \left[1 + v_t \cos(2\phi - \Phi_h)\right] + N_0, \qquad (2.19)$$

from where we can calculate the experimental visibility

$$v_e = v_t v_e^r, \qquad (2.20)$$

and, alternatively, write the experimental signal as

$$c_e = \frac{(N + N_0)}{2} \left[1 + v_e \cos(2\phi - \Phi_h)\right], \qquad (2.21)$$

with $0 \leq v_e \leq (N - N_0) / (N + N_0)$.

The path-difference phase ϕ is introduced by rotating a mirror mounted on a motorised stage capable of rotations in steps of $\sim 10^{-5}$ degrees, see Fig. 2b in main text. Complete cycles ($\phi \to 2\pi$) are obtained by physical rotations of the mirror of the order $\sim 10^{-4}$ degrees.

The reference coincidence signal, i.e. for $\Phi_h=0$, was obtained by imposing $s=0$ and averaging all phase offsets by varying α between $\alpha=0$ and $\alpha=\pi$ in steps of $\Delta\alpha=\pi/20$. A maximum in the reference signal is equivalent to $\sim 12,000$ coincidence events collected in 5 seconds. We measure ~ 10 kHz coincidences from the source, accordingly our set-up has $\sim 24\%$ overall transmission.

The experimental errors arise from instabilities, e.g. small mechanical fluctuations in the mirror position ($< 10^{-5}$ degrees), to which the Sagnac interferometer is sensitive to, in addition to inevitable random errors from Poissonian photon-counting statistics. Figure 2.4 shows our recorded coincidence signals for four cases.

2.5.4 Measurement of Φ_h without Hong-Ou-Mandel interference

Although the presented data in the main text was taken with indistinguishable photons (inside the Hong-Ou-Mandel dip), qualitatively similar measurements were obtained with distinguishable photons by moving the modes outside of the dip, see Fig. 2.5. Given our particular evolutions however, it can be shown that the anti-bunching terms observed when there is a degree of distinguishability between the photons (absent in the completely indistinguishable case) do not alter the measured holonomic phases, Φ_h. Instead, they show up merely as a background of counts, reducing the overall signal-to-noise ratio of the interference traces shown in Fig. 2.5. It was therefore not imperative to obtain perfect indistinguishability in order to measure the holonomic phases. Yet, any amount of indistinguishability will enhance the signal-to-noise ratio above that of the completely distinguishable case. A comparison between our measurements outside the Hong-Ou-Mandel dip (fully distinguishable) and the corresponding data inside the Hong-Ou-Mandel dip (indistinguishable), are shown in Fig. 2.5a-c.
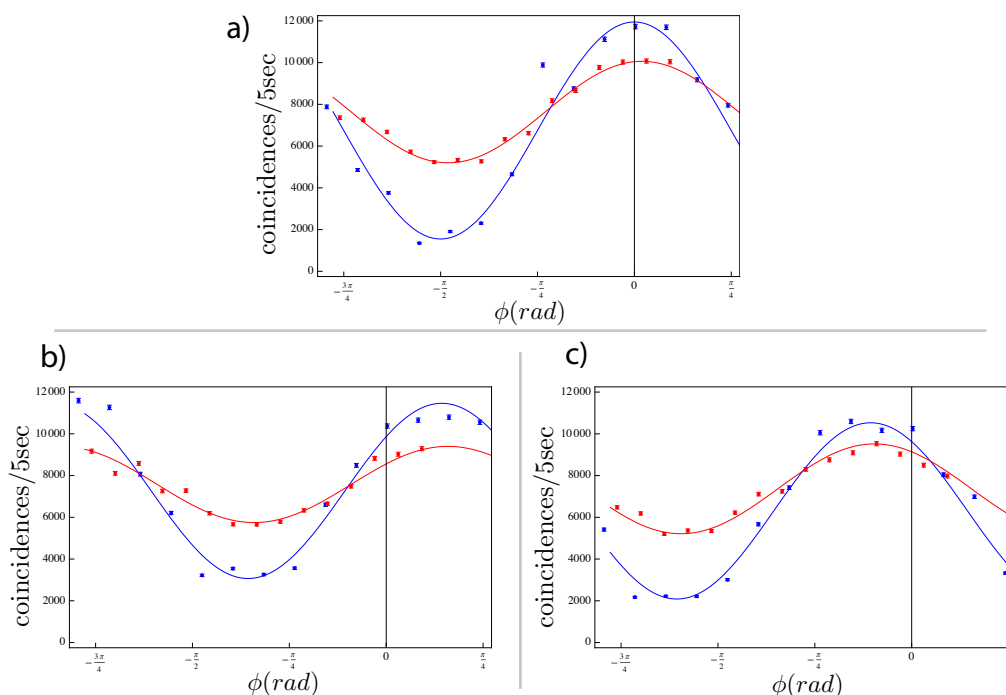
Figure 2.5: Indistinguishable-distinguishable cases comparison. Counted coincidences inside (blue dots) and outside (red dots) the Hong-Ou-Mandel dip for a) $(s, \alpha) = (0, \frac{9}{20}\pi)$, b) $(s, \alpha) = (\frac{4}{10}\frac{\pi}{2}, \frac{14}{20}\pi)$ and c) $(s, \alpha) = (\frac{3}{10}\frac{\pi}{2}, \frac{3}{20}\pi)$. Curves represent best sinusoidal fits for the corresponding data. Inside and outside the dip we obtain $N=11911$, $N_0=1616$, and $N^{\text{out}}=10000$, $N_0^{\text{out}}=5068$, respectively. Which, from Eq. (2.20), predicts an outside/inside visibility ratio of 0.43. The observed visibility ratios are 0.41, 0.42 and 0.44 for a), b) and c), respectively.

2.5.5   Source of polarization entangled photon pairs

The experimental setup for producing two-photon polarization entangled states is shown in Fig. 2.6a). Figure 2.6b) shows the reconstruction of the entangled state via quantum state tomography: It reveals a tangle [23] of $\mathbb{T}_{\text{tomo}}=0.959 \pm 0.001$, and a fidelity $\mathfrak{F}=0.988 \pm 0.001$ to the state $|\Psi^+\rangle=(|HV\rangle + |VH\rangle)/\sqrt{2}$.
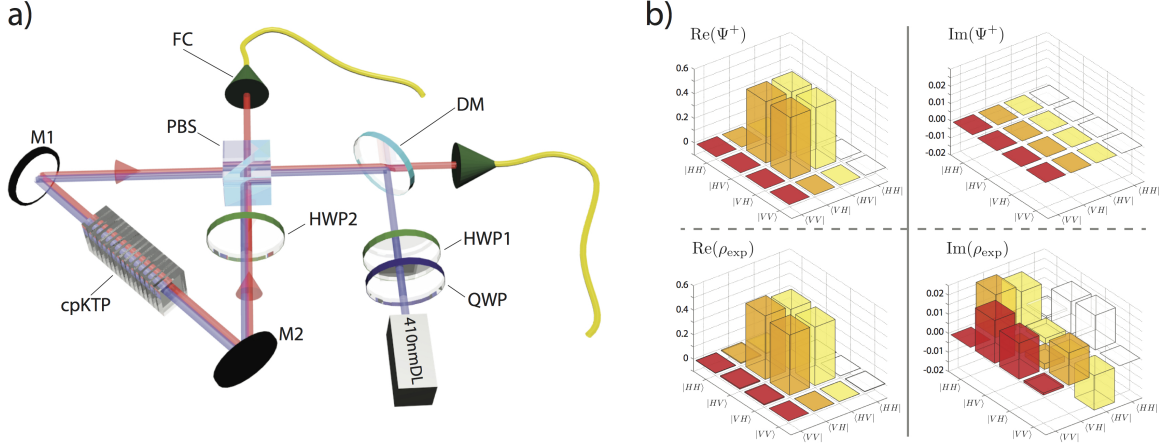
Figure 2.6: **Experimental depiction of two-photon polarization entangled source.** a) A pair of polarization entangled single-photons are produced via spontaneous parametric downconversion in a 10 mm long custom periodically-poled KTiOPO$_4$ (cpKTP) nonlinear crystal [28]. A continuous wave pump centered at 410 nm is output from a laser diode (410nmLD) with its polarization controlled by a half-wave (HWP1) and quarter-wave plate (QWP). The pump is incident on a dual-wavelength polarizing beam-splitter (PBS) [29] which together with mirrors M1 and M2 make up the Sagnac loop. The superposition of counter-propagating pump modes in the Sagnac loop destroys the 'which path' information of the downconverted fields resulting in an entangled two-photon state that can be tuned from $|HV\rangle + e^{i\phi}|VH\rangle \rightarrow |HV\rangle$ by means of the HWP1 on the pump field. HWP2 is custom made to suit both the pump at 410 nm and the downconverted light at 820 nm, it works to flip the reflected vertically polarized pump mode from $|V\rangle \rightarrow |H\rangle$ for phase matching in the cpKTP crystal. A dichroric mirror (DM) and long pass filters (not shown) before each fibre coupler (FC) separate and block the pump light from being coupled to the output FCs. b) Experimental results from a quantum state tomography of the polarization entangled two-photon state ρ_{exp}.

References

[1] Simon, B. Holonomy, the quantum adiabatic theorem, and berry's phase. *Phys. Rev. Lett.* **51**, 2167–2170 (1983).

[2] Berry, M. V. Quantal phase factors accompanying adiabatic changes. *Proc. R. Soc. Lond. A* **392**, 45–57 (1984). `http://rspa.royalsocietypublishing.org/content/392/1802/45.full.pdf+html`.

[3] Milman, P. & Mosseri, R. Topological phase for entangled two-qubit states. *Phys. Rev. Lett.* **90**, 230403 (2003).

[4] LiMing, W., Tang, Z. L. & Liao, C. J. Representation of the SO(3) group by a maximally entangled state. *Phys. Rev. A* **69**, 064301 (2004).

[5] Zanardi, P. & Rasetti, M. Holonomic quantum computation. *Physics Letters A* **264**, 94 – 99 (1999).

[6] Duan, L.-M., Cirac, J. I. & Zoller, P. Geometric manipulation of trapped ions for quantum computation. *Science* **292**, 1695–1697 (2001). `http://www.sciencemag.org/content/292/5522/1695.full.pdf`.

[7] Wu, L.-A., Zanardi, P. & Lidar, D. A. Holonomic quantum computation in decoherence-free subspaces. *Phys. Rev. Lett.* **95**, 130501 (2005).

[8] Sjöqvist, E. *et al.* Non-adiabatic holonomic quantum computation. *New Journal of Physics* **14**, 103035 (2012).

[9] Filipp, S. *et al.* Experimental demonstration of the stability of berry's phase for a spin-1/2 particle. *Phys. Rev. Lett.* **102**, 030404 (2009).

[10] Abdumalikov Jr, A. A. *et al.* Experimental realization of non-abelian non-adiabatic geometric gates. *Nature* **496**, 482–485 (2013).

[11] Feng, G., Xu, G. & Long, G. Experimental realization of nonadiabatic holonomic quantum computation. *Phys. Rev. Lett.* **110**, 190501 (2013).

[12] Kwiat, P. G. & Chiao, R. Y. Observation of a nonclassical berry's phase for the photon. *Phys. Rev. Lett.* **66**, 588–591 (1991).

[13] Ericsson, M. *et al.* Measurement of geometric phase for mixed states using single photon interferometry. *Phys. Rev. Lett.* **94**, 050401 (2005).

[14] Cucchietti, F. M., Zhang, J.-F., Lombardo, F. C., Villar, P. I. & Laflamme, R. Geometric phase with nonunitary evolution in the presence of a quantum critical bath. *Phys. Rev. Lett.* **105**, 240406 (2010).

[15] Kobayashi, H., Ikeda, Y., Tamate, S., Nakanishi, T. & Kitano, M. Nonlinear behavior of geometric phases induced by photon pairs. *Phys. Rev. A* **83**, 063808 (2011).

[16] Souza, C. E. R., Huguenin, J. A. O., Milman, P. & Khoury, A. Z. Topological phase for spin-orbit transformations on a laser beam. *Phys. Rev. Lett.* **99**, 160401 (2007).

[17] Du, J., Zhu, J., Shi, M., Peng, X. & Suter, D. Experimental observation of a topological phase in the maximally entangled state of a pair of qubits. *Phys. Rev. A* **76**, 042121 (2007).

[18] Sjöqvist, E. Geometric phase for entangled spin pairs. *Phys. Rev. A* **62**, 022109 (2000).

[19] Jakóbczyk, L. & Siennicki, M. Geometry of bloch vectors in two-qubit system. *Physics Letters A* **286**, 383–390 (2001).

[20] Mukunda, N. & Simon, R. Quantum kinematic approach to the geometric phase. i. general formalism. *Annals of Physics* **228**, 205 – 268 (1993).

[21] Pancharatnam, S. Generalized theory of interference, and its applications. *Proc. Ind. Acad. Sci. A* **44**, 247–262 (1956).

[22] Milman, P. Phase dynamics of entangled qubits. *Phys. Rev. A* **73**, 062118 (2006).

[23] Hill, S. & Wootters, W. K. Entanglement of a pair of quantum bits. *Phys. Rev. Lett.* **78**, 5022–5025 (1997).

[24] Tong, D. M., Sjöqvist, E., Kwek, L. C., Oh, C. H. & Ericsson, M. Relation between geometric phases of entangled bipartite systems and their subsystems. *Phys. Rev. A* **68**, 022106 (2003).

[25] Ericsson, M., Pati, A. K., Sjöqvist, E., Brännlund, J. & Oi, D. K. L. Mixed state geometric phases, entangled systems, and local unitary transformations. *Phys. Rev. Lett.* **91**, 090405 (2003).

[26] Johansson, M., Ericsson, M., Singh, K., Sjöqvist, E. & Williamson, M. S. Topological phases and multiqubit entanglement. *Phys. Rev. A* **85**, 032112 (2012).

[27] Loredo, J. C., Ortíz, O., Weingärtner, R. & De Zela, F. Measurement of pancharatnam's phase by robust interferometric and polarimetric methods. *Phys. Rev. A* **80**, 012113 (2009).

[28] Brańczyk, A., Fedrizzi, A., Stace, T., Ralph, T. & White, A. Engineered optical nonlinearity for quantum light sources. *Optics express* **19**, 55 (2011).

[29] Smith, D. H. *et al.* Conclusive quantum steering with superconducting transition-edge sensors. *Nat Commun* **3**, 625 (2012).

[30] Hong, C. K., Ou, Z. Y. & Mandel, L. Measurement of subpicosecond time intervals between two photons by interference. *Phys. Rev. Lett.* **59**, 2044–2046 (1987).

[31] Walborn, S. P., de Oliveira, A. N., Pádua, S. & Monken, C. H. Multimode hong-ou-mandel interference. *Phys. Rev. Lett.* **90**, 143601 (2003).

[32] Ollivier, H. & Zurek, W. H. Quantum discord: A measure of the quantumness of correlations. *Phys. Rev. Lett.* **88**, 017901 (2001).

CHAPTER 3

Measuring entanglement in a photonic Embedding Quantum Simulator

J. C. Loredo[1], M. P. Almeida[1], R. Di Candia[2], J. S. Pedernales[2], J. Casanova[3], E. Solano[2,4], A. G. White[1]

[1] Centre for Engineered Quantum Systems, Centre for Quantum Computer and Communication Technology, School of Mathematics and Physics, University of Queensland, Brisbane, Queensland 4072, Australia

[2] Department of Physical Chemistry, University of the Basque Country UPV/EHU, Apartado 644, 48080 Bilbao, Spain

[3] Institut für Theoretische Physik, Albert-Einstein-Allee 11, Universität Ulm, D-89069 Ulm, Germany

[4] Department of Physical Chemistry, University of the Basque Country UPV/EHU, Apartado 644, 48080 Bilbao, Spain

Measuring entanglement is a demanding task that usually requires full tomography of a quantum system, involving a number of observables that grows exponentially with the number of parties. Recently, it was suggested that adding a single ancillary qubit would allow for the efficient measurement of concurrence, and indeed any entanglement monotone associated to antilinear operations. Here, we report on the experimental implementation of such a device—an embedding quantum simulator—in photonics, encoding the entangling dynamics of a bipartite system into a tripartite one. We show that bipartite concurrence can be efficiently extracted from the measurement of merely two observables, instead of fifteen, without full tomographic information.

3.1 Introduction

ENTANGLEMENT is arguably the most striking feature of quantum mechanics [1], defining a threshold between the classical and quantum behavior of nature. Yet its experimental quantification in a given system remains challenging. Several measures of entanglement involve unphysical operations, such as antilinear operations, on the quantum state [2, 3], and thus its direct measurement cannot be implemented in the laboratory. As a consequence, in general, experimental measurements of entanglement have been carried out mostly via the full reconstruction of the quantum state [4]. While this technique—called quantum state tomography (QST)—has been widely used when dealing with relatively low-dimensional systems [5, 6], it is known to become rapidly intractable as the system size grows, being outside of experimental reach in systems with ~ 10 qubits [7]. This difficulty lies in having to measure an exponentially-growing number of observables, $2^{2N}-1$, to reconstruct N-qubits. Such constraint can be relaxed somewhat by using, for example, multiple copies of the same quantum state [8], prior state knowledge in noisy dynamics [9], compressed sensing methods [10], or measuring phases monotonically dependent on entanglement [11]. However, measuring entanglement in scalable systems remains a challenging task.

An efficient alternative is to embed the system dynamics into an enlarged Hilbert-space simulator, called embedding quantum simulator (EQS) [12, 13], where unphysical operations are mapped onto physical transformations on the simulator. The price to pay, comparatively small in larger systems, is the addition of only one ancillary qubit and, usually, dealing with more involved dynamics. However, measuring the entanglement of the simulated system becomes efficient, involving the measurement of a low number of observables in the EQS, in contrast to the $2^{2N}-1$ needed with full tomography.

In this Letter, we experimentally demonstrate an embedding quantum simulator, using it to efficiently measure two-qubit entanglement. Our EQS uses three polarization-encoded qubits in a circuit with two concatenated controlled-sign gates. The measurement of only 2 observables on the resulting tripartite state gives rise to the efficient measurement of bipartite concurrence, which would otherwise need 15 observables.

3.2 The Embedding protocol

We consider the simulation of two-qubit entangling dynamics governed by the Hamiltonian $H=-g\sigma_z \otimes \sigma_z$, where $\sigma_z=|0\rangle\langle0|-|1\rangle\langle1|$ is the z-Pauli matrix written in the computational basis, $\{|0\rangle, |1\rangle\}$, and g is a constant with units of frequency. For simplicity, we let $\hbar=1$. Under this Hamiltonian, the concurrence [2] of an evolving pure state $|\psi(t)\rangle$ is calculated as $\mathcal{C}=|\langle\psi(t)|\sigma_y \otimes \sigma_y K|\psi(t)\rangle|$, where K is the complex conjugate operator defined as

$$K|\psi(t)\rangle=|\psi(t)^*\rangle. \tag{3.1}$$

Notice here the explicit dependance of $\mathcal{C}$ upon the unphysical transformation K. We now consider the dynamics of the initial state $|\psi(0)\rangle = (|0\rangle + |1\rangle) \otimes (|0\rangle + |1\rangle)/2$. Under these conditions one can calculate the resulting concurrence at any time t as
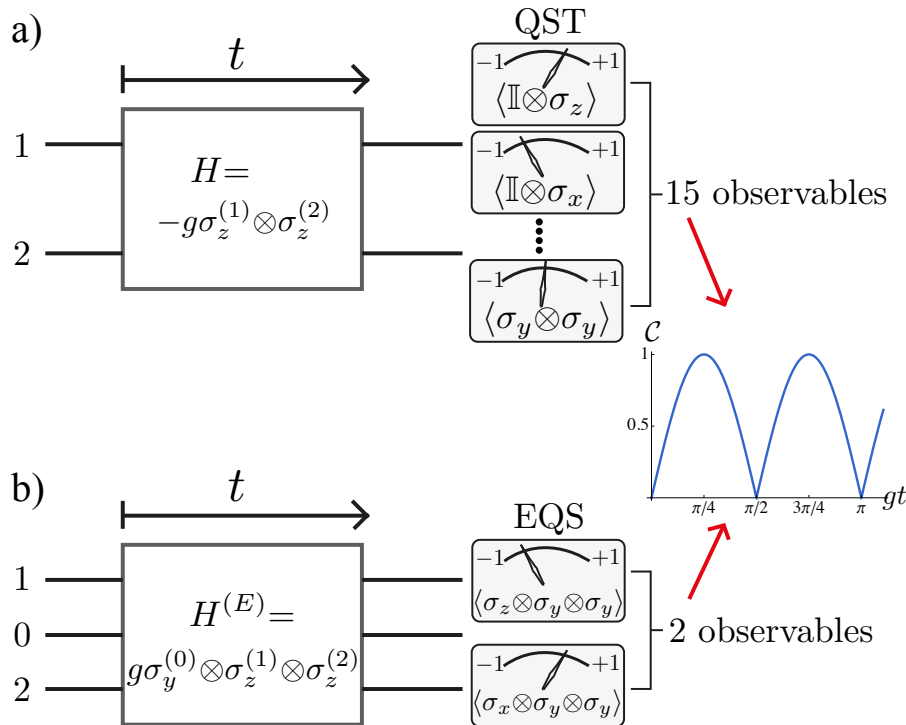
Figure 3.1: (a) Qubits 1 and 2 evolve via an entangling Hamiltonian H during a time interval t, at which point quantum state tomography (QST) is performed via the measurement of 15 observables to extract the amount of evolving concurrence. (b) An efficient alternative corresponds to adding one extra ancilla, qubit 0, and having the enlarged system—the embedding quantum simulator (EQS)—evolve via $H^{(E)}$. Only two observables are now required to reproduce measurements of concurrence of the system under simulation.

$$\mathcal{C} = |\sin(2gt)|. \tag{3.2}$$

The target evolution, $e^{-iHt}|\psi(0)\rangle$, can be embedded in a 3-qubit simulator. Given the state of interest $|\psi\rangle$, the transformation

$$|\Psi\rangle = |0\rangle \otimes \mathrm{Re}|\psi\rangle + |1\rangle \otimes \mathrm{Im}|\psi\rangle, \tag{3.3}$$

gives rise to a real-valued 3-qubit state $|\Psi\rangle$ in the corresponding embedding quantum simulator. The decoding map is, accordingly, $|\psi\rangle = \langle 0|\Psi\rangle + i\langle 1|\Psi\rangle$. The physical unitary gate $\sigma_z \otimes \mathbb{I}_4$ transforms the simulator state into $\sigma_z \otimes \mathbb{I}_4|\Psi\rangle = |0\rangle \otimes \mathrm{Re}|\psi\rangle - |1\rangle \otimes \mathrm{Im}|\psi\rangle$, which after the decoding becomes $\langle 0|\Psi\rangle - i\langle 1|\Psi\rangle = \mathrm{Re}|\psi\rangle - i\mathrm{Im}|\psi\rangle = |\psi^*\rangle$. Therefore, the action of the complex conjugate operator K corresponds to the single qubit rotation $\sigma_z \otimes \mathbb{I}_4$ [12, 14]. Now, following the same encoding rules: $\langle\psi|OK|\psi\rangle = \langle\Psi|(\sigma_z - i\sigma_x) \otimes O|\Psi\rangle$, with O an observable in the simulation. In the

case of $O=\sigma_y\otimes\sigma_y$, we obtain

$$\mathcal{C} = |\langle\sigma_z \otimes \sigma_y \otimes \sigma_y\rangle - i\langle\sigma_x \otimes \sigma_y \otimes \sigma_y\rangle|, \tag{3.4}$$

which relates the simulated concurrence to the expectation values of two nonlocal operators in the embedding quantum simulator. Regarding the dynamics, it can be shown that the Hamiltonian $H^{(E)}$ that governs the evolution in the simulator is $H^{(E)}=-\sigma_y\otimes(\text{Re}H)+i\mathbb{I}_2\otimes(\text{Im}H)$ [12]. Accordingly, in our case, it will be given by $H^{(E)}=g\sigma_y\otimes\sigma_z\otimes\sigma_z$.

Our initial state under simulation is $|\psi(0)\rangle=(|0\rangle+|1\rangle)\otimes(|0\rangle+|1\rangle)/2$, which requires, see Eq. (3.3), the initialization of the simulator in $|\Psi(0)\rangle=|0\rangle\otimes(|0\rangle+|1\rangle)\otimes(|0\rangle+|1\rangle)/2$. Under these conditions, the relevant simulator observables, see Eq. (3.4), read $\langle\sigma_x\otimes\sigma_y\otimes\sigma_y\rangle=\sin(2gt)$ and $\langle\sigma_z\otimes\sigma_y\otimes\sigma_y\rangle=0$, from which the concurrence of Eq. (3.2) will be extracted. Therefore, our recipe, depicted in Fig. 3.1, allows the encoding and efficient measurement of two-qubit concurrence dynamics.
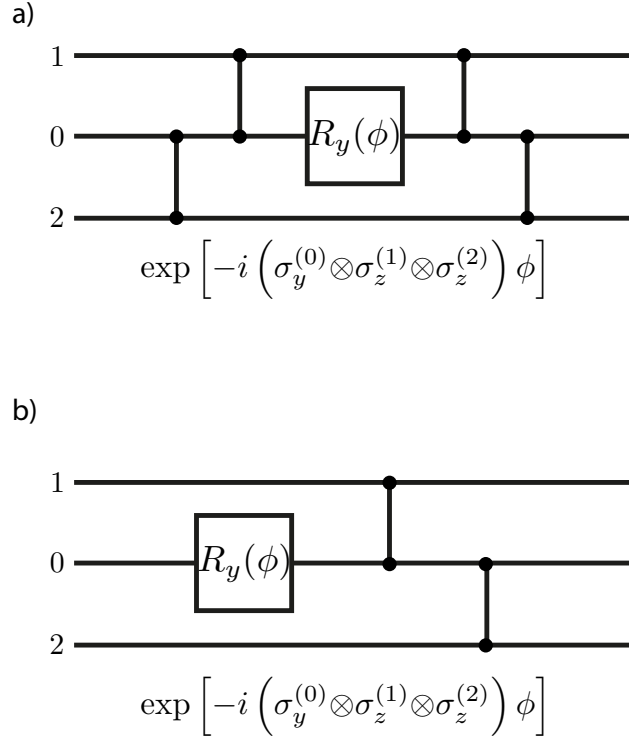
Figure 3.2: Quantum circuit for the embedding quantum simulator. (a) 4 controlled-sign gates and one local rotation $R_y(\phi)$ implement the evolution operator $U(t)=\exp\left(-ig\sigma_y^{(0)}\otimes\sigma_z^{(1)}\otimes\sigma_z^{(2)}t\right)$, with $\phi=gt$. (b) A reduced circuit employing only two controlled-sign gates reproduces the desired three-qubit dynamics for inputs with the ancillary qubit in $|0\rangle$.

To construct the described three-qubit simulator dynamics, it can be shown (see Appendix) that a quantum circuit consisting of 4 controlled-sign gates and one local rotation $R_y(\phi)=\exp(-i\sigma_y\phi)$, as depicted in Fig. 3.2(a), implements the evolution operator:

$$U(t)=\exp\left[-ig\left(\sigma_y\otimes\sigma_z\otimes\sigma_z\right)t\right], \tag{3.5}$$

reproducing the desired dynamics, with $\phi = gt$. This quantum circuit can be further reduced if we consider only inputs with the ancillary qubit in state $|0\rangle$, in which case, only two controlled-sign gates reproduce the same evolution, see Fig. 3.2 (b). This reduced subspace of initial states corresponds to simulated input states of only real components.

3.3 Experimental implementation

We encode a three-qubit state in the polarization of 3 single-photons. The logical basis is encoded according to $|h\rangle \equiv |0\rangle, |v\rangle \equiv |1\rangle$, where $|h\rangle$ and $|v\rangle$ denote horizontal and vertical polarization, respectively. The simulator is initialized in the state

$$|\Psi(0)\rangle = |h\rangle^{(0)} \otimes \left(|h\rangle^{(1)} + |v\rangle^{(1)}\right) \otimes \left(|h\rangle^{(2)} + |v\rangle^{(2)}\right)/2 \tag{3.6}$$

of qubits 0, 1 and 2, and evolves via the optical circuit in Fig. 3.2 (b).

3.3.1 The setup

Figure 3.3 is the physical implementation of Fig. 3.2 (b), where the dimensionless parameter $\phi = gt$ is controlled by the angle $\phi/2$ of one half-wave plate. The two concatenated controlled-sign gates are implemented by probabilistic gates based on two-photon quantum interference [15, 16, 17], see Appendix.

In order to reconstruct the two three-qubit observables in Eq. (3.4), one needs to collect 8 possible tripartite correlations of the observable eigenstates. For instance, the observable $\langle \sigma_x \otimes \sigma_y \otimes \sigma_y \rangle$ is obtained from measuring the 8 projection combinations of the states

$$\{|d\rangle, |a\rangle\} \otimes \{|r\rangle, |l\rangle\} \otimes \{|r\rangle, |l\rangle\},$$

where $|d\rangle = (|h\rangle + |v\rangle)/\sqrt{2}$, $|r\rangle = (|h\rangle + i|v\rangle)/\sqrt{2}$, and $|a\rangle$ and $|l\rangle$ are their orthogonal states, respectively. To implement these polarization projections, we employed Glan-Taylor prisms due to their high extinction ratio. However, only their transmission mode is available, which required each of the 8 different projection settings separately, extending our data-measuring time. The latter can be avoided by simultaneously registering both outputs of a projective measurement, such as at the two output ports of a polarizing beam splitter, allowing the simultaneous recording of all 8 possible projection settings. Thus, an immediate reconstruction of each observable is possible.

Our source of single-photons consists of four-photon events collected from the forward and backward pair emission in spontaneous parametric down-conversion in a *beta*-barium borate (BBO) crystal pumped by a 76 MHz frequency-doubled mode-locked femtosecond Ti:Sapphire laser. One of the four photons is sent directly to an avalanche photodiode detector (APD) to act as a trigger, while the other 3 photons are used in the protocol. This kind of sources are known to suffer from undesired higher-order photon events that are ultimately responsible
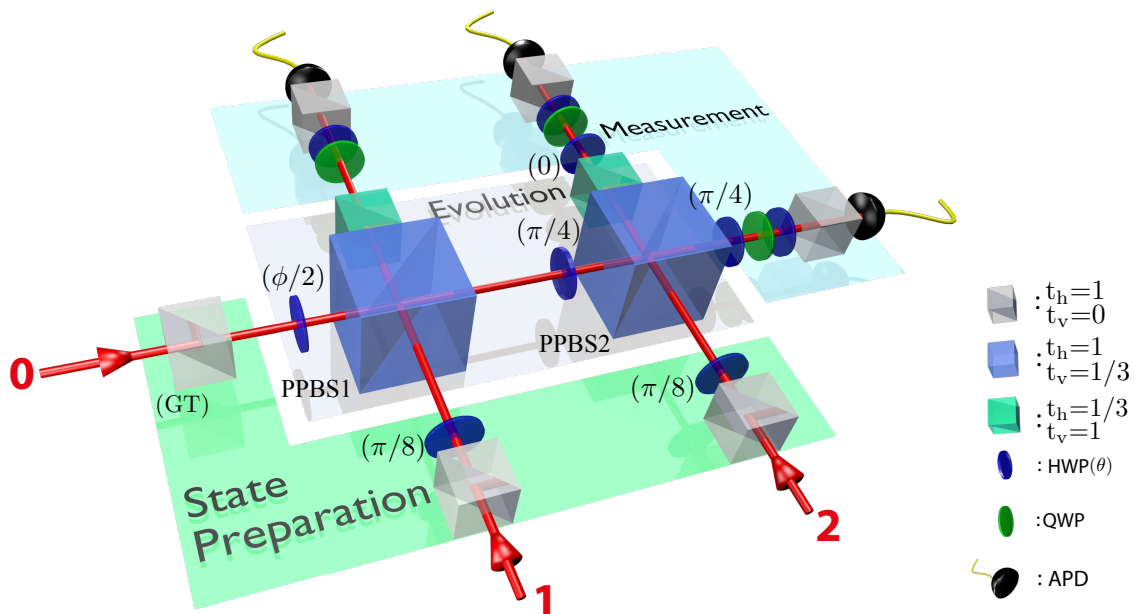
Figure 3.3: Experimental setup. Three single-photons with wavelength centered at 820 nm are injected via single-mode fibers into spatial modes 0, 1 and 2. Glan-Taylor (GT's) prisms, with transmittance $t_h=1$ ($t_v=0$) for horizontal (vertical) polarization, and half-wave plates (HWP's) are employed to initialize the state. Controlled two-qubit operations are performed based on two-photon quantum interference at partially polarizing beam-splitters (PPBS's). Projective measurements are carried out with a combination of half-wave plates, quarter-wave plates (QWP's) and Glan-Taylor prisms. The photons are collected via single-mode fibers and detected by avalanche photodiodes (APD's).

of a non-trivial gate performance degradation [19, 18, 20], although they can be reduced by decreasing the laser pump power. However, given the probabilistic nature and low efficiency of down-conversion processes, multi-photon experiments are importantly limited by low count-rates, see Appendix. Therefore, increasing the simulation performance quality by lowering the pump requires much longer integration times to accumulate meaningful statistics, which ultimately limits the number of measured experimental settings.

As a result of these higher-order noise terms, a simple model can be considered to account for non-perfect input states. The experimental input n-qubit state ρ_{exp} can be regarded as consisting of the ideal state ρ_{id} with certain probability ε, and a white-noise contribution with probability $1-\varepsilon$, i.e. $\rho_{\mathrm{exp}}=\varepsilon\rho_{\mathrm{id}}+(1-\varepsilon)\mathbb{I}_{2^n}/2^n$. Since the simulated concurrence is expressed in terms of tensorial products of Pauli matrices, the experimentally simulated concurrence becomes $\mathcal{C}_{\mathrm{exp}}=\varepsilon|\sin(2gt)|$.

3.3.2 Three-qubit protocol

In Fig. 3.4, we show our main experimental results from our photonic embedding quantum simulator for one cycle of concurrence evolution taken at different pump powers: 60 mW, 180 mW, and 600 mW—referred as to 10%, 30%, and 100% pump, respectively. Figure 3.4 (a) shows
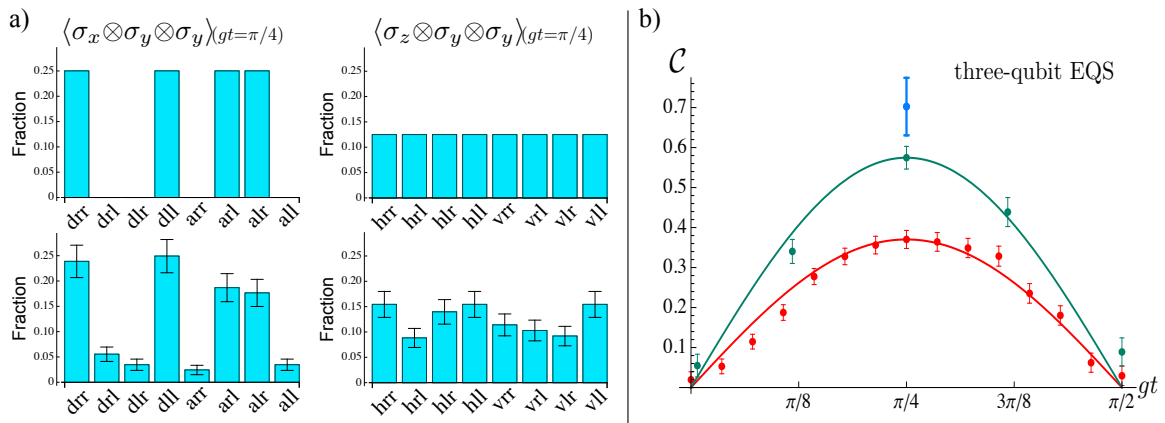
Figure 3.4: (a) Theoretical predictions (top) and experimentally measured (bottom) fractions involved in reconstructing $\langle\sigma_x\otimes\sigma_y\otimes\sigma_y\rangle$ (left) and $\langle\sigma_z\otimes\sigma_y\otimes\sigma_y\rangle$ (right), taken at $gt=\pi/4$ for a 10% pump. (b) Extracted simulated concurrence within one evolution cycle, taken at 10% (blue), 30% (green), and 100% (red) pump powers. Curves represent $\mathcal{C}=\mathcal{C}_{\mathrm{pp}}|\sin(2gt)|$, where $\mathcal{C}_{\mathrm{pp}}$ is the maximum concurrence extracted for a given pump power (pp): $\mathcal{C}_{10\%}=0.70\pm0.07$, $\mathcal{C}_{30\%}=0.57\pm0.03$ and $\mathcal{C}_{100\%}=0.37\pm0.02$. Errors are estimated from propagated Poissonian statistics. The low count-rates of the protocol, see Appendix, limit the number of measured experimental settings, hence only one data point could be reconstructed at 10% pump.

theoretical predictions (for ideal pure-state inputs) and measured fractions of the different projections involved in reconstructing $\langle\sigma_x\otimes\sigma_y\otimes\sigma_y\rangle$ and $\langle\sigma_z\otimes\sigma_y\otimes\sigma_y\rangle$ for 10% pump at $gt=\pi/4$. From measuring these two observables, see Eq. (3.4), we construct the simulated concurrence produced by our EQS, shown in Fig. 3.4 (b). We observe a good behavior of the simulated concurrence, which preserves the theoretically predicted sinusoidal form. The overall attenuation of the curve is in agreement with the proposed model of imperfect initial states. Together with the unwanted higher-order terms, we attribute the observed degradation to remaining spectral mismatch between photons created by independent down-conversion events and injected to inputs 0 and 2 of Fig. 3.3—at which outputs 2 nm band-pass filters with similar but not identical spectra were used.

3.3.3 Two-qubit protocol

We compare our measurement of concurrence via our simulator with an explicit measurement from state tomography. In the latter we inject one down-converted pair into modes 0 and 1 of Fig. 3.3. For any value of t, set by the wave-plate angle ϕ, this evolving state has the same amount of concurrence as the one from our simulation, they are equivalent in the sense that one is related to the other at most by local unitaries, which could be seen as incorporated in either the state preparation or within the tomography settings.

Figure 3.5 shows our experimental results for the described two-photon protocol. We extracted the concurrence of the evolving two-qubit state from overcomplete measurements in quantum state tomography [4]. A maximum concurrence value of $\mathcal{C}=1$ is predicted in the ideal
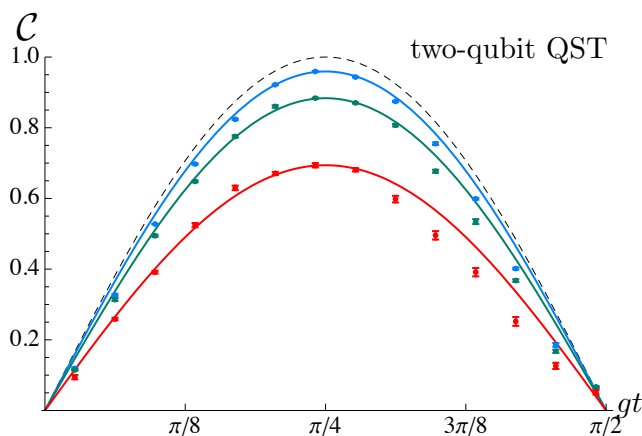
Figure 3.5: Concurrence measured via two-qubit quantum state tomography (QST) on the explicit two-photon evolution, taken at 10% (blue), 30% (green), and 100% (red) pump powers. The corresponding curves indicate $\mathcal{C}=\mathcal{C}_{\mathrm{pp}}|\sin(2gt)|$, with $\mathcal{C}_{\mathrm{pp}}$ the maximum extracted concurrence for a given pump power (pp): $\mathcal{C}_{10\%}=0.959 \pm 0.002$, $\mathcal{C}_{30\%}=0.884 \pm 0.002$, and $\mathcal{C}_{100\%}=0.694\pm0.006$. Errors are estimated from Monte-Carlo simulations of Poissonian counting fluctuations.

case of perfect pure-state inputs. Experimentally, we measured maximum values of concurrence of $\mathcal{C}_{10\%}=0.959\pm0.002$, $\mathcal{C}_{30\%}=0.884\pm0.002$ and $\mathcal{C}_{100\%}=0.694\pm0.006$, for the three different pump powers, respectively. For the purpose of comparing this two-photon protocol with our embedding quantum simulator, only results for the above mentioned powers are shown. However, we performed an additional two-photon protocol run at an even lower pump power of 30 mW (5% pump), and extracted a maximum concurrence of $\mathcal{C}_{5\%}=0.979 \pm 0.001$. A clear and pronounced decline on the extracted concurrence at higher powers is also observed in this protocol. However, a condition closer to the ideal one is reached. This observed pump power behavior and the high amount of measured concurrence suggest a high-quality gate performance, and that higher-order terms—larger for higher pump powers—are indeed the main cause of performance degradation.

While only mixed states are always involved in experiments, different degrees of mixtures are present in the 3- and 2-qubit protocols, resulting in different extracted concurrence from both methods. An inspection of the pump-dependence, see Appendix, reveals that both methods decrease similarly with pump power and are close to performance saturation at the 10% pump level. This indicates that in the limit of low higher-order emission our 3-qubit simulator is bounded to the observed performance. Temporal overlap between the 3 photons was carefully matched. Therefore, we attribute the remaining discrepancy to spectral mismatch between photons originated from independent down-conversion events. This disagreement can in principle be reduced via error correction [21, 22] and entanglement purification [23] schemes with linear optics.

3.4   Discussion

We have shown experimentally that entanglement measurements in a quantum system can be efficiently done in a higher-dimensional embedding quantum simulator. The manipulation of larger Hilbert spaces for simplifying the processing of quantum information has been previously considered [24]. However, in the present scenario, this advantage in computing concurrence originates from higher-order quantum correlations, as it is the case of the appearance of tripartite entanglement [25, 26].

The efficient behavior of embedding quantum simulators resides in reducing an exponentially-growing number of observables to only a handful of them for the extraction of entanglement monotones. We note that in this non-scalable photonic platform the addition of one ancillary qubit and one entangling gate results in count rates orders of magnitude lower as compared to direct state tomography on the 2-qubit dynamics. This means that in practice absolute integration times favor the direct 2-qubit implementation. However, this introduced limitation escapes from the purposes of the embedding protocol and instead belongs to the specific technology employed in its current state-of-the-art performance.

This work represents the first proof-of-principle experiment showing the efficient behavior of embedding quantum simulators for the processing of quantum information and extraction of entanglement monotones. This validates an architecture-independent paradigm that, when implemented in a scalable platform, e.g. ions [7, 13], would overcome a major obstacle in the characterization of large quantum systems. The relevance of these techniques will thus become patent as quantum simulators grow in size and currently standard approaches like full tomography become utterly unfeasible. We believe that these results pave the way to the efficient measurement of entanglement in any quantum platform via embedding quantum simulators.

3.5 Appendix

3.5.1 Quantum circuit of the embedding quantum simulator

Following the main text, the evolution operator associated with the embedding Hamiltonian $H^{(E)} = g\sigma_y \otimes \sigma_z \otimes \sigma_z$ can be implemented via 4 control-Z gates (CZ), and a single qubit rotation $R_y(t)$. These gates act as

$$
\begin{align}
CZ^{ij} &= |0\rangle\langle 0|^{(i)} \otimes \mathbb{I}^{(j)} + |1\rangle\langle 1|^{(i)} \otimes \sigma_z^{(j)}, \tag{3.7}\\
R_y^i(t) &= e^{-i\sigma_y^{(i)}gt} \equiv (\cos(gt)\mathbb{I}^{(i)} - i\sin(gt)\sigma_y^{(i)}), \tag{3.8}
\end{align}
$$

with $\sigma_z = |0\rangle\langle 0| - |1\rangle\langle 1|$, and $\sigma_y = -i|0\rangle\langle 1| + i|1\rangle\langle 0|$. The indices i and j indicate on which particle the operators act. The circuit for the embedding quantum simulator consists of a sequence of gates applied in the following order:

$$
U(t) = CZ^{02}CZ^{01}R_y^0(t)CZ^{01}CZ^{02}. \tag{3.9}
$$

Simple algebra shows that this expression can be recast as

$$
\begin{align}
U(t) &= \cos(gt)\mathbb{I}^{(0)} \otimes \mathbb{I}^{(1)} \otimes \mathbb{I}^{(2)} - i\sin(gt)\sigma_y^{(0)} \otimes \sigma_z^{(1)} \otimes \sigma_z^{(2)}\\
&= \exp\left(-ig\sigma_y^{(0)} \otimes \sigma_z^{(1)} \otimes \sigma_z^{(2)}t\right), \tag{3.10}
\end{align}
$$

explicitly exhibiting the equivalence between the gate sequence and the evolution under the Hamiltonian of interest.

3.5.2 Linear optics implementation

The evolution of the reduced circuit is given by a $R_y(t)$ rotation of qubit 0, followed by two consecutive control-Z gates on qubits 1 and 2, both controlled on qubit 0, see Fig. 3.6 (a). These logic operations are experimentally implemented by devices that change the polarization of the photons, where the qubits are encoded, with transformations as depicted in Fig. 3.6 (b). For single qubit rotations, we make use of half-wave plates (HWP's), which shift the linear polarization of photons. For the two-qubit gates, we make use of two kinds of partially-polarizing beam splitters (PPBS's). PPBS's of type 1 have transmittances $t_h=1$ and $t_v=1/3$ for horizontal and vertical polarizations, respectively. PPBS's of type 2, on the other hand, have transmittances $t_h=1/3$ and $t_v=1$. Their effect can be expressed in terms of polarization dependant input-output relations—with the transmitted mode corresponding to the output mode—of the bosonic creation operators as

$$
\begin{align}
a_{p,out}^{\dagger(i)} &= \sqrt{t_p}a_{p,in}^{\dagger(i)} + \sqrt{1-t_p}a_{p,in}^{\dagger(j)} \tag{3.11}\\
a_{p,out}^{\dagger(j)} &= \sqrt{1-t_p}a_{p,in}^{\dagger(i)} - \sqrt{t_p}a_{p,in}^{\dagger(j)}, \tag{3.12}
\end{align}
$$

where $a_{p,in}^{\dagger(i)}$ ($a_{p,out}^{\dagger(i)}$) stands for the i-th input (output) port of a PPBS with transmittance t_p for p-polarized photons.
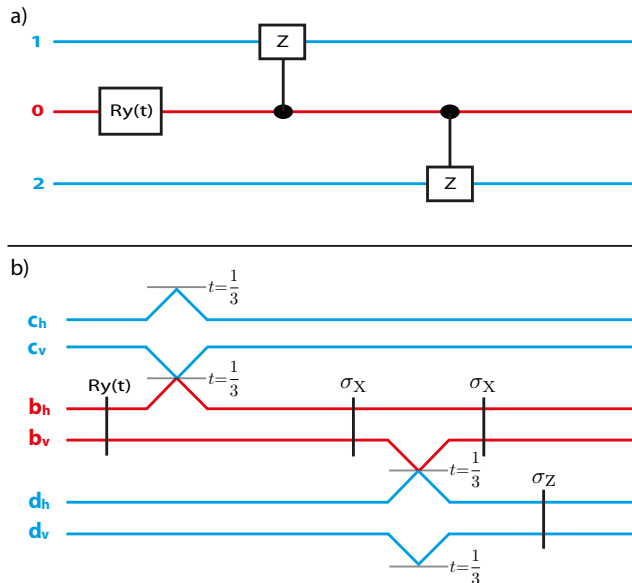
Figure 3.6: (a) Circuit implementing the evolution operator $U(t)=\exp\left(-ig\sigma_y^{(0)}\otimes\sigma_z^{(1)}\otimes\sigma_z^{(2)}t\right)$, if the initial state is $|\Psi(0)\rangle=|0\rangle^{(0)}\otimes\left(|0\rangle^{(1)}+|1\rangle^{(1)}\right)\otimes\left(|0\rangle^{(2)}+|1\rangle^{(2)}\right)/2$. (b) Dual-rail representation of the circuit implemented with linear-optics. Red (blue) lines represent trajectories undertaken by the control qubit (target qubits).

Our circuit is implemented as follows: the first $R_y(t)$ rotation is implemented via a HWP oriented at an angle $\theta = gt/2$ with respect to its optical axis. The rest of the target circuit, corresponding to the sequence of two control-Z gates, can be expressed in terms of the transformation of the input to output creation operators as

$$
\begin{aligned}
b_h c_h d_h &\rightarrow b_h c_h d_h \\
b_h c_h d_v &\rightarrow b_h c_h d_v \\
b_h c_v d_h &\rightarrow b_h c_v d_h \\
b_h c_v d_v &\rightarrow b_h c_v d_v \\
b_v c_h d_h &\rightarrow b_v c_h d_h \\
b_v c_h d_v &\rightarrow -b_v c_h d_v \\
b_v c_v d_h &\rightarrow -b_v c_v d_h \\
b_v c_v d_v &\rightarrow b_v c_v d_v,
\end{aligned}
\tag{3.13}
$$

where $b\equiv a^{\dagger(0)}$, $c\equiv a^{\dagger(1)}$, and $d\equiv a^{\dagger(2)}$ denote the creation operators acting on qubits 0, 1, and 2, respectively. These polarization transformations can be implemented with a probability of $1/27$ via a 3-fold coincidence detection in the circuit depicted in Fig. 3.6 (b). In this dual-rail representation of the circuit, interactions of modes c and d with vacuum modes are left implicit.

The σ_x and σ_z single qubit gates in Fig. 3.6 (b) are implemented by HWP's with angles $\pi/4$

and 0, respectively. In terms of bosonic operators, these gates imply the following transformations,

$$\sigma_x: \quad b_h \to b_v, \quad b_v \to b_h \tag{3.14}$$

$$\sigma_z: \quad d_h \to d_h, \quad d_v \to -d_v. \tag{3.15}$$

According to all the input-output relations involved, it can be calculated that the optical elements in Fig. 3.6 (b) implement the following transformations

$$
\begin{aligned}
b_h c_h d_h &\to b_h c_h d_h/(3\sqrt{3}) \\
b_h c_h d_v &\to b_h c_h d_v/(3\sqrt{3}) \\
b_h c_v d_h &\to b_h c_v d_h/(3\sqrt{3}) \\
b_h c_v d_v &\to b_h c_v d_v/(3\sqrt{3}) \\
b_v c_h d_h &\to b_v c_h d_h/(3\sqrt{3}) \\
b_v c_h d_v &\to -b_v c_h d_v/(3\sqrt{3}) \\
b_v c_v d_h &\to -b_v c_v d_h/(3\sqrt{3}) \\
b_v c_v d_v &\to b_v c_v d_v/(3\sqrt{3}),
\end{aligned}
\tag{3.16}
$$

if events with 0 photons in some of the three output lines of the circuit are discarded. Thus, this linear optics implementation corresponds to the evolution of interest with success probability $P = (1/(3\sqrt{3}))^2 = 1/27$.

3.5.3 Photon count-rates

Given the probabilistic nature and low efficiency of down-conversion processes, multi-photon experiments are importantly limited by low count-rates. In our case, typical two-photon rates from source are around 150 kHz at 100% pump (two-photon rates are approx. linear with pump power), which after setup transmission ($\sim$80%) and 1/9 success probability of one controlled-sign gate, are reduced to about 13 kHz (1 kHz) at 100% (10%) pump. These count-rates make it possible to run the two-photon protocol, described in the main text, at low powers in a reasonable amount of time. However, this situation is drastically different in the three-photon protocol, where we start with 500 Hz of 4-fold events from the source, in which case after setup transmission, 1/27 success probability of two gates, and 50% transmission in each of two 2 nm filters used for this case, we are left with as few as $\sim$100 mHz ($\sim$1 mHz) at 100% (10%) pump (4-fold events reduce quadratically with pump). Consequently, long integration times are needed to accumulate meaningful statistics, imposing a limit in the number of measured experimental settings.

3.5.4   Pump-dependence

To estimate the effect of power-dependent higher-order terms in the performance of our protocols, we inspect the pump power dependence of extracted concurrence from both methods. Fig. 3.7 shows that the performances of both protocols decrease at roughly the same rate with increasing pump power, indicating that in both methods the extracted concurrence at 10% pump is close to performance saturation.
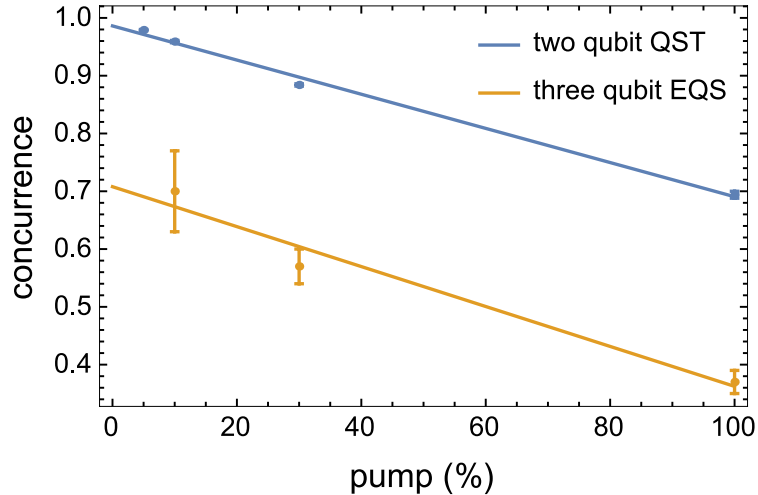
Figure 3.7: Measured concurrence vs pump power. The concurrence is extracted from both two-qubit quantum state tomography (QST) and the three-qubit embedding quantum simulator (EQS). Straight lines are linear fits to the data. Slopes overlapping within error, namely -0.0030 ± 0.0001 from QST and -0.0035 ± 0.0007 from EQS, show that both methods are affected by higher-order terms at the same rate.
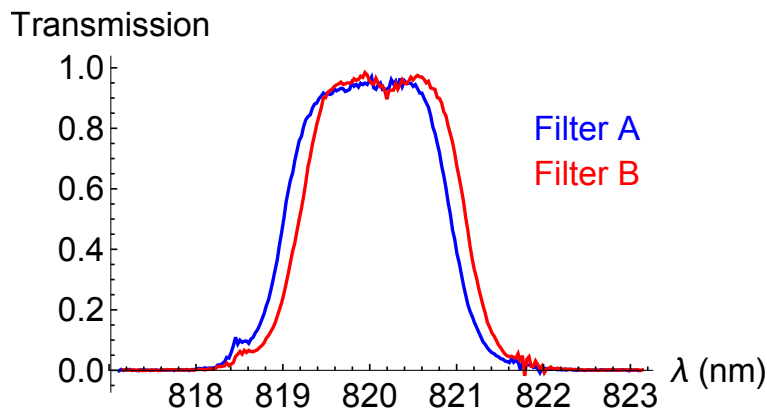
Figure 3.8: Spectral filtering. The measured transmission for both filters used in our three-qubit protocol qualitatively reveals the remaining spectral mismatch.

The principal difference between the two methods is that in the three-qubit protocol one of the photons originates from an independent down-conversion event and as such will present a slightly different spectral shape due to a difficulty in optimizing the phase-matching condition

for both forward and backward directions simultaneously. To reduce this spectral mismatch, we used two 2 nm filters at the output of the two spatial modes where interference from independent events occurs, see Fig. 3.8. Note that not identical spectra are observed. This limitation would be avoided with a source that presented simultaneous high indistinguishability between all interfering photons.

References

[1] R. Horodecki, P. Horodecki, M. Horodecki, and K. Horodecki, Rev. Mod. Phys. **81**, 865 (2009).

[2] W. K. Wootters, Phys. Rev. Lett. **80**, 2245 (1998).

[3] A. Osterloh & J. Siewert, Phys. Rev. A **72**, 012337 (2005).

[4] D. F. V. James, P. G. Kwiat, W. J. Munro, and A. G. White, Phys. Rev. A **64**, 052312 (2001).

[5] H. Häffner, W. Hänsel, C. F. Roos, J. Benhelm, D. Chek-al-kar, M. Chwalla, T. Körber, U. D. Rapol, M. Riebe, P. O. Schmidt, C. Becher, O. Gühne, W. Dür, and R. Blatt, Nature **438**, 643 (2005).

[6] X.-C. Yao, T.-X. Wang, P. Xu, L. He, G.-S. Pan, X.-H. Bao, C.-Z. Peng, C.-Y. Lu, Y.-A. Chen and J.-W. Pan, Nat. Photon **6**, 225 (2012).

[7] T. Monz, P. Schindler, J. T. Barreiro, M. Chwalla, D. Nigg, W. A. Coish, M. Harlander, W. Hansel, M. Hennrich, and R. Blatt, Phys. Rev. Lett. **106**, 130506 (2011).

[8] S. P. Walborn, P. H. Souto Ribeiro, L. Davidovich, F. Mintert, and A. Buchleitner, Nature **440**, 1022 (2006).

[9] O. Jiménez Farías, C. Lombard Latune, S. P. Walborn, L. Davidovich, and P. H. Souto Ribeiro, Science **324**, 1414 (2009).

[10] D. Gross, Y.-K. Liu, S. T. Flammia, S. Becker, and J. Eisert, Phys. Rev. Lett. **105**, 150401 (2010).

[11] J. C. Loredo, M. A. Broome, D. H. Smith, and A. G. White, Phys. Rev. Lett. **112**, 143603 (2014).

[12] R. Di Candia, B. Mejia, H. Castillo, J. S. Pedernales, J. Casanova, and E. Solano, Phys. Rev. Lett. **111**, 240502 (2013).

[13] J. S. Pedernales, R. Di Candia, P. Schindler, T. Monz, M. Hennrich, J. Casanova, and E. Solano, Phys. Rev. A **90**, 012327 (2014).

[14] J. Casanova, C. Sabín, J. León, I. L. Egusquiza, R. Gerritsma, C. F. Roos, J. J. García-Ripoll, and E. Solano, Phys. Rev. X **1**, 021018 (2011).

[15] T. C. Ralph, A. G. White, W. J. Munro, and G. J. Milburn, Phys. Rev. A **65**, 012314 (2001).

[16] J. L. O'Brien, G. J. Pryde, A. G. White, T. C. Ralph, and D. Branning, Nature **426**, 264 (2003).

[17] T. C. Ralph, Phys. Rev. A **70**, 012312 (2004).

[18] T. J. Weinhold, A. Gilchrist, K. J. Resch, A. C. Doherty, J. L. O'Brien, G. J. Pryde, and A. G. White, arXiv:0808.0794 (2008).

[19] M. Barbieri, T. Weinhold, B. Lanyon, A. Gilchrist, K. Resch, M. Almeida, and A. White, Journal of Modern Optics **56**, 209 (2009).

[20] J.-W. Pan, Z.-B. Chen, C.-Y. Lu, H. Weinfurter, A. Zeilinger, and M. Zukowski, Rev. Mod. Phys. **84**, 777 (2012).

[21] J. L. O'brien, G. J. Pryde, A. G. White, and T. C. Ralph, Phys. Rev. A **71**, 060303 (2005).

[22] X.-C. Yao, T.-X. Wang, H.-Z. Chen, W.-B. Gao, A. G. Fowler, R. Raussendorf, Z.-B. Chen, N.-L. Liu, C.-Y. Lu, Y.-J. Deng, Y.-A. Chen, and J.-W. Pan, Nature **482**, 489 (2012).

[23] J.-W. Pan, S. Gasparoni, R. Ursin, G. Weihs, and A. Zeilinger, Nature **423**, 417 (2003).

[24] B. P. Lanyon, M. Barbieri, M. P. Almeida, T. Jennewein, T. C. Ralph, K. J. Resch, G. J. Pryde, J. L. O'Brien, A. Gilchrist, and A. G. White, Nat Phys **5**, 134 (2009).

[25] C.-Y. Lu, D. E. Browne, T. Yang, and J.-W. Pan, Phys. Rev. Lett. **99**, 250504 (2007).

[26] B. P. Lanyon, T. J. Weinhold, N. K. Langford, M. Barbieri, D. F. V. James, A. Gilchrist, and A. G. White, Phys. Rev. Lett. **99**, 250505 (2007).

Part II

Multi-Photon Experiments with Solid-State Emitters

CHAPTER 4

Scalable performance in solid-state single-photon sources

J. C. Loredo[1], N. A. Zakaria[1], N. Somaschi[2], C. Anton[2], L. De Santis[2,3], V. Giesz[2], T. Grange[4], M. A. Broome[1,†], O. Gazzano[2,‡], G. Coppola[2], I. Sagnes[2], A. Lemaitre[2], A. Auffeves[4], P. Senellart[2,5], M. P. Almeida[1], A. G. White[1]

[1]Department of Physics, Centre for Engineered Quantum Systems and Centre for Quantum Computation and Communication Technology, University of Queensland, Brisbane, Australia

[2]CNRS-LPN Laboratoire de Photonique et de Nanostructures, Université Paris-Saclay, Route de Nozay, 91460 Marcoussis, France

[3]Université Paris-Sud, Université Paris-Saclay, F-91405 Orsay, France

[4]Université Grenoble-Alpes, CNRS, Institut Néel, "Nanophysique et semiconducteurs" group, F-38000 Grenoble, France

[5]Département de Physique, Ecole Polytechnique, Université Paris-Saclay, F-91128 Palaiseau, France

[†]Present address: Centre of Excellence for Quantum Computation and Communication Technology, School of Physics, University of New South Wales, Sydney, New South Wales 2052, Australia

[‡]Present address: Joint Quantum Institute, National Institute of Standards and Technology, University of Maryland, Gaithersburg, MD, USA

The desiderata for an ideal photon source are high brightness, high single-photon purity, and high indistinguishability. Defining brightness at the first collection lens, these properties have been simultaneously demonstrated with solid-state sources, however absolute source efficiencies remain close to the 1% level, and indistinguishability only demonstrated for photons emitted consecutively on the few nanosecond scale. Here we employ deterministic quantum dot-micropillar devices to demonstrate solid-state single-photon sources with scalable performance. In one device, an absolute brightness at the output of a single-mode fibre of 14% and purities of 97.1–99.0% are demonstrated. When non-resonantly excited, it emits a long stream of photons that exhibit indistinguishability up to 70%—above the classical limit of 50%—even after 33 consecutively emitted photons, a 400 ns separation between them. Resonant excitation in other devices results in near-optimal indistinguishability values: 96% at short timescales, remaining at 88% in timescales as large as 463 ns, after 39 emitted photons. The performance attained by our devices brings solid-state sources into a regime suitable for scalable implementations.

4.1 Introduction

Photon indistinguishability—responsible for unique quantum phenomena with no classical counterpart, notably photon bunching via interference [1]—has been demonstrated in various physical systems [2, 3, 4, 5, 6, 7, 8, 9], resulting in a broad range of applications in photonic quantum technologies [10], including quantum teleportation [11, 12], generation of entangled photon sources [13, 14, 15], and linear-optics quantum computation [16, 17]. However, achieving conclusive indistinguishability, i..e. above 50% (the classical limit), while simultaneously displaying high single-photon purity and high absolute brightness is experimentally challenging.

Semiconductor quantum dots (QDs) inserted in photonic structures [18, 19, 20, 21, 22] are a rapidly improving technology for generating bright sources of indistinguishable single-photons. Addressing the excited states of the quantum dot using a non-resonant scheme early showed two-photon interference visibilities in the 70%−80% range [8], yet with limited collection efficiencies. Improvements in the efficiency have been made by deterministically placing the quantum dot in the centre of a photonic micro-cavity. Here the acceleration of photon emission into well defined cavity modes [23], due to Purcell enhancement, has enabled two-photon interference visibilities in the same range, with simultaneous efficiencies at the first collection lens around 80% [9]. Near-unity indistinguishability, in turn, has been achieved in recent years under strictly-resonant excitation of the quantum dot [24, 25, 26], whereas the recent development of electric control on deterministically coupled devices [27]—thus with scalable fabrication—has now enabled strictly-resonant excitation in combination with Purcell enhancement, resulting in near-optimal single-photon sources [28] with visibilities reaching the 99% mark, simultaneous state-of-the-art extraction efficiency of 65% and polarised brightness at the first lens around 16%.

Although impressive, the reported efficiencies in these demonstrations are defined at the first lens, and poor optical collection results in low photon count rates available in practice. Consequently, absolute brightnesses remain around the 1% mark, too low for practical scalable applications [10]. In addition, direct measurements of indistinguishability via two-photon interference, so far, only employed photons consecutively emitted with a few nanosecond separation, while a key question regarding the scalable potential of the developed sources is to determine how many consecutive photons exhibit high indistinguishability. A recent work obtained on quantum dots in microlenses reported a 40 % drop in the indistinguishability over 10 ns only [29].

In the present work, we demonstrate high absolute brightness and generation of indistinguishable photons consecutively emitted over 463 ns. Our measurements were performed on various quantum dot-micropillar devices, all obtained using a deterministic—thus scalable— technology. Using a simple micropillar (*Device* 1) [9], we demonstrate a high-purity single-photon source with an absolute brightness of 14%. That is, about one in seven laser pulses creates a high-purity single-photon at the output of a single-mode fibre. We also demonstrate robust and conclusive quantum interference between consecutively emitted photon pulses up

to a first and thirty-third, separated by 400 ns. Interference visibilities, under non-resonant excitation, reach maximum values of 70% in short timescales, decreasing to plateaus above 60% at longer temporal separations, and remain above the classical limit of 50% even at high pump-powers. Using electrically controlled pillar devices [28] (*Devices* 2 and 3) we demonstrate, under strictly resonant-excitation, indistinguishability reaching near-optimal values: 96% at short timescales, remaining above 88% at 463 ns separation.

4.2   Absolute brightness

Device 1 contains self-assembled InGaAs QDs grown by molecular beam epitaxy, positioned in between two layers of GaAs/AlAs distributed Bragg reflectors, consisting of 16 (36) pairs acting as a top (bottom) mirror. Note that *Device* 1 is a pillar from the same batch as in Ref. [9]. Low-temperature *in situ* lithography [30] was employed to fabricate micropillars centred around a single QD with 50 nm accuracy. The sample is mounted on a closed-cycle cryostat and is optically pumped by 5 ps laser pulses at 80 MHz repetition rate with wavelength tuned to 905.3 nm, corresponding to one of the quantum dot excited states in its p-shell. We optimised our collection efficiency by judicious choice of optical elements, achieving an efficiency budget as follows. After emission from the micropillar, single-photons travel across the following elements, with measured transmittances η_{elem}, before reaching detectors: two cryostat windows with η_{cryo}=(96 ± 1)%; a microscope objective (Olympus LMPLN10XIR) with N.A.=0.3 and η_{obj}=(91 ± 1)%; a dichroic mirror (Alluxa filters) used to separate single-photons from the laser path, with a measured attenuation at 905 nm bounded to > 60 dB extinction, while no appreciable loss is recorded at wavelengths corresponding to single-photon emission, we thus consider η_{dich}=1; 6 mirrors and 2 lenses, with an overall transmission of η_{ml}=(95 ± 1)%; and a 0.85 nm FWHM band-pass filter (Alluxa filters) with η_{bp}=(91 ± 1)% used to ensure that any residual scattered laser light is filtered out. Remaining losses are due to coupling to a single-mode fibre, where we estimate a fibre-coupling efficiency of η_{fc}=(65 ± 4)%, by comparing collection with a multimode fibre assumed to have a unity coupling efficiency. This results in an overall transmission of our optical setup of η_{setup}=(49 ± 3)%.

We characterise this device in terms of absolute brightness and purity, see Fig. 4.1. We detect large count-rates in a silicon avalanche photodiode (APD), as shown in the saturation measurements in Fig. 4.1a. The saturation curves are fitted to $R_0\left(1 - \exp\left(-P/P_0\right)\right)$, where R_0 is an asymptotic rate value, and P_0 is the saturation power. The inset figure shows *Device 1* spectra with varying temperature T. The energy of the QD transition varies like the band gap of the semiconductor with temperature [31], whereas the cavity mode energy follows the temperature variation of the refractive index. Adjusting the temperature thus allows tuning the QD-cavity resonance. For the measurements presented in Fig. 4.1, the neutral exciton line is brought in resonance at T=15 K. The count-rates in pulsed configuration reach values as high as 3.6 MHz. In fact, for this measurement a known loss must be introduced in the optical path in order to properly quantify the available count-rates, as they are beyond the APD's
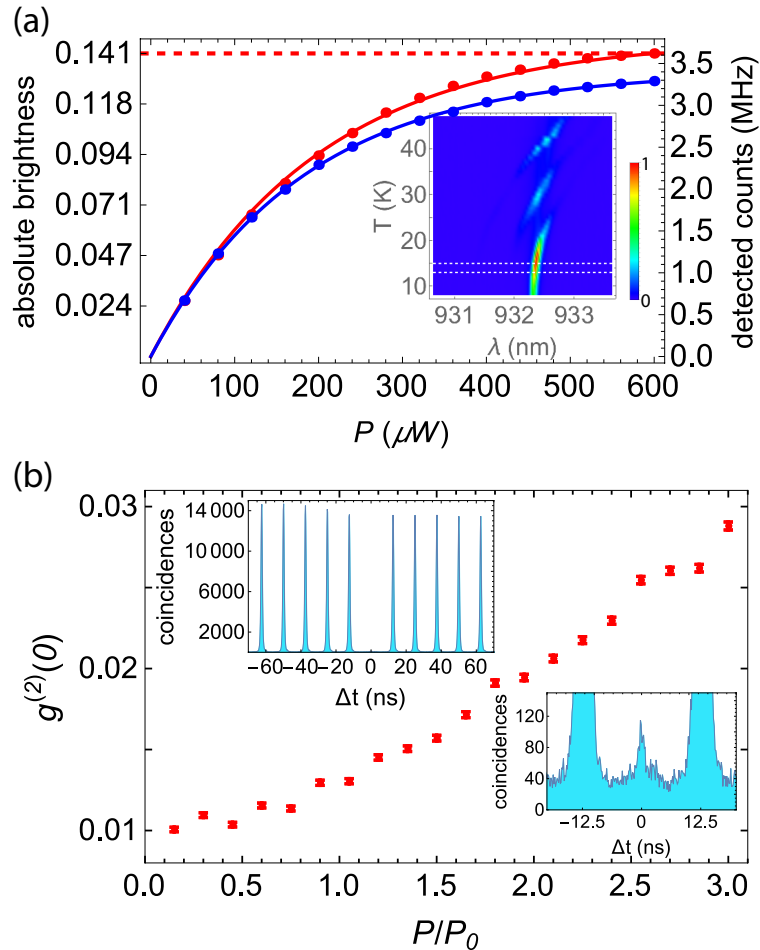
Figure 4.1: Absolute brightness and purity of *Device* 1. a) Detected count rates at T=15 K (red), with the QD in resonance with the cavity mode, and 13 K (blue), with the QD slightly detuned from the cavity. Solid curves represent fits to $R_0 \left(1 - \exp\left(-P/P_0\right)\right)$, with P_0=197 μW, and R_0=3.8 MHz for T=15 K, and R_0=3.4 MHz for T=13 K. Inset: QD spectra with varying temperature. b) Power-dependent $g^{(2)}(0)$ at T=15 K. Note that even three times above the saturation pump power the photon purity remians > 97%. Top inset shows the autocorrelation measurement for P=1P_0, and bottom inset zooms into the zero delay resolving the non-zero $g^{(2)}(0)$ from experimental noise.

(Perkin-Elmer SPCM-AQR-14-FC) linear regime. This allows us to accumulate a high amount of statistics with notably short integration times. For instance, the inset in Fig. 4.1b shows a $g^{(2)}(\Delta t)$ measurement—second-order autocorrelation function with $g^{(2)}(0)$=0 corresponding to an ideal single-photon state—at P=P_0, yielding a value of $g^{(2)}(0)$=0.0130 $\pm$ 0.0002, where the small error is reached with an integration time of only 29 seconds. We in fact used about half the available counts after selecting one linear polarisation emitted by our device. Thus, in our setup, the same amount of statistics is achieved four times faster when the polariser is removed. Remarkably, we observe low multi-photon emission at all pump-powers, with a measured maximum value of $g^{(2)}(0)$=0.0288 $\pm$ 0.0002 at P=3P_0. We thus observe a single-photon purity $1-g^{(2)}(0)$ above 97% even at maximum brightness. These values were extracted from integrating raw counts in a 2 ns window—sufficiently larger than the < 0.5 ns lifetime [9]—

around the peak at zero delay compared to the average of the 10 adjacent lateral peaks, without any background subtraction. Error bars in this work are deduced from assuming poissonian statistics in detected events.

Our APD efficiency of 32%—measured using the approach of Ref. [32]—80 MHz pump rate, and 3.6 MHz detected count rate corresponds to an absolute brightness—the probability-per-laser-pulse of finding a spectrally-isolated high-purity single-photon at the output of a single-mode fibre—of 14%, the highest reported to date. Such absolute brightness represents a clear improvement over what has been previously achieved with quantum dot-based photon sources. For instance, a drastic contrast between performance at the first lens and actual detected count rates has been common until now, e.g., reporting a brightness as high as 72% while detecting 65 kHz [33], or 143 MHz collected on the first lens but only 72 kHz available on detection [34]. Detected rates of 4.0 MHz at the single-photon level have been reported [35], however without coupling into a single-mode fibre and at the cost of high multi-photon contribution with $g^{(2)}(0)$=0.4. In fact, our source greatly exceeds, in terms of absolute brightness, the performance of any other single-photon source from any physical system, including the well established Spontaneous Parametric DownConversion source—so far considered as the premier photon source—where the equivalent (triggered) absolute brightness is well below 1%.

We note that, given our setup collection efficiency of η_{setup}=49%, *Device* 1 exhibits—for the neutral exciton state—a brightness at the first lens of 29%. Deducing the exciton lifetime from the correlation curves at low excitation power, we estimate the Purcell factor of the device to be around F_p=2, and the fraction of emission into the cavity mode around 66%. Considering an output coupling efficiency of 90%, the measured brightness in the first lens could reach 60% with a unity probability to find the QD in the neutral exciton state. However, as evidenced in the inset of Fig. 4.1a, the present QD also presents an non-negligible probability to emit from the positively- or negatively-charged exciton transition that are brought in resonance at higher temperatures. As a result, the probability of the quantum dot to be in the neutral exciton is reduced leading to the measured 29% brightness at the first lens. Note that this instability of the charge state was not observed originally in the devices under study, see Ref. [9], but appeared after sample accidental freezing.

4.3   Long timescale indistinguishability

We now explore the indistinguishability of photons emitted by *Device* 1 with various temporal distances. We perform our measurements at T=13 K to reduce phonon-induced dephasing [36], which is sufficiently close to the quantum dot cavity resonance at T=15 K. Note that contrary to most reports, the phonon sideband here is not filtered out by the 0.85 nm bandpass filter used to further suppress the laser light. Figure 4.2a depicts our experimental setup. Single-photons are injected into an unbalanced Mach-Zehnder interferometer with a variable fibre-based path-length difference designed to match—by using multiple fibres of distinct lengths—an integer multiple of 12.5 ns up to 400 ns. Polarisation control—polariser (Pol)

and a half-wave plate (HWP)—and a polarising beamsplitter (PBS) behave as a beamsplitter with tuneable reflectivity, thus balancing the photon-flux entering the interference point inside a fibre-beamsplitter (FBS) closing the Mach-Zehnder configuration. Quarter-wave plates (QWPs) and HWPs are used to tune the polarisation of interfering photons in parallel or orthogonal configuration. Time-correlation histograms from the output of this interferometer reveal the indistinguishability of photons emitted with a temporal distance $\Delta\tau_e$. Fully distinguishable photons—e.g., with orthogonal polarisation—meeting at a 50:50 beamsplitter result in a 50 % probability of being detected simultaneously at the output of the beamsplitter. This results in the peak around Δt=0 of the time-correlation measurement being about half of those at Δt>0, with the exception of peaks at $\Delta t=\Delta\tau_e$, which larger suppression indicates that the interfering photons were emitted with a temporal distance $\Delta\tau_e$. In general it can be shown for a pure single-photon source, see Appendix, that the areas $A_{\Delta t}$ centered around Δt are given by $A_k=N$, $A_{-\Delta\tau_e}=N(1-\mathcal{R}^2)$, $A_{\Delta\tau_e}=N(1-\mathcal{T}^2)$, and $A_0=N\left((\mathcal{R}^2+\mathcal{T}^2)-2\mathcal{R}\mathcal{T}V\right)$, where $k=\pm 12.5$ ns, ± 25 ns, ..., and excludes peaks at $\pm\Delta\tau_e$, N is an integration constant, $\mathcal{R}$ is the beamsplitter reflectivity, and $\mathcal{T}=1-\mathcal{R}$.

We use the visibility V to quantify the degree of indistinguishability of the source. Since the measured visibility depends both on the photon source and on the apparatus used to characterise it the latter must be accounted for. Ideally the apparatus is a beamsplitter of reflectivity $\mathcal{R}$=0.5; in our experiment $\mathcal{R}$=0.471, $\mathcal{T}$=0.529, and the visibility V is thus,

$$V = \frac{\mathcal{R}^2 + \mathcal{T}^2 - A_0/A}{2\mathcal{R}\mathcal{T}}, \tag{4.1}$$

where A is taken as the average value of A_k. Note that since the $g^{(2)}(0)$ values are intrinsic to the source, and hence affect any process in which we wish to use it, we do not correct for non-zero $g^{(2)}(0)$ in Eq. (4.1). The deduced V therefore corresponds to the raw two-photon interference visibility, and quantifies the degree of photon indistinguishability.

Figure 4.2b shows histograms for the indistinguishability of orthogonal- and parallel-polarised photons at $\Delta\tau_e$=50 ns and $P=P_0$. In virtue of Eq. (4.1), and measured $\mathcal{R}$=0.471, we obtain $V_{50\text{ns}}^{P_0}$=(0.71±0.01)% in orthogonal configuration (red histogram), and $V_{50\text{ns}}^{P_0}$=(60.31±0.60)% for parallel-polarised photons (blue histogram), where $V_{\Delta\tau_e}^{P}$ denotes visibility taken at a power P and temporal delay $\Delta\tau_e$. We observe higher visibilities at lower powers and shorter delays. For instance, the measurements in Fig. 4.2c were taken at P=0.5P_0, and reveal $V_{12.5\text{ns}}^{0.5P_0}$=(67.52±0.78)% at a temporal delay (blue histogram) of $\Delta\tau_e$=12.5 ns. Remarkably, we find that indistinguishability is robust in the temporal domain. Even after 33 consecutive emitted photons (orange histogram), at $\Delta\tau_e$=400 ns, it only decreases to $V_{400\text{ns}}^{0.5P_0}$=(59.97±0.76)%. That is, less than 8% visibility decrease in $\sim$ 400 ns. All V values with the non-resonant scheme are obtained without any background correction.

To thoroughly examine the indistinguishability properties of *Device* 1, we carried out power- and temporal-dependent measurements, see Fig. 4.3a. All these measured V are within the 50%−70% range, thus showing conclusive quantum interference at all measured powers and timescales. The large available photon flux allows us to gather more than 100 visibility values
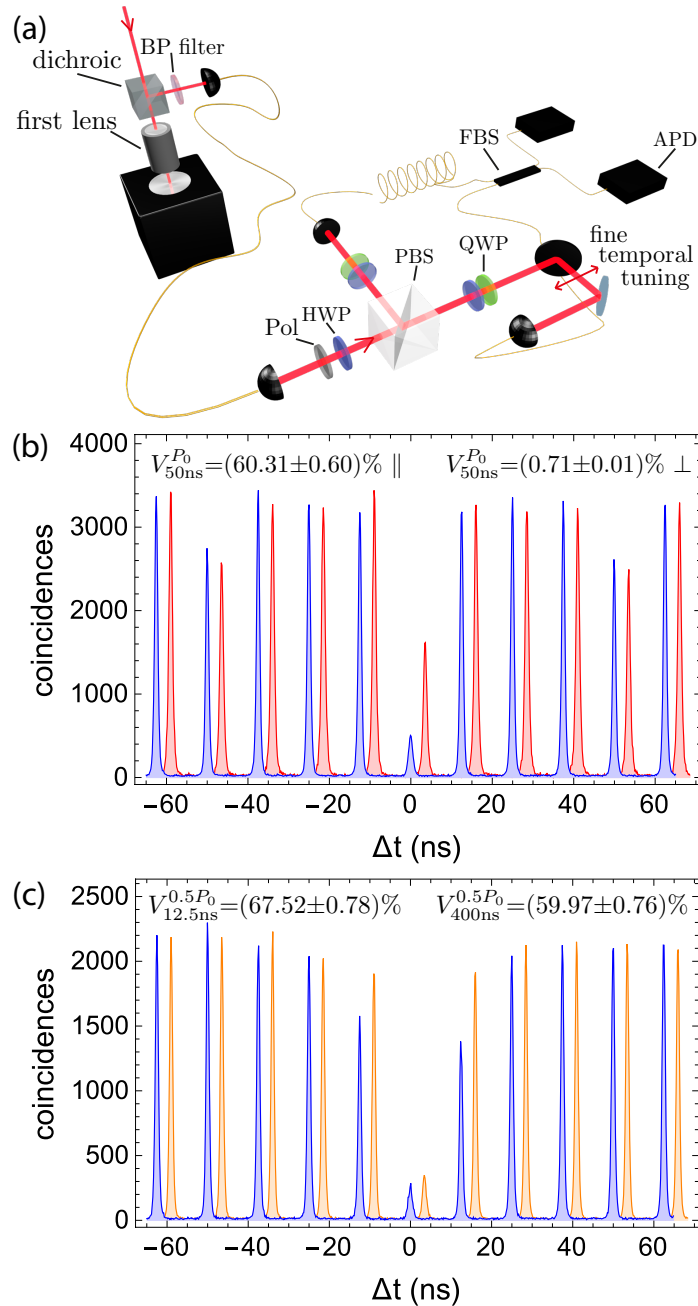
Figure 4.2: Two-photon interference between temporally-distant photons. a) A simple unbalanced Mach-Zehnder interferometer with a path-length difference of $\Delta\tau_e$ probes the indistinguishability of two photons emitted with the same $\Delta\tau_e$ temporal separation. b) Interference histograms of orthogonal- (red) and parallel-polarised (blue) photons with $\Delta\tau_e$=50 ns, at saturation of the quantum dot. (Note the suppression at $\Delta\tau_e$, see text for details). c) Interference of parallel-polarised photons with $\Delta\tau_e$=12.5 ns (blue) and $\Delta\tau_e$=400 ns (orange), taken at P=0.5P_0. A temporal offset of 3.5 ns has been introduced between histograms for clarity.

with measurement errors sufficiently small to identify an interesting behaviour in this narrow visibility range. At any given $\Delta\tau_e$, V is linear in P, see Appendix, and we simply use $\overline{V}=V_{\Delta\tau_e}^{max}+m_{\Delta\tau_e}P$ to characterise the P-dependence of V at fixed $\Delta\tau_e$. Conversely, at fixed P, V decreases monotonically and asymptotically in $\Delta\tau_e$, flattening to fixed values at longer

timescales.

We model this behaviour by considering a time-dependent wandering of the spectral line as the origin of the temporal modulation. That is, the frequency of every emitted photon $\omega(t){=}\omega_0{+}\delta\omega(t)$ varies in time according to some wandering function $\delta\omega(t)$ occurring in timescales much larger than the photon lifetime. Our problem is then equivalent to finding the mutual interference visibility between independent sources with finite frequency detuning [37], which is given by $V(0)/\left(1+\delta\omega_r^2\right)$ in the case where $V(0)$ is the degree of indistinguishability for each source alone (equal value for both), and $\delta\omega_r$ is the ratio of the frequency detuning to the spectral linewidth of the sources (equal linewidth for both). If this mismatch arises due to spectral wandering within the same source, then the time-averaged relative detuning squared is given by $2\delta\omega_r^2\left(1-\exp\left(-\Delta\tau_e/\tau_c\right)\right)$, with τ_c a characteristic wandering timescale, see Appendix for more details. We thus derive the visibility of temporally-distant photons:

$$V\left(\Delta\tau_e\right) = \frac{V(0)}{1 + 2\delta\omega_r{}^2\left(1 - e^{-\Delta\tau_e/\tau_c}\right)}. \tag{4.2}$$

To obtain a statistically meaningful temporal behaviour, we used the fitted values of $\overline{V}$ at
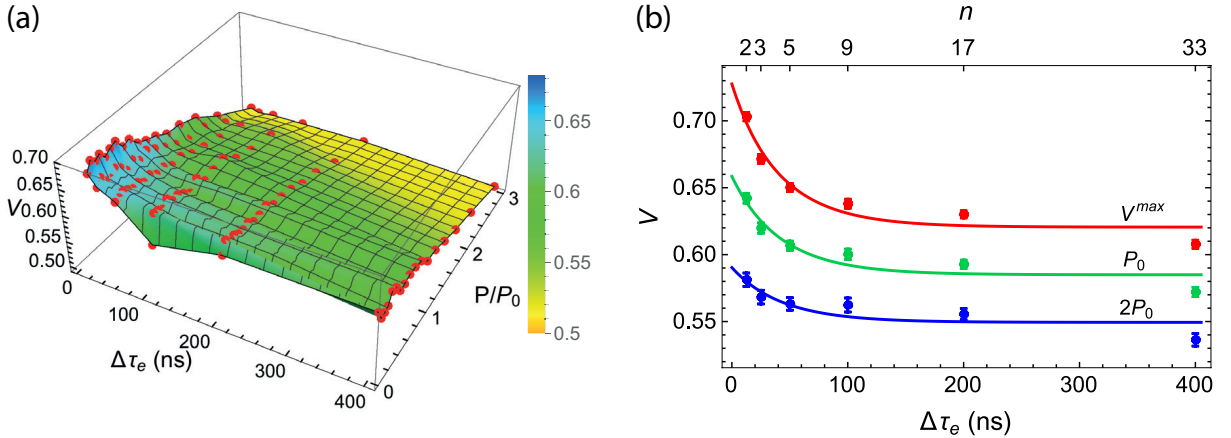
Figure 4.3: Power- and temporal-dependent two-photon interference. a) Over >100 measured visibilities (red points) showing conclusive quantum interference, i.e. $V{>}0.5$, at all measured powers and timescales. Coloured surface is an interpolation to the data. b) Fitted values of $\overline{V}$ at different $\Delta\tau_e$ (bottom axis), for $P{=}0$ (red), $P{=}P_0$ (green), and $P{=}2P_0$ (blue), showing interference between a first and n-th consecutive emitted photon (top axis). Curves are fits to our model in Eq. (4.2).

different $\Delta\tau_e$, for powers $P{=}0$, $P{=}P_0$, and $P{=}2P_0$. These values are plotted in Fig. 4.3b and are in good agreement with our model in Eq. (4.2). In the limit of low powers, we obtain $V(0){=}(72.8\pm2.4)\%$, $\tau_c{=}(45.5\pm19.1)$ ns, and $\delta\omega_r{=}(29.4\pm3.1)\%$; whereas at high powers, at $P{=}2P_0$, these parameters are $V(0){=}(59.0\pm2.0)\%$, and $\delta\omega_r{=}(19.3\pm4.5)\%$. The maximum degree of indistinguishability $V(0)$ decreases only by 13.8% with increasing power, evidencing a slight increase of pure dephasing of the exciton transition. On the contrary, the relative amplitude of the spectral wandering decreases by 34%, evidencing that spectral diffusion is

significantly reduced at higher powers, as recently observed in nanowire based devices [38]. Note that the large relative error in τ_c is due to a small relative decay in V, an uncertainty that increases with increasing power. Thus—although it is reasonable to assume that τ_c itself is power-dependent—we extracted τ_c only at $P=0$ and used it as a fixed parameter for the fits at higher powers.

The decrease of the indistinguishability by few percents for temporally distant photons demonstrates a very limited spectral diffusion in our micropillar devices. This observation is in striking contrast to previous measurements on single photon sources based on alternative approaches for efficient photon extraction, such as nanowires [38], or micro lenses [29]. A significantly lower stability of the electrostatic environment of the QD can reasonably be attributed to the close proximity of free surfaces in the latter. Indeed, as indicated by the observation of three emission lines from the same QD, even the micropillar devices under study do not provide a fully stable charge state for the QDs, an effect that we observe to be dependent on the quality of the etched surfaces. This makes strictly resonant spectroscopy difficult without an additional non-resonant excitation, a situation also observed in other micropillar devices [26].

Therefore, to explore the indistinguishability of temporally-distant photons under strictly resonant excitation, we turn to electrically controlled micropillars and present data on two devices, *Device* 2 and *Device* 3[1]. These devices consist of quantum dots deterministically coupled to micropillars embedded in cylindrical gated structures with p- and n-contacts respectively defined on the top and bottom sides of the device, resulting in an effective p-i-n diode structure onto which an electric field can be applied. (See Ref. [28] for a detailed description of the device). We perform our measurements at $T=9$ K and tune the emission into cavity-resonance via an applied bias voltage of -0.3 V. This sample is cooled by gas exchange in a closed-cycle cryostat, and is pumped by shaped 15 ps laser pulses at 82 MHz repetition rate. The experimental setup used for photon collection is reported in Ref. [28], and the appartus used for the temporal-dependent measurements is conceptually identical to that in Fig. 4.2a.

Resonant-excitation allows us to probe two-photon interference in a regime excelling in indistinguishability performance. Indeed, for *Device* 2 we obtain $V^\pi_{12.2\mathrm{ns}}=(95.0\pm1.0)\%$ at a short temporal separation, decreasing only to $V^\pi_{158.5\mathrm{ns}}=(90.6\pm1.7)\%$ at long timescales, see Figs. 5.4a, and 5.4b. We observe a high single-photon purity quantified by $g^{(2)}(0)=0.015\pm0.007$ at π-pulse, see Fig. 5.4c, where the non-vanishing $g^{(2)}(0)$ primarily consists of background noise and thus a value $1-g^{(2)}(0)$ of 98.5% represents a lower bound on the intrinsic single-photon purity. Indistinguishability measurements at various temporal distances, see Fig. 5.4d, reveal plateaus at high values: Up to a first and fourteenth photon, separated by ~150 ns, exhibit an indistinguishability greater than 90%. The curve is a fit to Eq. (4.2), with a maximum indistinguishability value of $V(0)=96.6\%$, $\tau_c=54.4$ ns, and $\delta\omega_r=17.8\%$. The reproducibility of our results, thanks to a deterministic fabrication, is evidenced by similar indistinguishability values obtained on *Device* 3: $V^\pi_{12.2\mathrm{ns}}=(96.1\pm0.8)\%$ at a short temporal delay, and $V^\pi_{463\mathrm{ns}}=(87.8\pm1.6)\%$ for a first and thirty-ninth photon separated by 463 ns. These values of indistinguishability are

---

[1]The measurements under strictly-resonant excitation were performed by our collaborators in the group of Prof. Pascale Senellart. Those involved in these measurements are listed as authors of the published work.
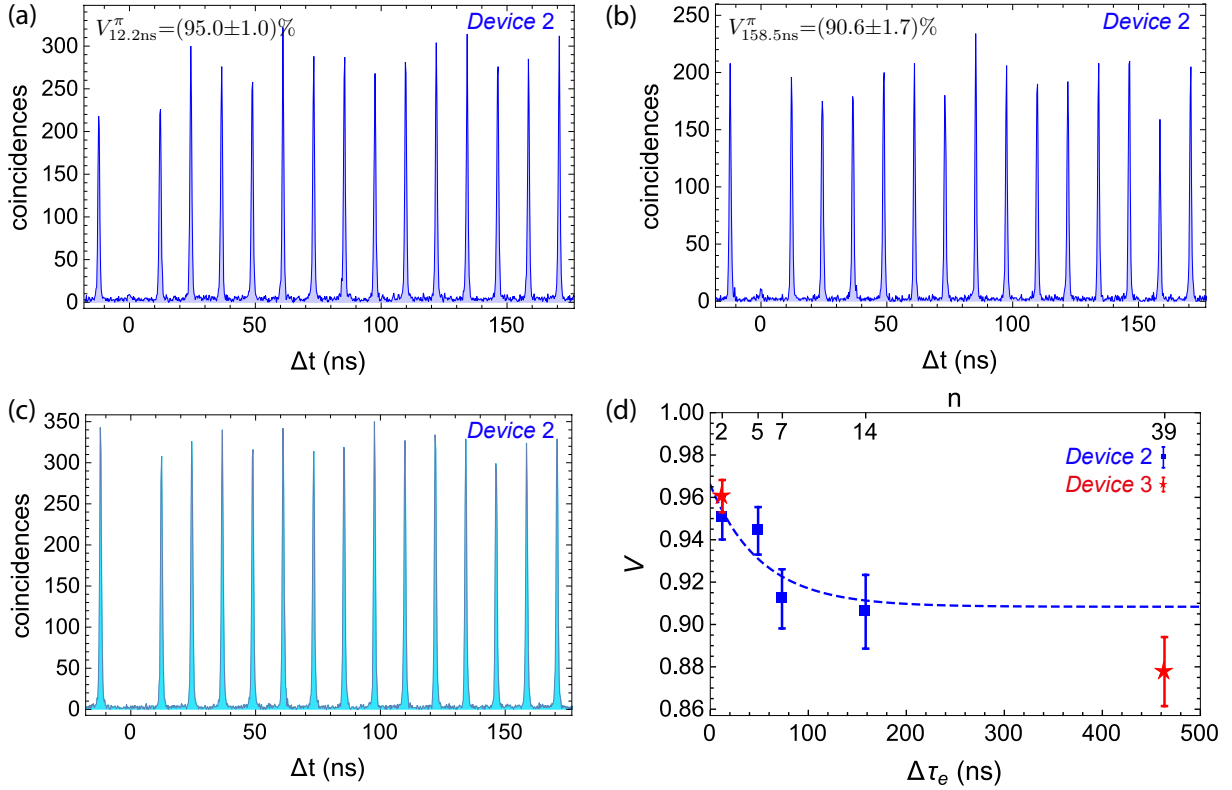
Figure 4.4: Temporal-dependent indistinguishability under strictly resonant excitation. Two-photon interference histograms with *Device 2* of parallel-polarised photons at a) $\Delta\tau_e$=12.2 ns, and b) $\Delta\tau_e$=158.5 ns, under a π-pulse preparation. c) Second-order autocorrelation measurement at π-pulse. d) Indistinguishability between a first and n-th consecutive emitted photon from *Device 2* (blue) and *Device 3* (red). Indistinguishability remains robust in the temporal domain, decreasing only by 4.4% in $\sim$ 159 ns (down to 90.6%) for *Device 2*, and by 8.3% in $\sim$ 463 ns (down to 87.8%) for *Device 2* . The curve is a fit of the data from *Device 2* to Eq. (4.2).

corrected for the measured background noise arising from detector dark counts: The experimental setup used for these resonant-excitation measurements presents a low collection efficiency, thus an integration of raw detected counts that includes the background noise, which at zero delay is as large as non-vanishing counts due to photon dinstinguishability, would under-estimate the intrinsic degrees of indistinguishability in our devices, see the Appendix for details on this method. No correction for non-vanishing $g^{(2)}(0)$ was included.

Note that a high absolute brightness with this recently developed technology is yet to be achieved. However, since the mode profile of connected pillars is the same as isolated ones [27] and a photon extraction efficiency at the first lens of 65% has been reported on this sample [28], the same experimental methods as before should allow even higher absolute efficiencies than the 14% reported here.

4.4   Discussion and conclusion

We provided here strong evidence that our sources emit long streams of indistinguishable photons. Under non-resonant excitation, even a first and a thirty-third consecutive photon, separated by 400 ns, display conclusive quantum interference. For a fixed pump power, photon indistinguishability decreases only a few percent—about 8% at low powers and less than 4% at higher powers—before flattening to fixed values at longer timescales. This contrasts favourably to previous works, where photon indistinguishability has been observed to decrease by 40% in only 10 ns [29]. Moreover, under strictly-resonant excitation, photon indistinguishability between a first and thirty-ninth photon remained at 88%. Interestingly, the observation of only small reductions in the temporal domain indicate that non-unity indistinguishability under non-resonant excitation is mainly caused by homogenous broadening of the spectral linewidth (governing coherence times at short temporal delays), and a limited inhomogeneous broadening (governing effective coherence times at longer temporal delays). The relative amplitude of the spectral diffusion at saturation is similar for both resonant and non-resonant excitation. However, *Device* 1 operates in a limited Purcell regime whereas *Devices* 2 and 3 operate with a Purcell factor around $7-10$, leading to an increased radiative exciton linewidth. From this, we conclude that, although the application of an electrical bias in p-i-n diode structures allows a good control of the QD charge states, it does not lead to a significant decrease in the spectral wandering phenomena. The excellent indistinguishability observed in *Devices* 2 and 3 arises mainly from reduced pure dephasing of the exciton state, increased Purcell factor and reduced time jitter in a resonant excitation scheme.

Our reported indistinguishability values correspond to the longest temporal delays here studied, at a particular pump repetition rate of 80 MHz: It only represents a lower bound on the number of photons we can generate—limited by radiative lifetimes in the order of a few hundred picoseconds—that can be further used in quantum information processing protocols with solid-state sources [39]. Previous works investigating noise spectra in resonance fluorescence have shown evidence of long streams of near transform-limited photons [40] in timescales potentially reaching seconds [41]. In fact, *Device* 2 has recently been shown to emit photons with near transform-limited linewidth in a millisecond timescale [42], in which case we would expect that our devices are producing at least hundreds of thousands of highly indistinguishable single-photons.

Our findings are especially relevant in implementations with time-bin encoded degrees of freedom, such as some recently proposed schemes of linear-optics quantum computing with time-bin encoding [43, 44], where the indistinguishability of temporally-distant photons will directly determine quantum fidelities of the implemented protocols. Scaling solid-state multi-photon sources by combining multiple independent emitters remains challenging, as atomic growth accuracy or complex individual electric control over multiple devices is needed. These requirements can be circumvented by making use of a single photon source emitting a long temporal stream of highly indistinguishable photons that can be demultiplexed by fast active

optics.

A high absolute brightness will be critical for successfully implementing multi-photon experiments with these sources, where their downconversion counterparts currently require experimental runs of hundreds of hours [45, 46]. The key role of high emission yields in these devices has been made explicit in the recent demonstration of a solid-state based multi-photon experiment [47], realised with *Device* 1, where integration times outperformed those in equivalent downconversion implementations by two-orders of magnitude. Achieving high absolute efficiencies, and thus allowing the scaling of multi-photon experiments to larger photon numbers, becomes feasible due to Purcell-enhancement of *deterministically*-coupled quantum dot-micropillar devices [9, 27, 28, 37, 48]. This necessary condition is unlikely to be found by chance with non-deterministic approaches, with reported [48] device yields of $\sim 0.01\%$ [26]. Thus, the deterministic fabrication, high absolute brightness, and long timescale indistinguishability of our devices will enable large-scale applications that have been heretofore impossible.

4.5 Appendix

4.5.1 Areas in time-correlation histograms

Here we deduce the area distribution of the time-correlation measurements described in the main text. For simplicity, we first consider two (fully-distinguishable) single-photons distributed in time-bins $\{t_1, t_2\}$, entering an unbalanced Mach-Zehnder interferometer composed of a first 50:50 beamsplitter and a second beamsplitter with reflectance $\mathcal{R}$ (transmittance $\mathcal{T}=1-\mathcal{R}$). Our task is to find all possible output distributions leading to a coincidence detection between events separated in time by Δt. There are two timescales relevant in such coincidence measurements: the difference in occupied time-bins $\delta t=|t_2-t_1|$, and the temporal delay inside the unbalanced interferometer Δ. By inspecting this reduced scenario, we can find that there are 8 events leading to a coincidence detection, as depicted in Fig. 4.5. This results in local patterns of peak areas $A_{\Delta t}$ given by: $A_{-\delta t-\Delta}=\mathcal{R}^2$, $A_{-\delta t}=2\mathcal{R}\mathcal{T}$, and $A_{-\delta t+\Delta}=\mathcal{T}^2$, the local pattern around $-\delta t$; and $A_{\delta t-\Delta}=\mathcal{R}^2$, $A_{\delta t}=2\mathcal{R}\mathcal{T}$, and $A_{\delta t+\Delta}=\mathcal{T}^2$, the local pattern around δt. From this, we find simple rules for the time-correlation measurement of an array of single-photons distributed in arbitrary time-bins $\{t_i\}$ passing through a Δ-unbalanced Mach-Zehnder:

rule 1: Find all possible temporal delays δt relating each pair of photons within the given time-bin distribution.

rule 2: Around each $\pm\delta t$, assign the relative frequency of events $\{\mathcal{R}^2, 2\mathcal{R}\mathcal{T}, \mathcal{T}^2\}$ at temporal delays $\Delta t=\{\pm\delta t-\Delta, \pm\delta t, \pm\delta t+\Delta\}$.
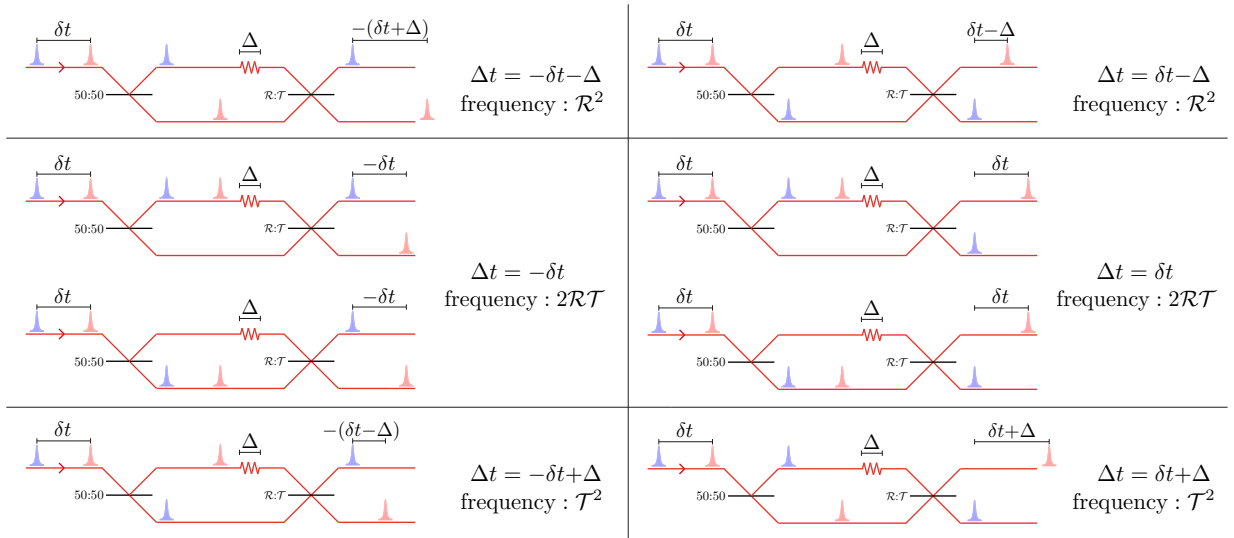
Figure 4.5: Two consecutive single-photons separated by δt passing through a Δ-unbalanced Mach-Zehnder interferometer. 8 outcome distributions, occurring with a given relative frequency, lead to a coincidence signal between events separated in time by Δt. The relative delay Δt is positive if a detector in the upper output fires first, and it is negative in the opposite case.

We note that these two simple rules describe different interesting histograms relevant in the literature. For instance, by simply identifying the involved parameters, one can find histograms of $g^{(2)}(\Delta t)$ measurements of arbitrary $|n\rangle$ Fock states by considering n single-photons occupying

the same time-bin, resulting in distributions agreeing with $g^{(2)}(0)=1-1/n$, or the well known 5-peak structures in two-photon interference experiments involving pairs of photons separated by $\Delta\tau_e < 12.5$ ns repeated every 12.5 ns.

Now, the experiment described in the main text is the particular case of an infinitely long stream of single-photons separated by a fixed $\delta t{=}12.5$ ns, and passing through an unbalanced interferometer with $\Delta{=}\Delta\tau_e$. Under this consideration, and following *rule 1* and *rule 2*, we derive the distribution of areas $A_{\Delta t}$, given by: $A_k{=}N$, $A_{-\Delta\tau_e}{=}N(1-\mathcal{R}^2)$, $A_{\Delta\tau_e}{=}N(1-\mathcal{T}^2)$, and $A_0{=}N\left((\mathcal{R}^2 + \mathcal{T}^2) - 2\mathcal{R}\mathcal{T}V\right)$, with $k{=}\pm 12.5$ ns, ± 25 ns, ..., excluding peaks at $\pm\Delta\tau_e$, and N an integration constant. The visibility term V in A_0 appears from noticing (in virtue of *rule 1* and *rule 2*) that the area at $\Delta t{=}0$ for fully-distinguishable photons is $A_0^{V=0}{=}N(\mathcal{R}^2 + \mathcal{T}^2)$, and then one simply uses the well-known relation $V{=}\left(1-A_0/A_0^{V=0}\right)(\mathcal{R}^2+\mathcal{T}^2)/(2\mathcal{R}\mathcal{T})$, with A_0 relating the coincidence rate at zero delay of photons with non-zero V indistinguishability.

4.5.2 Visibility power-dependence

Following the main text, the interference visibility V of two photons separated in time by $\Delta\tau_e$ exhibits a linear-dependence in the pump power P. For a given $\Delta\tau_e$, we measure V at various values of P, up to three saturation powers $P{=}3P_0$, and fit the data to $\overline{V}{=}V_{\Delta\tau_e}^{max}+m_{\Delta\tau_e}P$. Figure 4.6 shows the power-dependence of V for $\Delta\tau_e{=}12.5$ ns, $\Delta\tau_e{=}50$ ns, and $\Delta\tau_e{=}400$ ns. The fitted parameters are $V_{12.5\text{ns}}^{max}{=}(70.3{\pm}0.3)\%$, $m_{12.5\text{ns}}{=}-(6.1{\pm}0.2)\%$ at short timescales; $V_{50\text{ns}}^{max}{=}(65.0{\pm}0.3)\%$, $m_{50\text{ns}}{=}-(4.4{\pm}0.2)\%$ at moderate timescales; and $V_{400\text{ns}}^{max}{=}(60.8{\pm}0.3)\%$, $m_{400\text{ns}}{=}-(3.6{\pm}0.2)\%$ at the longest timescales explored in this work.
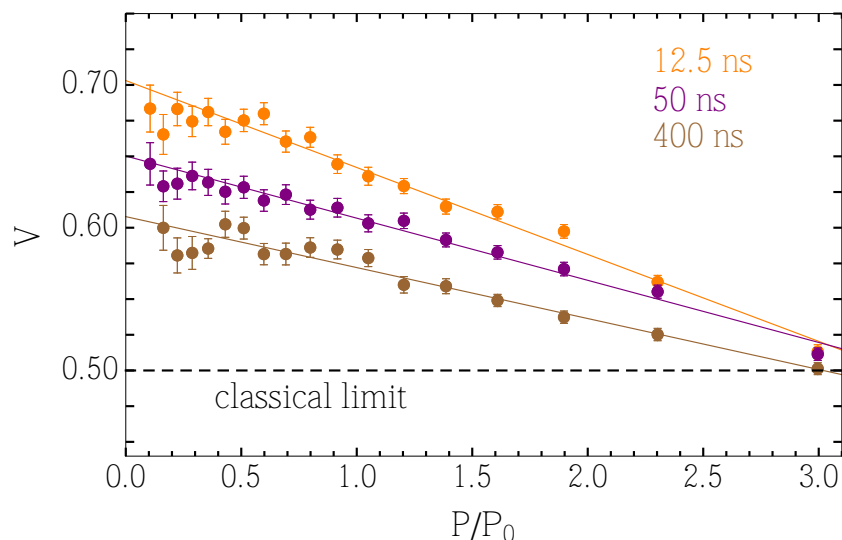
Figure 4.6: Power-dependence of V for $\Delta\tau_e{=}12.5$ ns (orange), $\Delta\tau_e{=}50$ ns (purple), and $\Delta\tau_e{=}400$ ns (brown). Curves are fits to $\overline{V}{=}V_{\Delta\tau_e}^{max}+m_{\Delta\tau_e}P$. V is above 50% (the classical limit) at all powers and timescales here explored.

4.5.3 Visibilities of temporally-distant photons

The interference visibility of two photons from two sources a and b reads [37]:

$$V = \left(\frac{\gamma_a \gamma_b}{\gamma_a + \gamma_b}\right) \frac{(\gamma_a + \gamma_b + \gamma_a^* + \gamma_b^*)}{[(\gamma_a + \gamma_b + \gamma_a^* + \gamma_b^*)/2]^2 + \delta\omega^2}, \tag{4.3}$$

where the γ_i are the radiative rates, γ_i^* the pure dephasing rates, and $\delta\omega$ the frequency detuning between the two sources. If the interfering photons are emitted by the same quantum dot, we assume that $\gamma_a = \gamma_b = \gamma$ and $\gamma_a^* = \gamma_b^* = \gamma^*$ are constant, but only the frequency $\omega = \omega_0 + \delta\omega(t)$ varies over time (i.e. spectral wandering) around a central value ω_0. This model makes sense here as the timescale over which ω varies is much larger than the radiative lifetime. Then Eq. (4.3) reduces to:

$$V = \left\langle \frac{V(0)}{1 + \delta\omega_r^2} \right\rangle, \tag{4.4}$$

where we have used $V(0) = \gamma/(\gamma + \gamma^*)$ the "intrinsic" degree of indistinguishability, and $\delta\omega_r = \delta\omega/(\gamma + \gamma^*)$ the ratio between the frequency detuning and the spectral linewidth $\gamma + \gamma^*$.

One can define a time correlation function for the frequency fluctuations as

$$F(\Delta\tau_e) = \langle \delta\omega(t)\delta\omega(t + \Delta\tau_e) \rangle = \langle \delta\omega^2 \rangle f(\Delta\tau_e), \tag{4.5}$$

then, the frequency difference as a function of the delay $\Delta\tau_e$ can be expressed as

$$
\begin{aligned}
\langle \delta\omega^2(\Delta\tau_e) \rangle &= \langle (\delta\omega(t + \Delta\tau_e) - \delta\omega(t))^2 \rangle \\
&= 2 \langle \delta\omega^2 \rangle (1 - f(\Delta\tau_e)).
\end{aligned}
\tag{4.6}
$$

A common assumption is to assume an exponential correlation function

$$f(\Delta\tau_e) = e^{-\Delta\tau_e/\tau_c}, \tag{4.7}$$

with τ_c a characteristic wandering timescale. Which is expected for a Markovian dynamics of the environnement. An additional input which is required is the distribution for $\delta\omega$. Generally one assumes a Gaussian distribution, but for simplicity, and without loss of generality, we take a two-value distribution $\delta\omega = \pm\sqrt{\langle \delta\omega^2 \rangle}$, so that:

$$
\begin{aligned}
V(\Delta\tau_e) &= \left\langle \frac{V(0)}{1 + \delta\omega_r^2(\Delta\tau_e)} \right\rangle \\
&= \frac{V(0)}{1 + \langle \delta\omega_r^2(\Delta\tau_e) \rangle} \\
&= \frac{V(0)}{1 + 2\delta\omega_r^2 \left(1 - e^{-\Delta\tau_e/\tau_c}\right)}
\end{aligned}
\tag{4.8}
$$

4.5.4 Extraction of visibility under resonant excitation

Here we describe the methods to extract the raw and corrected two-photon interference visibilities under strictly-resonant excitation and π-pulse preparation, see Fig. 4.7. Figure 4.7a shows the interference histogram of two photons separated by $\Delta\tau_e$=12.2 ns, from which a visibility is extracted via $V = (\mathcal{R}^2 + \mathcal{T}^2 - A_0/A)/(2\mathcal{R}\mathcal{T})$, where A_0 is the area of the peak around Δt=0, and A is taken as the average area of 14 adjacent peaks (excluding the peak at $\Delta\tau_e$). These areas are taken as the integrated counts within a temporal window of 2 ns (considerably longer than the subnanosecond lifetimes) around $\Delta t = k \times 12.2$ ns, with $k = 0, 2, 3, ..., 15$, see Fig. 4.7b. The resulting integrated areas are shown in Fig. 4.7c, from which we extract a raw $V^\pi_{12.2\text{ns}} = (89.0 \pm 1.5)\%$.
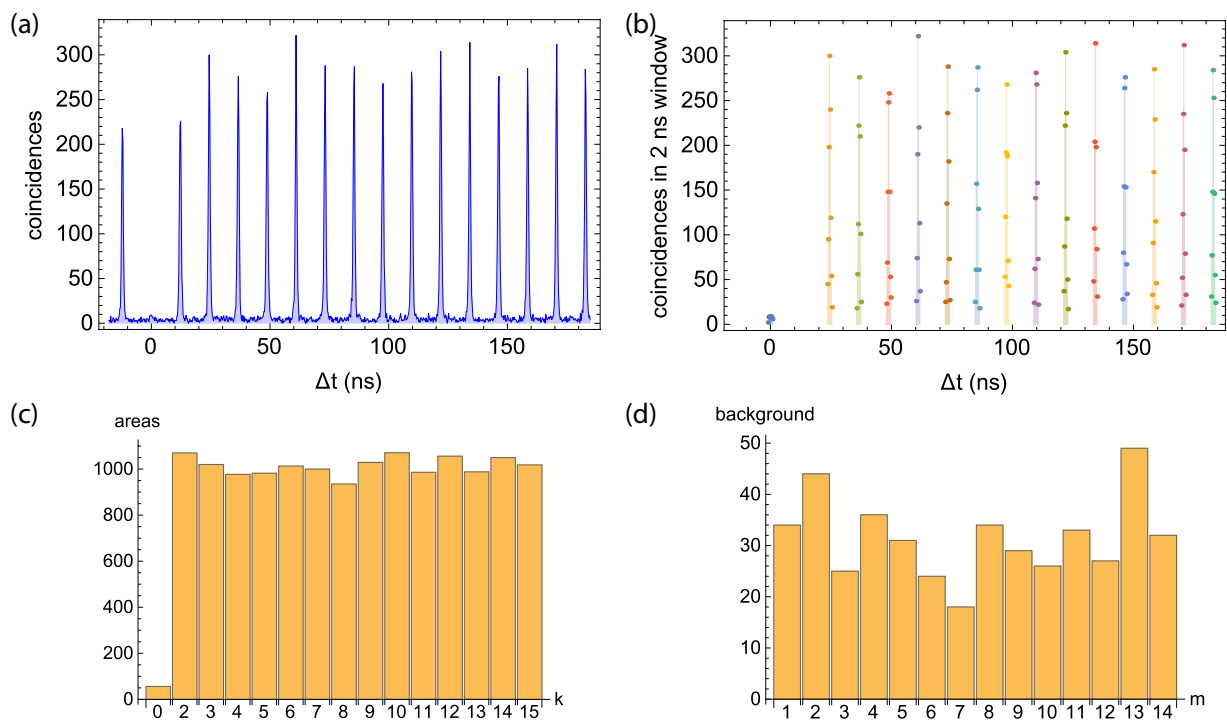
Figure 4.7: Method to extract the raw and corrected interference visibilities. a) Interference histogram of two photons separated by $\Delta\tau_e$=12.2 ns. b) Subset of data involved in the evaluation of V. c) Integrated counts from data in b). d) Measured background in between peaks.

As described in the main text, the remaining non-vanishing area at Δt=0 is indeed quite small and it is on the order of experimental noise. We take into account this noise by integrating coincidence counts within a 2 ns window but now located in between peaks, that is at $\Delta t = (m + 1/2) \times 12.2$ ns, with $m = 1, 2, ..., 14$, see Fig.4.7d. After subtracting the average of these background counts to the areas in Fig.4.7c, we obtained the corrected visibility $V^\pi_{12.2\text{ns}} = (95.0 \pm 1.0)\%$. These same methods were employed for all measurements under strictly-resonant excitation. Figure 4.8 shows both raw and corrected visibilities for two devices (*Device 2* and 3) extracted with this method.

Measurements under quasi-resonant excitation, as described in the main text, exhibit a noise level < 1%, and therefore no noise-correction was employed.
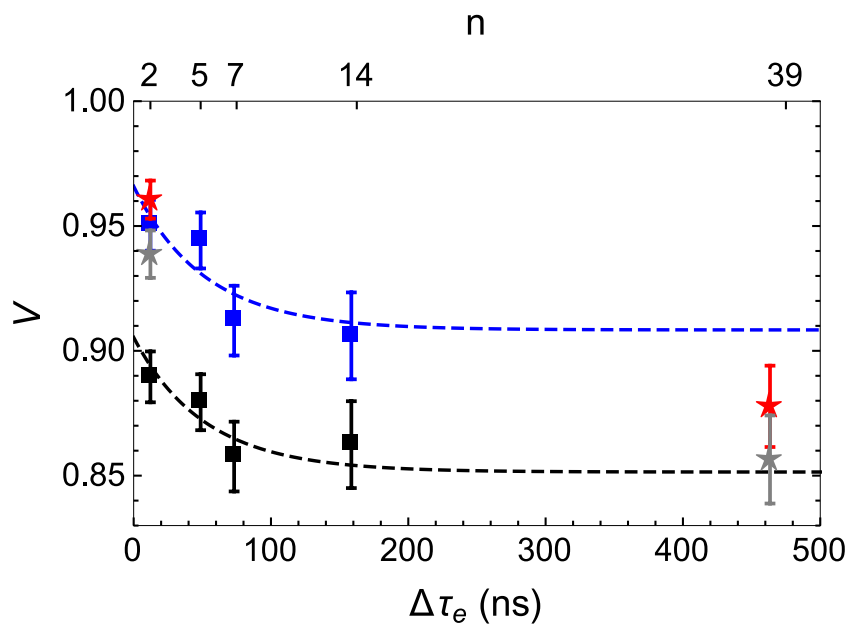
Figure 4.8: Indistinguishability vs temporal distance. Blue squares are corrected indistinguisha-bilities taken with *Device 2*, and red stars are the corrected values taken with *Device 3*. Black squares are raw values from *Device 2*, and gray stars are raw values from *Device 3*.

References

[1] Hong, C. K., Ou, Z. Y. & Mandel, L. Measurement of subpicosecond time intervals between two photons by interference. *Phys. Rev. Lett.* **59**, 2044–2046 (1987).

[2] Legero, T., Wilk, T., Hennrich, M., Rempe, G. & Kuhn, A. Quantum beat of two single photons. *Phys. Rev. Lett.* **93**, 070503 (2004).

[3] Duan, L.-M. & Monroe, C. *Colloquium* : Quantum networks with trapped ions. *Rev. Mod. Phys.* **82**, 1209–1224 (2010).

[4] Bernien, H. *et al.* Two-photon quantum interference from separate nitrogen vacancy centers in diamond. *Phys. Rev. Lett.* **108**, 043604 (2012).

[5] Kiraz, A. *et al.* Indistinguishable photons from a single molecule. *Phys. Rev. Lett.* **94**, 223602 (2005).

[6] Lang, C. *et al.* Correlations, indistinguishability and entanglement in hong-ou-mandel experiments at microwave frequencies. *Nat Phys* **9**, 345–348 (2013).

[7] Pittman, T., Jacobs, B. & Franson, J. Heralding single photons from pulsed parametric down-conversion. *Optics Communications* **246**, 545 – 550 (2005).

[8] Santori, C., Fattal, D., Vuckovic, J., Solomon, G. S. & Yamamoto, Y. Indistinguishable photons from a single-photon device. *Nature* **419**, 594–597 (2002).

[9] Gazzano, O. *et al.* Bright solid-state sources of indistinguishable single photons. *Nat Commun* **4**, 1425 (2013).

[10] O'Brien, J. L., Furusawa, A. & Vuckovic, J. Photonic quantum technologies. *Nat. Photon.* **3**, 687–695 (2009).

[11] Bouwmeester, D. *et al.* Experimental quantum teleportation. *Nature* **390**, 575–579 (1997).

[12] Wang, X.-L. *et al.* Quantum teleportation of multiple degrees of freedom of a single photon. *Nature* **518**, 516–519 (2015).

[13] Kwiat, P. G., Waks, E., White, A. G., Appelbaum, I. & Eberhard, P. H. Ultrabright source of polarization-entangled photons. *Phys. Rev. A* **60**, R773–R776 (1999).

[14] Kim, T., Fiorentino, M. & Wong, F. N. C. Phase-stable source of polarization-entangled photons using a polarization sagnac interferometer. *Phys. Rev. A* **73**, 012316 (2006).

[15] Dousse, A. *et al.* Ultrabright source of entangled photon pairs. *Nature* **466**, 217–220 (2010).

[16] Knill, E., Laflamme, R. & Milburn, G. J. A scheme for efficient quantum computation with linear optics. *Nature* **409**, 46–52 (2001).

[17] Kok, P. *et al.* Linear optical quantum computing with photonic qubits. *Rev. Mod. Phys.* **79**, 135–174 (2007).

[18] Michler, P. *et al.* A quantum dot single-photon turnstile device. *Science* **290**, 2282–2285 (2000).

[19] Vuckovic, J., Fattal, D., Santori, C., Solomon, G. S. & Yamamoto, Y. Enhanced single-photon emission from a quantum dot in a micropost microcavity. *Applied Physics Letters* **82**, 3596–3598 (2003).

[20] Pelton, M. *et al.* Efficient source of single photons: A single quantum dot in a micropost microcavity. *Phys. Rev. Lett.* **89**, 233602 (2002).

[21] Lund-Hansen, T. *et al.* Experimental realization of highly efficient broadband coupling of single quantum dots to a photonic crystal waveguide. *Phys. Rev. Lett.* **101**, 113903 (2008).

[22] Madsen, K. H. *et al.* Efficient out-coupling of high-purity single photons from a coherent quantum dot in a photonic-crystal cavity. *Phys. Rev. B* **90**, 155303 (2014).

[23] Gérard, J. M. *et al.* Enhanced spontaneous emission by quantum boxes in a monolithic optical microcavity. *Phys. Rev. Lett.* **81**, 1110–1113 (1998).

[24] He, Y.-M. *et al.* On-demand semiconductor single-photon source with near-unity indistinguishability. *Nat Nano* **8**, 213–217 (2013).

[25] Wei, Y.-J. *et al.* Deterministic and robust generation of single photons from a single quantum dot with 99.5% indistinguishability using adiabatic rapid passage. *Nano Letters* **14**, 6515–6519 (2014). PMID: 25357153.

[26] Ding, X. *et al.* On-demand single photons with high extraction efficiency and near-unity indistinguishability from a resonantly driven quantum dot in a micropillar. *Phys. Rev. Lett.* **116**, 020401 (2016).

[27] Nowak, A. K. *et al.* Deterministic and electrically tunable bright single-photon source. *Nat Commun* **5**, 3240 (2014).

[28] Somaschi, N. *et al.* Near-optimal single-photon sources in the solid state. *Nat Photon* **advance online publication**, – (2016).

[29] Thoma, A. *et al.* Exploring dephasing of a solid-state quantum emitter via time- and temperature-dependent hong-ou-mandel experiments. *Phys. Rev. Lett.* **116**, 033601 (2016).

[30] Dousse, A. *et al.* Controlled light-matter coupling for a single quantum dot embedded in a pillar microcavity using far-field optical lithography. *Phys. Rev. Lett.* **101**, 267404 (2008).

[31] Grilli, E., Guzzi, M., Zamboni, R. & Pavesi, L. High-precision determination of the temperature dependence of the fundamental energy gap in gallium arsenide. *Phys. Rev. B* **45**, 1638–1644 (1992).

[32] Hadfield, R. H. Single-photon detectors for optical quantum information applications. *Nat Photon* **3**, 696–705 (2009).

[33] Claudon, J. *et al.* A highly efficient single-photon source based on a quantum dot in a photonic nanowire. *Nat Photon* **4**, 174–177 (2010).

[34] Schlehahn, A. *et al.* Single-photon emission at a rate of 143 mhz from a deterministic quantum-dot microlens triggered by a mode-locked vertical-external-cavity surface-emitting lasermhz from a deterministic quantum-dot microlens triggered by a mode-locked vertical-external-cavity surface-emitting laser. *Applied Physics Letters* **107** (2015).

[35] Strauf, S. *et al.* High-frequency single-photon source with polarization control. *Nat Photon* **1**, 704–708 (2007).

[36] Unsleber, S. *et al.* Two-photon interference from a quantum dot microcavity: Persistent pure dephasing and suppression of time jitter. *Phys. Rev. B* **91**, 075413 (2015).

[37] Giesz, V. *et al.* Cavity-enhanced two-photon interference using remote quantum dot sources. *Phys. Rev. B* **92**, 161302 (2015).

[38] Reimer, M. E. *et al.* Overcoming power broadening of the quantum dot emission in a pure wurtzite nanowire. *arXiv:1407.2833* (2014).

[39] Gazzano, O. *et al.* Entangling quantum-logic gate operated with an ultrabright semiconductor single-photon source. *Phys. Rev. Lett.* **110**, 250501 (2013).

[40] Kuhlmann, A. V. *et al.* Charge noise and spin noise in a semiconductor quantum device. *Nat Phys* **9**, 570–575 (2013).

[41] Kuhlmann, A. V. *et al.* Transform-limited single photons from a single quantum dot. *Nat Commun* **6** (2015).

[42] Giesz, V. *et al.* Coherent control of a solid-state quantum bit with few-photon pulses. *arXiv:1512.04725* (2015).

[43] Humphreys, P. C. *et al.* Linear optical quantum computing in a single spatial mode. *Phys. Rev. Lett.* **111**, 150501 (2013).

[44] Rohde, P. P. Simple scheme for universal linear-optics quantum computing with constant experimental complexity using fiber loops. *Phys. Rev. A* **91**, 012306 (2015).

[45] Bentivegna, M. *et al.* Experimental scattershot boson sampling. *Science Advances* **1**, 1400255 (2015).

[46] Zhang, C. *et al.* Experimental greenberger-horne-zeilinger-type six-photon quantum non-locality. *Phys. Rev. Lett.* **115**, 260402 (2015).

[47] Loredo, J. C. *et al.* Boson sampling with single-photon fock states from a bright solid-state source. *arXiv:1603.00054* (2016).

[48] Unsleber, S. *et al.* Highly indistinguishable on-demand resonance fluorescence photons from a deterministic quantum dot micropillar device with 75% extraction efficiency. *arXiv:1512.07453v1* (2015).

CHAPTER 5

Boson Sampling with single-photon Fock states from a bright solid-state source

J. C. Loredo[1], M. A. Broome[2], P. Hilaire[3,4], O. Gazzano[3,5], I. Sagnes[3], A. Lemaitre[3],
M. P. Almeida[1], P. Senellart[3,6], A. G. White[1]

[1] Centre for Engineered Quantum Systems, Centre for Quantum Computation and Communication Technology, School of Mathematics and Physics, University of Queensland, Brisbane, Queensland 4072, Australia

[2] Centre of Excellence for Quantum Computation and Communication Technology, School of Physics, University of New South Wales, Sydney, New South Wales 2052, Australia

[3] CNRS-LPN Laboratoire de Photonique et de Nanostructures, Université Paris-Saclay, Route de Nozay, 91460 Marcoussis, France

[4] Université Paris Diderot-Paris 7, 75205 Paris CEDEX 13, France

[5] Joint Quantum Institute, National Institute of Standards and Technology, University of Maryland, Gaithersburg, MD 20899, USA

[6] Département de Physique, Ecole Polytechnique, Université Paris-Saclay, F-91128 Palaiseau, France

A BOSONSAMPLING device is a quantum machine expected to perform tasks intractable for a classical computer, yet requiring minimal non-classical resources as compared to full-scale quantum computers. Photonic implementations to date employed sources based on inefficient processes that only simulate heralded single-photon statistics when strongly reducing emission probabilities. BOSONSAMPLING with only single-photon input has thus never been realised. Here, we report on a BOSONSAMPLING device operated with a bright solid-state source of highly-pure single-photon Fock states: the emission from an efficient and deterministic quantum dot-micropillar system is demultiplexed into three partially-indistinguishable single-photons, with purity $1-g^{(2)}(0)$ of 0.990±0.001, interfering in a 6×6 linear optics network. Our demultiplexed source is between one and two orders-of-magnitude more efficient than current heralded multi-photon sources based on spontaneous parametric downconversion, allowing us to complete the BOSONSAMPLING experiment faster than previous equivalent implementations. This intrinsic source superiority places BOSONSAMPLING with larger photon numbers within near reach.

5.1 Introduction

A core tenet of computer science is the Extended Church-Turing thesis, which states that all computational problems that are efficiently solvable by physically realistic machines are efficiently simulatable with classical resources. In 2011 Aaronson and Arkhipov introduced BosonSampling, a quantum protocol for efficiently sampling the output of a multimode bosonic interferometer [1, 2, 3, 4, 5]: a problem apparently intractable with classical computation. When scaled to many bosons this model of intermediate—i.e. non-universal—quantum computation will provide the strongest evidence against the Extended Church-Turing thesis.

The most experimentally accessible boson is the photon: to date full BosonSampling protocols have been performed using up to 4 photons [6, 7, 8, 9, 10], and protocol validations with up to 6 photons [11]. These initial assays are well short of the numbers of single photons required to probe the Extended Church-Turing thesis: scalable photonic technology is required. The three core technologies needed for scalable quantum photonics are: single-photon sources [12, 13, 14, 15, 16]; large interferometric networks, with current integrated and programmable technology [17, 18, 19, 11]; and efficient photon detection, with demonstrated number resolution [20, 21], and efficiencies of up to 95% [22].

To date, BosonSampling implementations employed photons obtained from spontaneous parametric downconversion, which output is far from ideal single-photon Fock states, $|\psi\rangle = |1\rangle$, instead producing primarily vacuum with a small admixture of pairs of photons:

$$|\psi\rangle = \sqrt{1-|\lambda|^2} \sum_{n=0}^{\infty} \lambda^n |nn\rangle, \tag{5.1}$$

where $|\lambda| \ll 1$. A *non-heralded* $2n$-photon source can be built by using n downconverters, but it can only be used in specific protocols where the impact of higher photon-numbers is minimised [23]; alternatively, it can be operated as a *heralded* n-photon source by detecting n photons—one from each downconverter—to herald the presence of their n single-photon partners. Multi-photon rates for state-of-the-art pulsed downconversion sources [24, 25, 26, 27], pumped at a standard 80 MHz repetition rate, range from ∼300 kHz for 2 photons—thus, yielding heralded single-photons at that rate—down to ∼3 mHz for 8 photons—accordingly, 4 heralded single-photons at that rate. For as little as 6 heralded single-photons, the rate (∼1 per year) becomes less than the detection rate of gravitational waves [28].

Recent progress with time-multiplexing schemes [29] can potentially increase these heralded multi-photon rates in future experiments. Using downconversion to manipulate many single-photons remains, however, challenging to date, which has prevented the scaling of BosonSampling to larger photon numbers. In an effort to lessen this hurdle, an extended version of the protocol—named randomized [4], or "Scattershot" [10], BosonSampling—exploits heralding as a mean to increase, by a binomial factor, the number of valid inputs to the protocol: BosonSampling then becomes scalable with probabilistic, but heralded, downconversion sources.

Quantum-dots in photonic structures [30, 31, 32, 33, 34] have been recently shown to produce

long streams of indistinguishable single-photons with large emission yields [35, 36]. Efficient temporal-to-spatial demultiplexing of these sources will enable multi-photon experiments at scales heretofore impossible. Here we implement a BosonSampling device operated with a bright demultiplexed source of three highly-pure single-photon Fock states from the emission of a deterministic quantum dot-micropillar system [31]. The high source brightness allows us to implement multi-photon sources markedly more efficient than their downconversion counterparts, completing the BosonSampling protocol faster than in previous implementations. Our results prove solid-state sources an appealing candidate to constitute the basis for future quantum photonics, in particular for the implementation of BosonSampling with larger photon numbers.

5.2 Source of multiple single-photon Fock states

Laser pulses with a repetition rate of R_L=80 MHz and wavelength centred at 905 nm provide quasi-resonant excitation of an InGaAs quantum-dot deterministically coupled to a micropillar cavity, which itself is housed in an optically accessible cryostat (Cryo) system at 13 K. See refs. [31, 35] for a detailed description of this quantum dot-micropillar system. An optimised collection efficiency results in a record probability per pump-pulse of finding an spectrally-isolated single-photon at the output of a single-mode fiber—an absolute brightness—of up to η_0=0.14. As a result, our core source generates up to ∼11 MHz of single-photons, modulo detector efficiencies, from which 3.6 MHz are detected with an avalanche photodiode (APD) of 32% quantum efficiency [35]. The absolute brightness depends on the laser pump power P according to $\eta = \eta_0 \left(1 - e^{-P/P_0}\right)$, with P_0=150 μW the saturation power. Under quasi-resonant excitation, single-photon sources based on non-gated quantum dots are subject to small and random frequency jitter—known as spectral diffusion—due to charges near the solid-state emitter [37, 38]. This results in the emission of photons with partial indistinguishability, which in our case is around 50–70% depending on the exact pump conditions [35]. We choose to operate our source at P=1.2P_0, at which point it exhibits a single-photon purity $1-g^{(2)}(0)$ of 0.990±0.001, where $g^{(2)}(0)$=0 holds for an ideal $|n\rangle=|1\rangle$ Fock state. Our source remains highly pure even at high pump powers, with a purity of 0.976 ± 0.001 at $3P_0$, see Appendix. Temporal to spatial demultiplexing of the source could be achieved with an active, temporally-varying, switcher, such that each of n consecutive single-photons is routed into a different spatial channel, resulting in a scalable method to demultiplex n events from a 1-photon source into one event of an n-photon source. A simpler alternative is to implement a passive demultiplexer as depicted in Fig. 5.1(a). Here, photon routing occurs by using an array of $n-1$ chained beamsplitters with tuned transmittances as to evenly distribute, with probability $1/n$, each single-photon into one of n possible outputs. The high absolute brightness in our core source allows us to readily operate 2-, 3-, and 4-photon sources with this method. Figures 5.1(b)-(d) show the detected, and generated—corrected for detector efficiencies—count-rates of our demultiplexed n-photon source: n single-photons in the same temporal mode at the output of n single-mode fibres.
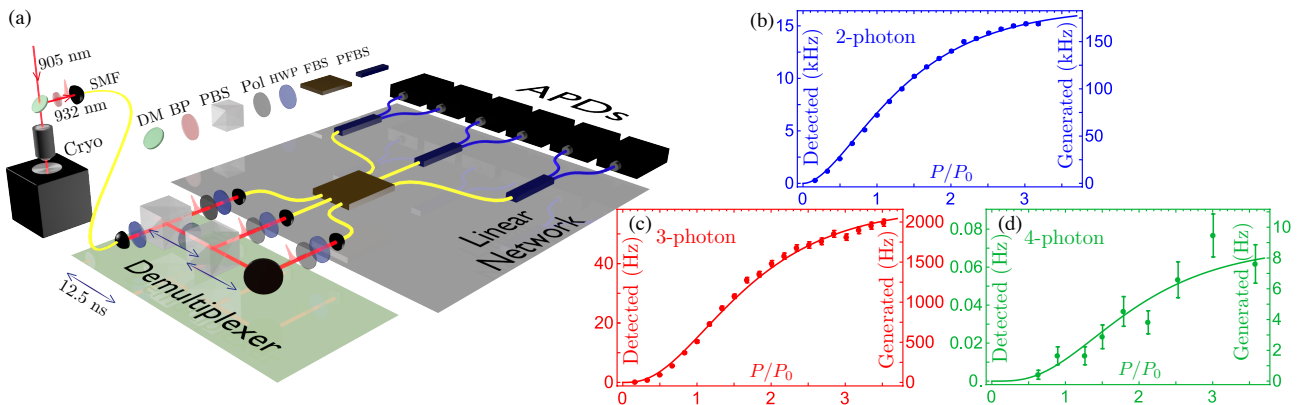
Figure 5.1: Experimental setup. (a) A dichroic mirror (DM), and a 0.85 nm FWHM band-pass filter (BP) isolate single-photon emission at 932 nm from the 905 nm excitation laser, which is then collected by a single-mode fibre (SMF). A passive demultiplexer composed of beam-splitters with tunable transmittances—half-wave plates (HWP), and polarising beam-splitters (PBS)—and compensating delay lines of 12.5 ns probabilistically converts three consecutive single photons into separate spatial modes at the input of the BOSONSAMPLING circuit. The 6×6 linear network is composed of polarisers (Pol), half-wave plates, a 3×3 non-polarising fibre beam-splitter (FBS), and polarising fibre beam-splitters (PFBS). Six APDs are used to record two- and three-fold correlation measurements to sample from the output distribution of the BOSONSAMPLING device. (b)-(d) Detected and generated n-photon rates obtained directly from the demultiplexed source. The generated rates include a factor of $(1/0.3)^n$ to describe our source modulo detector efficiencies (30% in average for the used APDs). The 4-photon count-rates are obtained from the demultiplexer in (a) with an extra tunable beam-splitter. Curves are fits to $c_{\max}^{(n)}(1-e^{-P/P_0})^n$, with $c_{\max}^{(2)}=186.4$ kHz, $c_{\max}^{(3)}=2202$ Hz, and $c_{\max}^{(4)}=8.8$ Hz, denoting maximum n-photon generated rates.

To estimate the efficiency of our source, we define the *n-photon probability per trial*

$$p_{\mathrm{pt}}^{(n)}=c_{\mathrm{gen}}^{(n)}/R_{\mathrm{trial}}, \tag{5.2}$$

the probability of generating a spectrally-isolated n-photon event, at the output of n single-mode fibres, per experimental attempt. Here, $c_{\mathrm{gen}}^{(n)}$ is the n-photon generated rate, and R_{trial} is the "trial" rate. This allows us to compare multi-photon sources from different systems based solely on their efficiency, irrespective of external parameters, such as detector efficiencies, and pump rates. For an explicit comparison, we compute $p_{\mathrm{pt}}^{(n)}$ for various *partially* heralded 3-photon sources used in previous BOSONSAMPLING experiments, see Fig. 5.2. Our solid-state based 3-photon source is superior to its downconversion counterparts by one to two orders-of-magnitude, see Appendix for details on this comparison. Note that this is achieved using a non-scalable—scaling as $1/n^n$—probabilistic demultiplexer. We thus expect our n-photon efficiency to increase super-exponentially ($\propto n^n$) with an active demultiplexer.
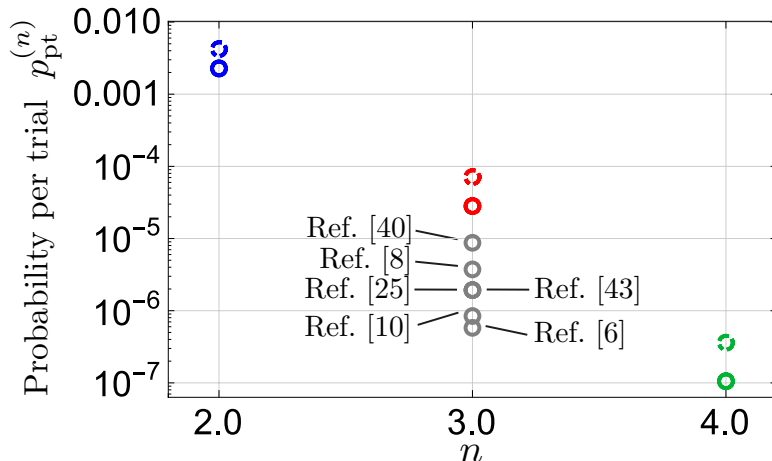
Figure 5.2: Multi-photon source efficiency. n-photon probability per trial, $p_{pt}^{(n)}$, for our 2-, 3-, and 4-photon source taken at $1.2P_0$ (solid circles), and at $3P_0$ (dashed circles). The $p_{pt}^{(n)}$ is estimated for various downconversion 3-photon sources (grey circles) employed in previous BosonSampling experiments. Our 3-photon source is between one to two orders of magnitude more efficient than the downconversion cases. Note that only partial heralding was employed in all downconversion implementations. A fully heralded n-photon source, a necessary condition to produce *true* single-photon Fock state statistics with downconversion, is thus further orders-of-magnitude less efficient than our sources.

5.3 BosonSampling with solid-state photon sources

Using this method, 2 and 3 partially-indistinguishable single-photons are used as inputs into the BosonSampling 6×6 linear network $\mathcal{L}$, consisting of 3 spatial- and 2 polarisation-encoded modes, see Fig. 5.1(a). The relative temporal delay between photons is fine-tuned as to erase their temporal distinguishability, and the use of polarising fibre beam-splitters ensures that they are indistinguishable in polarisation.

We first input $N=2$ single-photons, and characterise the $M=6$-mode $\mathcal{L}$ network—in general a non-unitary transfer matrix due to inevitable optical losses—using the method described in ref. [39], see Appendix. Following the theoretical model developed in ref. [40], 2 photons with a degree of indistinguishability quantified by $\mathcal{I}$, entering $\mathcal{L}$ in inputs $\{i, j\}$ and exiting from outputs $\{k_1, k_2\}$ lead to a 2-fold coincidence probability:

$$p^{(2)} = \left(\frac{1+\mathcal{I}}{2}\right) \left|\text{per}(\overline{\mathcal{L}})\right|^2 + \left(\frac{1-\mathcal{I}}{2}\right) \left|\det(\overline{\mathcal{L}})\right|^2, \tag{5.3}$$

given by the permanent (per) and determinant (det) of the submatrix $\overline{\mathcal{L}}$ formed with rows i, j and columns k_1, k_2 of $\mathcal{L}$. Note that Eq. (5.3) reduces to the well-known formula $p^{(2)} = \left|\text{per}(\overline{\mathcal{L}})\right|^2$ in the ideal case of perfect indistinguishability, i.e. $\mathcal{I}=1$.

We measured all $\binom{M}{N}=15$ outputs in which photons exit $\mathcal{L}$ in different modes, so-called no-collision events. Peak areas in temporal-correlation measurements at these outputs allow us to extract—in a single experimental run—both the sampling distribution resulting from the Boson Sampler—that is, with partially-indistinguishable photons—and that of a (classi-

cal) distinguishable sampler arising from completely distinguishable particles. Given an output configuration k, coincidences detected under the area A_k^0 around zero delay $\Delta t=0$ are subject to two-photon interference: they determine the Boson Sampler distribution by measuring $\overline{p}_k^{(2)}=A_k^0$. Conversely, photons leading to coincidences around $\Delta t= \pm \, l \times (12.5 \text{ ns})$, for l inte-
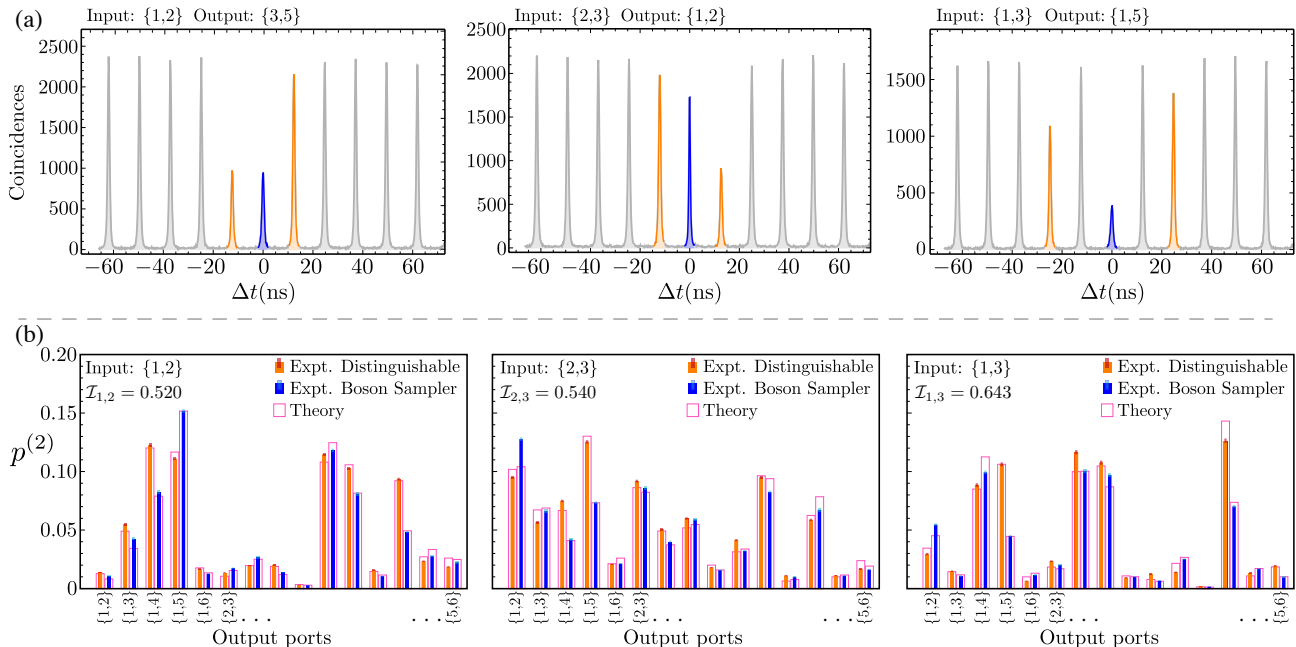
Figure 5.3: Two-photon BosonSampling. (a) Temporal-correlation measurements at no-collision outputs for 2 photons entering at different inputs. Coincidences around $\Delta t=0$ (blue peaks) result from two-photon interference and are thus governed by Eq. (5.3). The position of reduced areas (orange peaks) indicates the temporal distance in emission from the quantum-dot: For inputs $\{1,2\}$, and $\{2,3\}$, photons were emitted after one laser repetition rate $1/R_L=12.5$ ns, thus reduced areas appear at $\pm 1/R_L$; similarly, appearing at ± 25 ns for $\{1,3\}$, with photons emitted separated by 2 laser repetition rates. Coincidences outside $\Delta t=0$ (orange peaks and grey peaks) involve non-interfering photons, thus contain only classical information. (b) Coincidences at zero delay from the 15 no-collision outputs give the distribution of the Boson Sampler (blue bars), with theoretical distributions (empty bars) given by $\mathcal{I}_{1,2}=0.520$, $\mathcal{I}_{2,3}=0.540$, and $\mathcal{I}_{1,3}=0.643$, for their respective input; whereas coincidences outside zero delay determine that of the distinguishable sampler (red bars), with theoretical distribution (empty bars) obtained by assuming zero indistinguishability in Eq. (5.3). Note that strong output configurations in the classical sampler *tend* to have a larger reduction when observed in the Boson Sampler. A complete sampled distribution is obtained with 10 minutes integration time; and, in average, a total of ~ 40000 2-fold events are collected for any given distribution. Error bars (small light-coloured bars) are deduced from assuming poissonian statistics in detected events.

ger, do not interfere, and one would expect that these distributions contain information of a classical sampler. Indeed, following ref. [35], one can deduce that the distinguishable sampler distribution is measured via $\overline{p}_k^{(2)}(0)=2A_k^r-A_k^n-A_k^p$, where A_k^r is a reference area (average in grey peaks), A_k^n is the reduced area at negative Δt (left orange peak), and A_k^p is the reduced area

at positive Δt (right orange peak) as shown in Fig. 5.3(a). Measuring only no-collision events, however, does not provide access to the entire output distribution, thus to obtain probabilities we normalise the measured distributions to the corresponding theoretical prediction according to Eq. (5.3)—that is, the sum of experimentally obtained probabilities within the no-collision subspace is matched to that as in theory; and, given a 2-photon input $\{i, j\}$, $\mathcal{I}_{i,j}$ is extracted from the measured output distribution, see Appendix.

Figure 5.3(b) shows our 2-photon BosonSampling results. Experimental distributions for the Boson Sampler (blue bars) are shown for 3 different 2-photon inputs, and their theoretical distributions (empty bars) are obtained with pair-wise indistinguishabilities $\mathcal{I}_{1,2}$=0.520, $\mathcal{I}_{2,3}$=0.540, and $\mathcal{I}_{1,3}$=0.643, respectively; in agreement with independently measured indistinguishabilities via two-photon interference on a 2×2 beamsplitter, see Appendix. For the distinguishable sampler (red bars), the theoretical distribution (empty bars) is calculated by using $\mathcal{I}_{i,j}$=0, $\forall i, j$ in Eq. (5.3). To quantify the agreement between theory and experiment, we employ the statistical fidelity $\mathcal{F}=\sum_i \sqrt{p_i^{th} p_i^{exp}}$ between normalised theoretical and experimental distributions. For our 2-photon BosonSampling, we find an average fidelity of $\overline{\mathcal{F}}$=0.9984±0.0007 across the six sampled distributions in Fig. 5.3(b), where the error here is one standard deviation among the six fidelity values.

We now tune the source to input N=3 single-photons into the $\{1, 2, 3\}$ mode. In this case, the probability of detecting a 3-fold coincidence at outputs of $\mathcal{L}$ is [40]:

$$p^{(3)} = t_6^\dagger \left(\mathbb{I} + \sum_{i \neq j} \rho_{i,j} \mathcal{I}_{i,j} + \tilde{\rho} \prod_{i \neq j} \sqrt{\mathcal{I}_{i,j}} \right) t_6, \qquad (5.4)$$

with $\mathbb{I}$, the 6×6 identity operator; t_6, a 6-component quantity that depends on the permanent, determinant, and immanants of 3×3 submatrices $\mathcal{T}$; and the $\rho_{i,j}$, and $\tilde{\rho}$ matrices as explicitly defined in the Appendix. Eq. (5.4) reduces to $p^{(3)}= |\text{per}(\mathcal{T})|^2$ in the ideal case of perfect indistinguishability between all particles, i.e. $\mathcal{I}_{i,j}$=1, $\forall i, j$.

Verifying the output distribution of a BosonSampling device involves calculating a number of (modulus squared) matrix permanents. This task is in general computationally hard to implement efficiently on a classical computer. The complete result of a large-scale BosonSampling machine is thus likely to be, even in principal, unverifiable. It has been even argued that a large-scale BosonSampling experiment will fail to distinguish its data from the (trivial) uniform distribution—i.e., one in which every output configuration is equally probable [41]. In light of this, some methods have been proposed and demonstrated for the *validation* of BosonSampling: circumstantial evidence is provided to support that a BosonSampling machine is indeed functioning according to the laws of quantum mechanics, by ruling out that the experimentally obtained data originates from, e.g., the uniform distribution, or a sampler with distinguishable particles [42, 43, 44, 11].

Figure 5.4 shows our experimental results for the 3-photon Boson Sampler. In Fig. 5.4(a), the previously determined 2-photon indistinguishabilities $\mathcal{I}_{i,j}$ are used as input for the theoretical distribution (empty bars) according to Eq. (5.4), and experimental probabilities (blue bars)
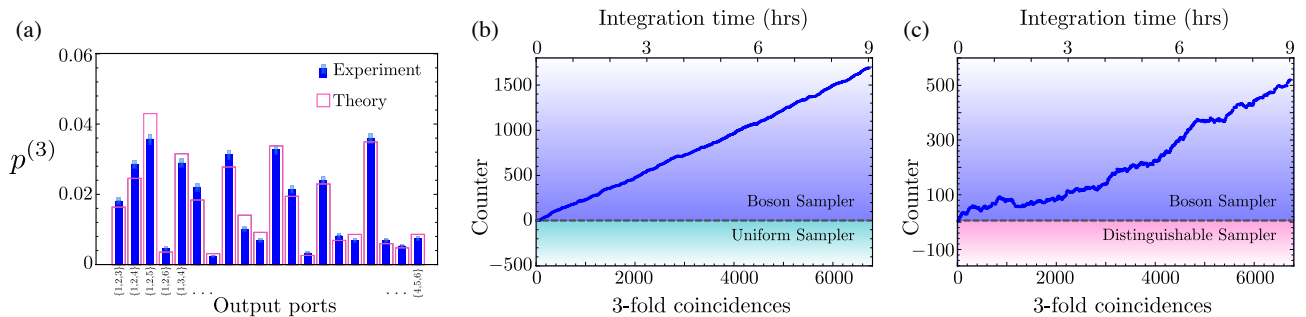
Figure 5.4: Three-photon BOSONSAMPLING. (a) A total of 20 no-collision 3-fold simultaneous coincidences are recorded to obtain the Boson Sampler distribution (blue bars); the theoretical distribution (empty bars) is obtained from Eq. (5.4) and by using the previously determined pair-wise indistinguishability parameters. Error bars (light-coloured bars) are deduced from poissonian statistics in measured events. We apply the validation of BOSONSAMPLING protocol against the uniform sampler (b), and distinguishable sampler (c). A counter (blue dots) is updated for every 3-fold event and at any point a positive value validates the data as being obtained from a Boson Sampler as opposed to either a uniform or distinguishable sampler, see Appendix. The final data set contains a total of 6725 3-fold events collected in 9 hours, that is $\sim$1000 per 80 minutes; a faster rate than in previous BOSONSAMPLING experiments.

are obtained by measuring the $\binom{M}{N}$=20 3-fold simultaneous—i.e. around Δt=0—coincidences for no-collision events normalised to the theoretical prediction. We find the 3-photon BOSON-SAMPLING fidelity $\mathcal{F}$=0.997±0.006, where the error here results from propagated poissonian statistics. In Figs. 5.4(b),(c), we apply the validation of BOSONSAMPLING protocol to our data. We record 3-fold coincidences in steps of 30 seconds, in which time a counter is updated. For each detected 3-fold coincidence, the counter is either increased or decreased in one unit, and it is designed, see Appendix, such that after an experimental run a positive value validates the data as obtained from the Boson Sampler distribution, whereas a negative counter indicates it originates from the uniform sampler, see Fig. 5.4(b), or the distinguishable sampler, see Fig. 5.4(c). We observed overall increasing positive counters, thus validating our BOSONSAMPLING device by ruling out the alternative hypotheses.

5.4 Discussion

We experimentally demonstrated multi-photon interference with a highly-efficient solid-state source: a BOSONSAMPLING device implemented with single-photon Fock states emitted by a deterministic quantum dot-micropillar system. A temporal to spatial demultiplexing scheme resulted in multi-photon sources between one to two orders-of-magnitude more efficient than their downconversion versions, which allowed us to complete the BOSONSAMPLING protocol faster than in previous experiments [6, 7, 8, 9]. An active source demultiplexing would further boost our multi-photon efficiency super-exponentially—with the number of photons—potentially enabling BOSONSAMPLING with larger photon numbers.

Furthermore, we directly observed the effect of partial distinguishability: Our results follow closely the sampling of permanents and immanants of matrices with contributions modulated by photon indistinguishability. Moreover, by exploiting temporal-correlation measurements we showed that both classical and quantum 2-photon sampling distributions can be obtained simultaneously, which can be readily extended to multi-fold temporal-dependent measurements in a larger BosonSampling experiment. Potentially, this could motivate new validation protocols exploiting statistics that include this temporal degree of freedom.

The impact of partial distinguishability in BosonSampling has been studied theoretically [45, 46, 40, 47], and reported experimentally [40]. However, identifying experimentally this property in isolation is challenging. Previous experiments with downconversion exhibit photon-statistics polluted by higher-order terms [23], which can be mistakenly interpreted as decreased photon-indistinguishability. In fact, in many cases these higher-order terms, and not photon distinguishability, are the main cause of performance degradation in downconversion-based protocols [48, 49]. The pathway to maximise indistinguishability in efficient solid-state sources is well known: resonant excitation of the quantum-dot results in near-optimal values of photon indistinguishability [33, 34], in which case the obtained output distributions will be close to the sampling of only permanents—functions belonging to the #P complexity class, in which the main complexity arguments of BosonSampling apply.

We believe our results pave the way to the forthcoming advent of quantum-dot based quantum photonics, in which a future BosonSampling implementation with efficiently demultiplexed and resonantly-pumped solid-state sources may finally see the Extended Church-Turing thesis put to serious test.

5.5 Appendix

5.5.1 Single-photon purity

Figure 5.5 shows the single-photon purity of our source from autocorrelation measurements at 1.2, and 3 times the saturation power P_0.
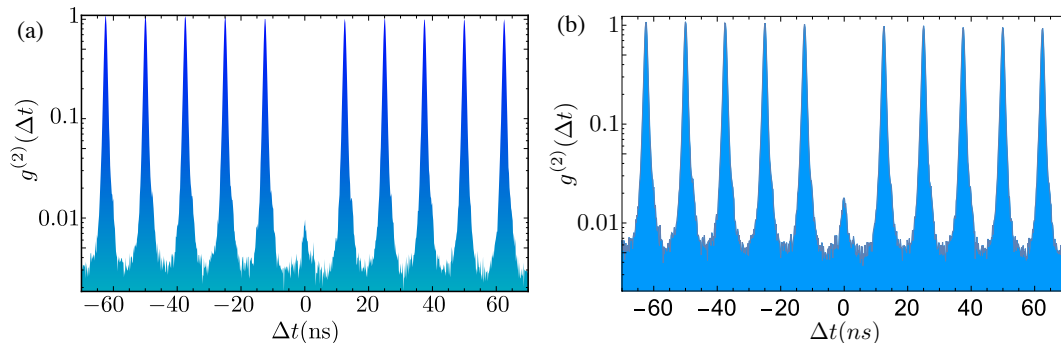
Figure 5.5: Second-order autocorrelation function $g^{(2)}(\Delta t)$ (log scale). A Hanbury Brown and Twiss experiment results in coincidences every $1/R_L=12.5$ ns. Decreased detected events—antibunching—at $\Delta t=0$ indicates non-classical states of light, where an ideal single-photon Fock state exhibits $g^{(2)}(0)=0$. We measure (a) $g^{(2)}(0)=0.010 \pm 0.001$ at $P=1.2P_0$, and (b) $g^{(2)}(0)=0.024 \pm 0.001$ at $P=3P_0$, resulting in single-photon purities $1-g^{(2)}(0)$ of 0.990 ± 0.001 and 0.976 ± 0.001, respectively.

5.5.2 n-photon probability per trial

In the main text, the *n-photon probability per trial*, $p_{\mathrm{pt}}^{(n)}$, is defined as the probability of generating a spectrally-isolated n-photon event, at the output of n single-mode fibres, per experimental attempt. Here, we expand on this concept, and elaborate on what we consider as a "trial", or "experimental attempt".

First, a relevant concept of n-photon efficiency is that taken at a point in which the source is readily useful, for which reason we consider n-photon events after all spectral filtering needed to perform the experiment; at the output of single-mode fibres as to straightforwardly interconnect it with a given protocol setup; and only the probability of *generating* the event—corrected for detector efficiencies—is considered to be insensitive to different detector performances at different operating wavelengths.

Secondly, different sources—either from the same, or from different systems—involve distinct experimental attempts to generate them. For instance, a 3-photon source can be obtained from: 1) A second-order downconversion event generated from 1 single laser pulse, this generates two pairs of photons, one of which is used to partially herald the source. 2) First-order downconversion events from 2 laser pulses in a double-pass pump configuration, which generates one pair in the forward direction, one pair in the backward direction, and one of the four photons is used to partially herald the source.

Ref.	$c_{\text{det}}^{(3)}$ (Hz)	η_{d}	R_{trial}(Hz)	$p_{\text{pt}}^{(3)}$
This Work ($3P_0$)	51	$(0.3)^3$	2.7×10^7	7.1×10^{-5}
This Work ($1.2P_0$)	20	$(0.3)^3$	2.7×10^7	2.8×10^{-5}
[40]	91	$(0.6)^4$	8×10^7	8.7×10^{-6}
[8]	39	$(0.6)^4$	8×10^7	3.7×10^{-6}
[25]	20	$(0.6)^4$	8×10^7	1.9×10^{-6}
[43]	20	$(0.6)^4$	8×10^7	1.9×10^{-6}
[10]	9	$(0.6)^4$	8×10^7	8.4×10^{-7}
[6]	6	$(0.6)^4$	8×10^7	5.8×10^{-7}

Table 5.1: **3-photon source efficiency.** Parameters used in estimating $p_{\text{pt}}^{(3)}$. For our work, we measured an average detector efficiency of 0.3, and three detectors were used. For the other references, we assumed a detector efficiency of 0.6, the expected value at downconversion wavelengths, and four detectors (three plus heralding) were used.

3) Consecutive single-photon emission from a quantum dot generated after 3 laser pulses, as it is the case in our experiment.

In the above examples, distinct approaches will lead to a different amount of attempts per unit of time to generate a 3-photon event. Assuming a pulsed laser with a standard 80 MHz repetition rate: For 1), we attempt to produce the source 8×10^7 times a second. For 2), although twice the number of pulses per second are sent into a non-linear crystal, we still attempt 8×10^7 times a second to generate the source. In 3), one needs 3 pulses to generate the state, thus the number of attempts per second is reduced to $\sim 2.7\times10^7$.

Taken this into account, we can calculate $p_{\text{pt}}^{(n)}$:

$$p_{\text{pt}}^{(n)} = \frac{c_{\text{gen}}^{(n)}}{R_{\text{trial}}} = \frac{c_{\text{det}}^{(n)}}{\eta_{\text{d}}R_{\text{trial}}}, \tag{5.5}$$

where $c_{\text{det}}^{(n)}$ ($c_{\text{gen}}^{(n)}$) is the detected (generated) n-photon rate; n_{d} is the total efficiency accounting for all detectors employed, e.g., a non-heralded downconversion n-photon source uses n detectors, whereas a fully heralded one uses $2n$; and R_{trial} is the rate of trials.

Table 5.1 summarizes the specific values employed to calculate the 3-photon $p_{\text{pt}}^{(3)}$, which was used in the comparison between our source and those used in previous BosonSampling experiments with downconversion. The detected rates $c_{\text{det}}^{(3)}$ used in refs. [40, 8] were obtained via private communication, and rates of 90.5 Hz, and 38.7 Hz were provided. For refs [25, 43], the 20 Hz 4-photon rates (3-photon plus heralding) were obtained from the manuscripts. For ref. [10], 35 kHz, and 20 kHz 2-photon rates are reported in the Supplementary Materials, from where a 4-photon rate (3-photon plus heralding) of 35 kHz $*$ 20 kHz/(80 MHz) = 8.75 Hz is derived. For ref. [6], a detected 4-photon rate of 1.2 kHz is reported at 100% pump power, which after spectral filtering of 3 photons (measured filter transmission of 0.5), and 20% pump power operation, is reduced to a 4-photon rate (3-photon plus heralding) of 6 Hz. The values reported for our sources are extracted from the power dependent n-photon saturation curves, and we employed the parameters $\eta_{\text{d}}=(0.3)^n$, and $R_{\text{trial}}=8\times10^7/n$ Hz for estimating $p_{\text{pt}}^{(n)}$.

5.5.3 Expected rates

The expected n-photon count-rate is:

$$c^{(n)} = \left(\eta_0 \left(1 - e^{-P/P_0} \right) \eta_{\text{setup}} \right)^n \left(\frac{1}{n} \right)^n R_L, \qquad (5.6)$$

where η_0=0.14 is the measured maximum absolute brightness, $\eta_0 \left(1 - e^{-P/P_0} \right)$ is the absolute brightness at a given relative pump power P/P_0, η_{setup} accounts for the experimental setup transmission and detection efficiencies, the factor $(1/n)^n$ is due to the probabilistic nature of the demultiplexer, and R_L is the laser's repetition rate.

We operate our source at R_L=80 MHz. The measured optical transmission of our demultiplexer is η_{demux}=0.650, arising from 3 polarizing beam-splitters, 15 AR-coated mirrors, and single-mode fibre couplers; which together with an average detector efficiency of η_{det}=0.30 results in a setup efficiency of η_{setup}=$\eta_{\text{demux}}\eta_{\text{det}}$=0.195. At P/P_0=3, these parameters predict, according to Eq. (5.6), detecting count-rates of $c^{(2)}$=13.5 kHz, $c^{(3)}$=52 Hz, and $c^{(4)}$=0.14 Hz, in good agreement with the actual detected count-rates $c_{\text{det}}^{(2)}$=15.1 kHz, $c_{\text{det}}^{(3)}$=51 Hz, and a discrepancy to the measured $c_{\text{det}}^{(4)}$=0.06 Hz can be attributed to a relatively large measurement error, see Fig. 5.1 of the main text.

Our BosonSampling setup contains a free-space preparation stage with η_{prep}=0.723, an average coupling into single-modes of a 3×3 fibre beam-splitter of η_{fc}=0.877, transmission of such fibre beam-splitter of η_{fbs}=0.678, and an average transmission of polarizing fibre beam-splitter of η_{pfbs}=0.767. This results in a combined BosonSampling setup efficiency of $\eta_{\text{setup}}^{\text{BS}}$=$\eta_{\text{demux}}\eta_{\text{prep}}\eta_{\text{fc}}\eta_{\text{fbs}}\eta_{\text{pfbs}}\eta_{\text{det}}$=0.064; which at P/P_0=1.2, according to Eq. (5.6), predicts $c^{(3)}$=0.73 Hz, the total 3-fold count-rate that we would expect with completely distinguishable particles fed into the BosonSampling experiment. This is consistent with our measured total 3-fold count-rate of 0.21 Hz (6725 3-fold events collected in 9 hours) in an experiment performed with partially-indistinguishable particles.

5.5.4 Transfer matrix

The linear network is composed by a 3×3 fibre beam-splitter, defining 3 spatial modes; and 3 polarizing fibre beam-splitters, giving access to 2 polarization-encoded modes; which combined result in a 6×6 network. Stress applied on these fibres before the experiment tunes a network $\mathcal{L}$ to an unknown configuration, which is then characterized with the method introduced in ref. [39]. This method consists of measuring: the probability $|\mathcal{L}_{i,j}|^2$ of a photon entering $\mathcal{L}$ in input i and exiting in output j, and phase factors $\arg(\mathcal{L}_{i,j})$ obtained from classical interference patterns. These measurements allow to reconstruct the complex elements $\mathcal{L}_{i,j}$. For all measurements presented in the main text, inputs 1, 2, and 3 of $\mathcal{L}$ are used. The transfer matrix $\mathcal{L}$

in this subspace is given by:

$$\mathcal{L}=\begin{bmatrix} 0.314 & 0.160 & 0.251 & 0.578 & 0.576 & 0.188 \\ 0.561 & -0.157+0.151i & -0.319+0.440i & -0.388-0.033i & 0.331-0.127i & -0.120-0.226i \\ 0.473 & 0.352+0.409i & -0.054-0.025i & 0.249-0.206i & -0.559+0.112i & 0.085-0.118i \end{bmatrix}.$$
(5.7)

Measurement errors arise primarily from obtaining $|\mathcal{L}_{i,j}|^2$, due to power instabilities of the laser light used for the characterization. The *relative* errors in these measurements are all <0.01, with an average value of 0.007.

5.5.5   Pair-wise indistinguishability

In a BOSONSAMPLING experiment, the main parameters changing the output distribution are particle distinguishability—originating from either spectral, spatial, or temporal mismatch—and higher-order photon terms. The high single-photon purity of our source, as shown in Fig. 5.5, evidences that higher-order terms have a negligible impact. The major parameter that modulates the output of our experiment is thus the pair-wise photon indistinguishability $\mathcal{I}_{i,j}$ between photons at inputs $\{i,j\}$.

We can obtain an independent estimate of this by comparing experiment to a theoretical model, where $\mathcal{I}_{i,j}$ is allowed to vary, and then minimize their variation distance $d=1/2\sum_k \left| p_k^{(2),\exp} - p_k^{(2),\mathrm{th}} \right|$ between experimental and theoretical distributions. As described in the main text, $p^{(2),\exp}$ is normalised to $\sum_k p_k^{(2),\mathrm{th}}$. This being relevant when computing d as distributions for different degrees of indistinguishability have different normalisation factors. For a given 2-photon input $\{i,j\}$, $\mathcal{I}_{i,j}$ is taken as that at the global minimum in d. We obtain $\mathcal{I}_{1,2}=0.520$, $\mathcal{I}_{2,3}=0.540$, and $\mathcal{I}_{1,3}=0.643$, see Fig. 5.6.
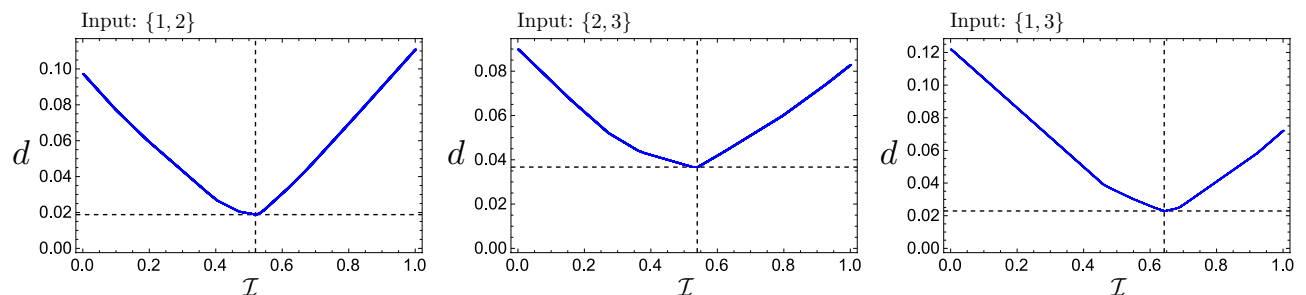
Figure 5.6: Variation distance d between experimental and theoretical distributions. d is a global minimum at $\mathcal{I}_{1,2}=0.520$, $\mathcal{I}_{2,3}=0.540$, and $\mathcal{I}_{1,3}=0.643$ for its corresponding 2-photon input. The variation distances at these points are respectively $d_{1,2}=0.019$, $d_{2,3}=0.037$, and $d_{1,3}=0.023$. These values are obtained with both experimental and theoretical distributions normalised to the non-unity theoretical normalisation factor. When the distributions are normalised to unity, the variation distances are $d_{1,2}=0.028$, $d_{2,3}=0.049$, and $d_{1,3}=0.055$, respectively.

We carried out time-correlated measurements of two-photon interference on a 2×2 beam-splitter to independently verify these degrees of indistinguishability. It has been shown in ref. [35] that the indistinguishability of two photons emitted by a semiconductor quantum dot depends on their emission temporal distance Δt_e. When both photons are emitted with the same polarisation from the quantum dot, their indistinguishability decreases monotonically in Δt_e. In our case we obtain $\mathcal{I}_{12.5\mathrm{ns}}^{bs}=0.6360\pm0.0063$

for photons emitted with Δt_e=12.5 ns, and $\mathcal{I}^{bs}_{25ns}$=0.6252±0.0065 for Δt_e=25 ns, see Fig. 5.7. Note that for these measurements photons are emitted with the same polarisation from the quantum dot.

The amount of indistinguishability $\mathcal{I}_{1,3}$=0.643, involving photons emitted with Δt_e=25 ns, and $\mathcal{I}^{bs}_{25ns}$=0.6252±0.0065 are in good agreement. Both $\mathcal{I}_{1,2}$=0.520, and $\mathcal{I}_{2,3}$=0.540 involve photons emitted with Δt_e=12.5 ns, therefore the minimisation method finds similar values, these however present some discrepancy with $\mathcal{I}^{bs}_{12.5ns}$=0.6360±0.0063. The quantum dot presents a small fine structure splitting of the exciton line, which in turn reduces the indistinguishability of photons emitted from two orthogonal emissions. Inputs $\{1,2\}$, and $\{2,3\}$ in the BosonSampling experiment contain photons separated by the first polarising beam-splitter in the source demultiplexer (see main text), thus they are emitted with orthogonal polarisations from the quantum dot and exhibit a reduced value of indistinguishability compared to photons emitted with the same polarisation, consistent with the obtained values.
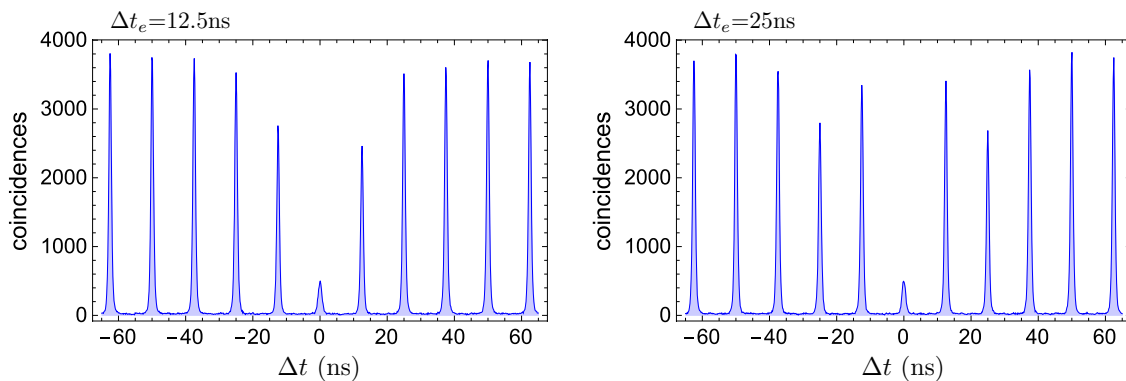
Figure 5.7: Two-photon interference on a 2×2 beam-splitter. Temporal-correlation measurements result in a series of peaks from which the degree of indistinguishability can be directly extracted via $\mathcal{I}=(R^2+T^2-A_0/A)/(2RT)$, with R=0.471 the beam-splitter reflectance, $T=1-R$, A the average peak area outside Δt=0 (excluding reduced peaks at Δt_e), and A_0 the peak area around Δt=0. See ref. [35] for a derivation of this formula. We obtain $\mathcal{I}^{bs}_{12.5ns}$=0.6360±0.0063 for Δt_e=12.5 ns, and $\mathcal{I}^{bs}_{25ns}$=0.6252±0.0065 for Δt_e=25 ns. Errors are estimated from propagated poissonian statistics.

5.5.6 Three-photon interference

We employ the theoretical model introduced in ref. [40] to describe the interference of 3 photons, labeled 1, 2, and 3, scattered across a linear network $\mathcal{L}$. In such case, the probability of detecting a 3-fold coincidence at the output $\{o_1, o_2, o_3\}$ of $\mathcal{L}$ is:

$$p^{(3)} = t_6^{\dagger} \left(\mathbb{I} + \rho_{1,2}\mathcal{I}_{1,2} + \rho_{2,3}\mathcal{I}_{2,3} + \rho_{1,3}\mathcal{I}_{1,3} + \tilde{\rho}\sqrt{\mathcal{I}_{1,2}}\sqrt{\mathcal{I}_{2,3}}\sqrt{\mathcal{I}_{1,3}} \right) t_6; \qquad (5.8)$$

where

$$
t_6 = \begin{pmatrix}
\frac{1}{\sqrt{6}}\mathrm{per}(\mathcal{T}) \\
\frac{1}{\sqrt{6}}\det(\mathcal{T}) \\
\frac{1}{2\sqrt{3}}\mathrm{imm}(\mathcal{T}) + \frac{1}{2\sqrt{3}}\mathrm{imm}(\mathcal{T}_{213}) \\
\frac{1}{6}\mathrm{imm}(\mathcal{T}) - \frac{1}{3}\mathrm{imm}(\mathcal{T}_{132}) - \frac{1}{6}\mathrm{imm}(\mathcal{T}_{213}) + \frac{1}{3}\mathrm{imm}(\mathcal{T}_{312}) \\
\frac{1}{6}\mathrm{imm}(\mathcal{T}) + \frac{1}{3}\mathrm{imm}(\mathcal{T}_{132}) + \frac{1}{6}\mathrm{imm}(\mathcal{T}_{213}) + \frac{1}{3}\mathrm{imm}(\mathcal{T}_{312}) \\
-\frac{1}{2\sqrt{3}}\mathrm{imm}(\mathcal{T}) + \frac{1}{2\sqrt{3}}\mathrm{imm}(\mathcal{T}_{213})
\end{pmatrix}, \quad
\mathbb{I} = \begin{pmatrix}
1 & 0 & 0 & 0 & 0 & 0 \\
0 & 1 & 0 & 0 & 0 & 0 \\
0 & 0 & 1 & 0 & 0 & 0 \\
0 & 0 & 0 & 1 & 0 & 0 \\
0 & 0 & 0 & 0 & 1 & 0 \\
0 & 0 & 0 & 0 & 0 & 1
\end{pmatrix},
$$

$$
\rho_{1,2} = \begin{pmatrix}
1 & 0 & 0 & 0 & 0 & 0 \\
0 & -1 & 0 & 0 & 0 & 0 \\
0 & 0 & 1 & 0 & 0 & 0 \\
0 & 0 & 0 & -1 & 0 & 0 \\
0 & 0 & 0 & 0 & 1 & 0 \\
0 & 0 & 0 & 0 & 0 & -1
\end{pmatrix}, \quad
\rho_{2,3} = \begin{pmatrix}
1 & 0 & 0 & 0 & 0 & 0 \\
0 & -1 & 0 & 0 & 0 & 0 \\
0 & 0 & -\frac{1}{2} & -\frac{\sqrt{3}}{2} & 0 & 0 \\
0 & 0 & -\frac{\sqrt{3}}{2} & \frac{1}{2} & 0 & 0 \\
0 & 0 & 0 & 0 & -\frac{1}{2} & -\frac{\sqrt{3}}{2} \\
0 & 0 & 0 & 0 & -\frac{\sqrt{3}}{2} & \frac{1}{2}
\end{pmatrix},
$$

$$
\rho_{1,3} = \begin{pmatrix}
1 & 0 & 0 & 0 & 0 & 0 \\
0 & -1 & 0 & 0 & 0 & 0 \\
0 & 0 & -\frac{1}{2} & \frac{\sqrt{3}}{2} & 0 & 0 \\
0 & 0 & \frac{\sqrt{3}}{2} & \frac{1}{2} & 0 & 0 \\
0 & 0 & 0 & 0 & -\frac{1}{2} & \frac{\sqrt{3}}{2} \\
0 & 0 & 0 & 0 & \frac{\sqrt{3}}{2} & \frac{1}{2}
\end{pmatrix}, \quad
\tilde{\rho} = \begin{pmatrix}
2 & 0 & 0 & 0 & 0 & 0 \\
0 & 2 & 0 & 0 & 0 & 0 \\
0 & 0 & -1 & 0 & 0 & 0 \\
0 & 0 & 0 & -1 & 0 & 0 \\
0 & 0 & 0 & 0 & -1 & 0 \\
0 & 0 & 0 & 0 & 0 & -1
\end{pmatrix},
$$

$\mathcal{I}_{1,2}$, $\mathcal{I}_{2,3}$, and $\mathcal{I}_{1,3}$ are pair-wise indistinguishability values; $\mathcal{T}$ is a 3×3 submatrix built with rows 1, 2, and 3, and columns o_1, o_2, and o_3 of $\mathcal{L}$; $\mathcal{T}_{a,b,c}$ is the matrix $\mathcal{T}$ with rows 1, 2, and 3 rearranged in order o_1, o_2, and o_3; and the permanent (per), determinant (det), and immanant (imm) of a 3×3 matrix are defined as:

$$
\mathrm{per}\begin{pmatrix} a & b & c \\ d & e & f \\ g & h & i \end{pmatrix} = aei + bfg + cdh + ceg + bdi + afh,
$$

$$
\det\begin{pmatrix} a & b & c \\ d & e & f \\ g & h & i \end{pmatrix} = aei + bfg + cdh - ceg - bdi - afh,
$$

$$
\mathrm{imm}\begin{pmatrix} a & b & c \\ d & e & f \\ g & h & i \end{pmatrix} = 2aei - bfg - cdh.
$$

5.5.7 Validation of BosonSampling

Aaronson and Arkhipov proposed a protocol to test data against the uniform sampler [42], as a counterargument to the claim [41] that a large-scale BosonSampling implementation would fail to distinguish the experimental data even from that of the trivial one. The method—used in Fig. 5.4(b)

in the main text—exploits available information of the sampling device—the transfer matrix $\mathcal{L}$—to define an estimator $P_{\text{est}} = \prod_{i=1}^{n} \sum_{j=1}^{n} \left| \overline{\mathcal{L}}_{i,j} \right|^2$, with $\overline{\mathcal{L}}_{i,j}$ the $n \times n$ submatrix of the $m \times m$ transfer matrix in an experiment involving n bosons in m modes. Unlike the permanent, P_{est} is efficiently computable—thus, the protocol is scalable—and yet is correlated with the Boson Sampler probabilities. For the uniform distribution, the probability of one photon entering $\mathcal{L}$ in input i and exiting in output j is a constant (uniform) value $\left| \overline{\mathcal{L}}_{i,j} \right|^2 = 1/m$ across any input/output setting, thus the estimator takes the form $P_{\text{est}}^{\text{u}} = (n/m)^n$. If the sampling device is functioning correctly, one expects to observe more probable events more often; thus the method simply consists of computing P_{est} for every event observed, and keeping track of a counter that is increased in one unit if $P_{\text{est}} > P_{\text{est}}^{\text{u}}$, and decreased in one unit otherwise. A resulting positive counter then validates the BosonSampling experiment by rejecting the hypothesis that the data originates from the uniform sampler. Experimental evidence supporting that this method works, even with small data samples and experimental imperfections, was reported in refs. [43, 44].

A different protocol, used in Fig. 5.4(c) in the main text, to test the data against a distinguishable sampler was proposed and demonstrated by Spagnolo et. al. [43]. This method, based on the likelihood ratio test, computes the relative—i.e., normalised to the no-collision space—quantum and classical probabilities, p^Q and p^C, for every observed output event; a counter is increased in one unit if $p^Q > p^C$, and decreased in one unit otherwise. At the end of an experimental run a positive counter validates a correct functioning of the BosonSampling machine by rejecting the distinguishable sampler hypothesis.

References

[1] Aaronson, S. & Arkhipov, A. The computational complexity of linear optics. *Proc. ACM Symposium on Theory of Computing, San Jose, CA* 333–342 (2011).

[2] Aaronson, S. A linear-optical proof that the permanent is #P-hard. *Proceedings of the Royal Society A: Mathematical, Physical and Engineering Science* **467**, 3393–3405 (2011).

[3] Shen, C., Zhang, Z. & Duan, L.-M. Scalable implementation of boson sampling with trapped ions. *Phys. Rev. Lett.* **112**, 050504 (2014).

[4] Lund, A. P. *et al.* Boson sampling from a gaussian state. *Phys. Rev. Lett.* **113**, 100502 (2014).

[5] Huh, J., Guerreschi, G. G., Peropadre, B., McClean, J. R. & Aspuru-Guzik, A. Boson sampling for molecular vibronic spectra. *Nat Photon* **9**, 615–620 (2015).

[6] Broome, M. A. *et al.* Photonic boson sampling in a tunable circuit. *Science* **339**, 794–798 (2013).

[7] Spring, J. B. *et al.* Boson sampling on a photonic chip. *Science* **339**, 798–801 (2013). `http://science.sciencemag.org/content/339/6121/798.full.pdf`.

[8] Tillmann, M. *et al.* Experimental boson sampling. *Nat Photon* **7**, 540–544 (2013).

[9] Crespi, A. *et al.* Integrated multimode interferometers with arbitrary designs for photonic boson sampling. *Nat Photon* **7**, 545–549 (2013).

[10] Bentivegna, M. *et al.* Experimental scattershot boson sampling. *Science Advances* **1**, e1400255 (2015). `http://advances.sciencemag.org/content/1/3/e1400255.full.pdf`.

[11] Carolan, J. *et al.* Universal linear optics. *Science* **349**, 711–716 (2015). `http://science.sciencemag.org/content/349/6249/711.full.pdf`.

[12] Kwiat, P. G., Waks, E., White, A. G., Appelbaum, I. & Eberhard, P. H. Ultrabright source of polarization-entangled photons. *Phys. Rev. A* **60**, 773–776 (1999).

[13] Pittman, T., Jacobs, B. & Franson, J. Heralding single photons from pulsed parametric down-conversion. *Optics communications* **246**, 545–550 (2005).

[14] Babinec, T. M. *et al.* A diamond nanowire single-photon source. *Nature nanotechnology* **5**, 195–199 (2010).

[15] Yuan, Z. *et al.* Electrically driven single-photon source. *Science* **295**, 102–105 (2002).

[16] Santori, C., Fattal, D., Vučković, J., Solomon, G. S. & Yamamoto, Y. Indistinguishable photons from a single-photon device. *Nature* **419**, 594–597 (2002).

[17] Politi, A., Cryan, M. J., Rarity, J. G., Yu, S. & O'Brien, J. L. Silica-on-silicon waveguide quantum circuits. *Science* **320**, 646–649 (2008). `http://science.sciencemag.org/content/320/5876/646.full.pdf`.

[18] Smith, B. J., Kundys, D., Thomas-Peter, N., Smith, P. G. R. & Walmsley, I. A. Phase-controlled integrated photonic quantum circuits. *Opt. Express* **17**, 13516–13525 (2009).

[19] Crespi, A. *et al.* Integrated photonic quantum gates for polarization qubits. *Nat Commun* **2**, 566 (2011).

[20] Miller, A. J., Nam, S. W., Martinis, J. M. & Sergienko, A. V. Demonstration of a low-noise near-infrared photon counter with multiphoton discrimination. *Applied Physics Letters* **83**, 791–793 (2003).

[21] Divochiy, A. *et al.* Superconducting nanowire photon-number-resolving detector at telecommunication wavelengths. *Nature Photonics* **2**, 302–306 (2008).

[22] Lita, A. E., Miller, A. J. & Nam, S. W. Counting near-infrared single-photons with 95% efficiency. *Opt. Express* **16**, 3032–3040 (2008).

[23] Pan, J.-W. *et al.* Multiphoton entanglement and interferometry. *Rev. Mod. Phys.* **84**, 777–838 (2012).

[24] Yao, X.-C. *et al.* Observation of eight-photon entanglement. *Nat Photon* **6**, 225–228 (2012).

[25] Metcalf, B. J. *et al.* Multiphoton quantum interference in a multiport integrated photonic device. *Nat Commun* **4**, 1356 (2013).

[26] Zhang, C. *et al.* Experimental greenberger-horne-zeilinger-type six-photon quantum nonlocality. *Phys. Rev. Lett.* **115**, 260402 (2015).

[27] Loredo, J. C. *et al.* Measuring entanglement in a photonic embedding quantum simulator. *Phys. Rev. Lett.* **116**, 070503 (2016).

[28] Abbott, B. P. *et al.* Observation of gravitational waves from a binary black hole merger. *Phys. Rev. Lett.* **116**, 061102 (2016).

[29] Kaneda, F. *et al.* Time-multiplexed heralded single-photon source. *Optica* **2**, 1010–1013 (2015).

[30] Lodahl, P. *et al.* Controlling the dynamics of spontaneous emission from quantum dots by photonic crystals. *Nature* **430**, 654–657 (2004).

[31] Gazzano, O. *et al.* Bright solid-state sources of indistinguishable single photons. *Nature communications* **4**, 1425 (2013).

[32] Lodahl, P., Mahmoodian, S. & Stobbe, S. Interfacing single photons and single quantum dots with photonic nanostructures. *Rev. Mod. Phys.* **87**, 347–400 (2015).

[33] Ding, X. *et al.* On-demand single photons with high extraction efficiency and near-unity indistinguishability from a resonantly driven quantum dot in a micropillar. *Phys. Rev. Lett.* **116**, 020401 (2016).

[34] Somaschi, N. *et al.* Near-optimal single-photon sources in the solid state. *Nat Photon* **10**, 340–345 (2016).

[35] Loredo, J. C. *et al.* Scalable performance in solid-state single-photon sources. *Optica* **3**, 433–440 (2016).

[36] Wang, H. *et al.* Near-transform-limited single photons from an efficient solid-state quantum emitter. *Phys. Rev. Lett.* **116**, 213601 (2016).

[37] Kuhlmann, A. V. *et al.* Charge noise and spin noise in a semiconductor quantum device. *Nat Phys* **9**, 570–575 (2013).

[38] Unsleber, S. *et al.* Two-photon interference from a quantum dot microcavity: Persistent pure dephasing and suppression of time jitter. *Phys. Rev. B* **91**, 075413 (2015).

[39] Rahimi-Keshari, S. *et al.* Direct characterization of linear-optical networks. *Opt. Express* **21**, 13450–13458 (2013).

[40] Tillmann, M. *et al.* Generalized multiphoton quantum interference. *Phys. Rev. X* **5**, 041015 (2015).

[41] Gogolin, C., Kliesch, M., Aolita, L. & Eisert, J. Boson sampling in the light of sample complexity. *arXiv:1306.3995* (2013).

[42] Aaronson, S. & Arkhipov, A. Bosonsampling is far from uniform. *arXiv:1309.7460* (2013).

[43] Spagnolo, N. *et al.* Experimental validation of photonic boson sampling. *Nat Photon* **8**, 615–620 (2014).

[44] Carolan, J. *et al.* On the experimental verification of quantum complexity in linear optics. *Nat Photon* **8**, 621–626 (2014).

[45] Shchesnovich, V. S. Partial indistinguishability theory for multiphoton experiments in multiport devices. *Phys. Rev. A* **91**, 013844 (2015).

[46] Tichy, M. C. Sampling of partially distinguishable bosons and the relation to the multidimensional permanent. *Phys. Rev. A* **91**, 022316 (2015).

[47] Tamma, V. & Laibacher, S. Multiboson correlation interferometry with arbitrary single-photon pure states. *Phys. Rev. Lett.* **114**, 243601 (2015).

[48] Weinhold, T. J. *et al.* Understanding photonic quantum-logic gates: The road to fault tolerance. *arXiv:0808.0794* (2008).

[49] Barbieri, M. *et al.* Parametric downconversion and optical quantum gates: two's company, four's a crowd. *Journal of Modern Optics* **56**, 209–214 (2009).

CHAPTER 6

Discussion and Conclusion

PHOTONIC quantum technologies [1] rely on the ability of controllably manipulating quanta of light. In the interplay of a large number of single-photons, the appearance of nonclassical correlations between the particles' degrees-of-freedom allows for the implementation of (quantum) protocols and algorithms that are markedly more efficient in performing certain tasks than their classical counterparts [2]. For instance, for the factorisation of large integers—in particular, semiprime numbers—it is believed that no efficient classical algorithm exists, the most efficient known algorithm requiring a sub-exponential time[1], whereas a quantum algorithm—Shor's algorithm [3]—is known to solve the integer factorisation problem in polynomial time. Moreover, a scalable quantum computer can in-principle be built entirely using single-photons, detectors, and linear optical networks [4], with computational power growing exponentially with the number of single-photons being handled. However, even quantifying to what extent these particles are quantum-mechanically correlated is a hard problem on its own, as usually an exponentially growing number of measurements are required in the full reconstruction of multi-photon states [5]. Furthermore, generating a large number of these single-photons in the first place is an exceedingly difficult task to achieve. The most developed and foremost used techniques for photon generation work well for producing the smallest numbers, with probabilities of generating multiple single-photons rapidly vanishing for only a handful of particles. In this work we tackled these issues and presented experimental progress towards efficient multi-photon manipulation. Below we summarise the findings contained in this thesis.

Chapter 2 presented the first experimental observation of geometric phases in a system of genuinely entangled quantum particles: Two single-photons entangled in their polarisation evolve under bi-local unitaries; as a result, their joint wavefunction picks up a phase factor of geometric and topological nature that depends on the particles' degree of entanglement. In the trivial case—with unentangled particles—the system is composed of two separate and non-interacting subsystems, thus it is no surprising that the total geometric phase is simply the sum of geometric phases acquired by each subsystem alone. A more interesting behaviour occurs when the particles exhibit non-zero entanglement: A non-vanishing total geometric phase appears even for evolutions that result in zero geometric phases of each reduced subsystem. These *entanglement-induced* geometric phases are not determined by trajectories on local parameter spaces of the particles' polarisation states, but instead they are related to curves on a correlation space—the Schmidt sphere—spanned by the parameters of the state's Schmidt decomposition. It is this kind of geometric phase that vanishes only for unentangled particles, and its value increases monotonically with entanglement measures, such as concurrence [6]. A new quantity that can measure quantum entanglement without full state reconstruction is then found.

---

[1]The running time of the algorithm grows slower than exponential but faster than polynomial with respect to the size of the number.

A system of three single-photons is then employed in Chapter 3. A three-qubit state, encoded in the photons' polarisation, evolves via non-local entangling unitaries implemented with linear optics. Under an appropriate mapping [7], simple and physical operations on the tripartite system mimics implementing the complex conjugation—an unphysical transformation—on a simulated state of two qubits undergoing an entangling dynamics. This allowed to obtain the bipartite concurrence—a quantity that involves complex conjugation of states—by simply measuring two observables in the simulator three-qubit state. This proof-of-principle experiment was the first demonstration of an architecture-independent protocol for reducing the overhead in measuring entanglement.

The measured two-photon countrates for the experiment in Chapter 2 was about ~ 2 kHz, whereas for Chapter 3 the three-photon (plus a fourth trigger) countrate was in the order of ~ 1 Hz (at low pump powers as to increase the quality of the results). This drastic decrease, due to the probabilistic and inefficient nature of parametric downconversion, lead us to turn our attention into solid-state emitters with inherent superior photon-emission efficiencies. The state-of-the-art for solid-state based photon sources presented large emission yields at the first collection lens, up to several tens of megahertz; however, available photon rates remained very low in practice, and a mismatch of several orders-of-magnitude between rates at the first lens and rates available in practice was common in the literature. In Chapter 4, we implemented the first single-photon source producing large emission yields at the output of a single-mode fibre, a point in which all photons can be directly used in further experiments. We also found that the photons produced by this source remained mutually indistinguishable even when emitted distant in time. This property is in direct contrast to downconversion sources, where photons emitted by independent laser pulses typically exhibit a markedly reduced photon indistinguishability. Demultiplexing the stream of high-yield and highly-indistinguishable single-photons offered the possibility of producing multi-photon states with higher countrates than downconversion.

In Chapter 5 we implemented a simple demultiplexing scheme to convert three consecutive single-photons—distributed in different temporal modes but sharing the same spatial mode—into three photons distributed in different spatial modes occurring simultaneously: a three-photon source. Thanks to the high brightness of our source, we implemented a BOSONSAMPLING device run with a source between one and two orders-of-magnitude more efficient than previous downconversion sources. This represented the first BOSONSAMPLING device that used only single-photon Fock states at its input; previous experiments would have required independent heralding of each input photon to do so, a task that is virtually impossible with downconversion due to the extremely low countrates that it would generate.

Throughout this thesis, we have thus reported experimental advances towards more efficient multi-photon manipulation, effectively overcoming hurdles inherent to downconversion, and finalising by reporting the first multi-photon experiment realised with a solid-state based source. Hence, to conclude, for all the above mentioned: Enabling multi-photon experiments with solid-state emitters in this my personal farewell to downconversion.

References

[1] O'Brien, J. L., Furusawa, A. & Vuckovic, J. Photonic quantum technologies. *Nat Photon* **3**, 687–695 (2009).

[2] Pan, J.-W. *et al.* Multiphoton entanglement and interferometry. *Rev. Mod. Phys.* **84**, 777–838 (2012).

[3] Shor, P. W. Algorithms for quantum computation: discrete logarithms and factoring. In *Foundations of Computer Science, 1994 Proceedings., 35th Annual Symposium on*, 124–134 (1994).

[4] Knill, E., Laflamme, R. & Milburn, G. J. A scheme for efficient quantum computation with linear optics. *Nature* **409**, 46–52 (2001).

[5] Thew, R. T., Nemoto, K., White, A. G. & Munro, W. J. Qudit quantum-state tomography. *Phys. Rev. A* **66**, 012303 (2002).

[6] Wootters, W. K. Entanglement of formation of an arbitrary state of two qubits. *Phys. Rev. Lett.* **80**, 2245–2248 (1998).

[7] Di Candia, R. *et al.* Embedding quantum simulators for quantum computation of entanglement. *Phys. Rev. Lett.* **111**, 240502 (2013).